https://doi.org/10.5194/egusphere-2026-5858
Preprint. Discussion started: 4 November 2026
© Author(s) 2026. CC BY 4.0 License.

The Seasonal Duality of Elevation-Dependent Warming in High-Latitude Mountains: A Century of Observations in Norway

Ketil Isaksen[1], Alessio M. Canclini[2], Herdis M. Gjelten[1], Cristian Lussana[1], Julia Lutz[1], Øyvind Nordli[1], Rasmus E. Benestad[1], Andreas Dobler[1], Inger Hanssen-Bauer[1], Thomas N. Nipen[2], Line Båserud[1], Erik Berge[1], Helene B. Erlandsen[1], Bernd Etzelmüller[3], Rune S. Ødegård[4], Karianne Ødemark[1]

[1]Climate and Environment Department, Norwegian Meteorological Institute, Oslo, 0313, Norway
[2]Development Centre for Weather Forecasting, Norwegian Meteorological Institute, Oslo, 0313, Norway
[3]Department of Geosciences, University of Oslo, Oslo, 0316, Norway
[4]Department of Manufacturing and Civil Engineering, Norwegian University of Science and Technology, Gjøvik, 2802, Norway

Correspondence to: Ketil Isaksen (ketili@met.no)

Abstract. Elevation-dependent warming (EDW) is driven by complex surface energy and atmospheric feedbacks, yet historical alpine temperature trends in high-latitude regions like Norway remain largely unexamined due to a reliance on lowland datasets. Addressing this gap, we provide the first comprehensive assessment of elevation-dependent warming across Norwegian mountains. We integrate four new century-scale (1904–2025) homogenised high-elevation temperature series, a national station network, and the high-resolution NORA3 regional reanalysis to quantify multi-decadal warming rates, resolve elevation gradients, and evaluate physical mechanisms. The NORA3 reanalysis demonstrates high temporal homogeneity and spatial fidelity against in-situ observations, successfully resolving fine-scale elevation gradients in data-sparse alpine regions and overcoming the decadal trend drifts prevalent in coarser global models. Observations reveal accelerating mountain warming, with annual rates increasing from 0.16–0.17 °C per decade during 1935–2025 to 0.39–0.41 °C per decade during 1981–2025. The EDW signal exhibits a pronounced seasonal duality. A robust positive EDW pattern dominates summer and autumn, with warming rates increasing with elevation and peaking at over 0.45–0.50 °C per decade at the highest alpine areas and sub-Arctic plateaus. This warm-season amplification is likely driven by localised snow-albedo feedbacks from earlier snowpack depletion, reinforced by atmospheric moistening, which disproportionately raises water vapour mixing ratios, thereby enhancing downwelling longwave radiation. Conversely, winter warming is characterised by a topographically constrained inverse EDW regime in sheltered continental valleys. This lowland enhancement is likely driven by atmospheric circulation shifts that increase wind and cloudiness, effectively eroding static cold-air pools and radiation inversions in valleys.

https://doi.org/10.5194/egusphere-2026-5858
Preprint. Discussion started: 4 November 2026
© Author(s) 2026. CC BY 4.0 License.

1 Introduction

Mountain environments are global climate change hotspots, where warming rates often exceed global averages (Gobiet et al., 2014; Pepin et al., 2022; Kotlarski et al., 2023). A central contributor to this amplification is elevation-dependent warming (EDW), characterised by systematic variations in temperature trends along elevation gradients (Mountain Research Initiative EDW Working Group, 2015; Pepin et al., 2025). High-alpine regions host highly sensitive cryospheric components - seasonal snow cover, glaciers, and permafrost - that respond dynamically to climate change (Hock et al., 2019). Beyond cryospheric retreat, mountain ecosystems harbour essential biodiversity, provide vital ecosystem services, and serve as global "water towers", supporting the livelihoods of 1.9 billion people, including 1.6 billion living downstream (Körner, 2004; Grêt-Regamey et al., 2012; Rahbek et al., 2019; Immerzeel et al., 2020). Understanding fine-scale mountain climate trends is critical for safeguarding water resources, socio-economic stability, and alpine environments (Hock et al., 2019; Pepin et al., 2025).

Elevation-dependent warming arises from a complex interplay of surface energy balance feedbacks, atmospheric moisture, and boundary-layer dynamics (Rangwala & Miller, 2012; Pepin et al., 2022, 2025; Byrne et al., 2024; Scherrer et al., 2026). In spring and summer, the snow-albedo feedback acts as a primary driver: earlier snowmelt replaces reflective snow with darker ground, accelerating shortwave absorption and surface warming near seasonal snowlines (Pepin & Lundquist, 2008; Ceppi et al., 2012; Minder et al., 2018; Carrer et al., 2023; Palazzi et al., 2019; Byrne et al., 2024). Simultaneously, rising atmospheric humidity enhances downwelling longwave radiation and alters lapse rates through moist-adiabatic condensation (Ohmura, 2012; Rangwala et al., 2013). However, EDW shows strong seasonal variations and is not universally amplified in mountain regions (Rottler et al., 2019; Scherrer et al., 2026). In autumn and winter, inverse EDW (lowland-enhanced warming) frequently dominates in e.g. the European Alps due to reduced lowland aerosols, declining low stratus clouds, and atmospheric circulation shifts that erode static valley cold-air pools and their associated temperature inversions (Scherrer & Appenzeller, 2014; Tudoroiu et al., 2016; Egli et al., 2017; Pepin et al., 2025; Scherrer et al., 2026).

While regional climate models and homogenised datasets have advanced understanding of elevation-dependent warming in the Alps (e.g., Gobiet et al., 2014; Kuhn and Olefs, 2020; Scherrer et al., 2026), detailed multi-decadal investigations of elevation-dependent warming in high-latitude regions remain limited. High-latitude European mountains, particularly in Norway, cover extensive sub-Arctic alpine terrain with strong maritime-to-continental contrasts and steep topographic gradients. Despite Norway's mountainous landscape and a long tradition of meteorological monitoring, past climate analyses have heavily favored lowland and coastal datasets. Consequently, systematic long-term assessments of EDW patterns across its mountain regions remain lacking.

This study addresses this gap by developing a unique dataset of homogenised observational records from high-elevation weather stations in Norway, and utilising it alongside a national homogenised station network and the high-resolution (3-km) regional reanalysis NORA3 (Haakenstad et al., 2021; Haakenstad & Breivik, 2022).

https://doi.org/10.5194/egusphere-2026-5858
Preprint. Discussion started: 4 November 2026
© Author(s) 2026. CC BY 4.0 License.

The primary aim of this study is to investigate the presence of elevation-dependent warming in Norway and explain the physical mechanisms driving these topographic temperature variations. To achieve this overarching goal, we pursue the following specific objectives:

– Assess recent warming dynamics (1981–2025) using observations and reanalysis to characterise the seasonal magnitude and spatial distribution of elevation-dependent warming and inverse EDW regimes.

– Quantify and compare long-term temperature trends and variability between mountain regions, adjacent lowlands, and gridded datasets.

– Develop long-term, homogenised air temperature reference series for representative high-mountain regions in Norway.

– Evaluate the spatial and temporal accuracy of the high-resolution NORA3 reanalysis against in-situ mountain observations.

The remainder of this paper is structured as follows: Section 2 outlines the study area, observational datasets, NORA3 reanalysis, and statistical methods. Section 3 presents the long-term reference series, regional EDW patterns, and the temporal evaluation of NORA3. In Section 4, we discuss the physical mechanisms driving the seasonal EDW regimes, followed by our main conclusions in Section 5.

2 Data and Methods

2.1 Background

Norway's high-elevation meteorological observations date back to the early 20th century, starting with the establishment of the Haldde summit observatory (893 m a.s.l., 1912–1926, Fig. 1a) in northern Norway. This station integrated groundbreaking auroral physics research with continuous weather observations, significantly advancing early regional weather forecasting (Birkeland, 1913; Devik, 1971; Brekke, 2022). Following Haldde's closure in 1926, the focus of high-elevation meteorology shifted southward to the mountainous regions of southern Norway.

During this period, the Bergen School of Meteorology, led by Vilhelm Bjerknes, revolutionised atmospheric science by introducing the three-dimensional conceptualisation of cyclone dynamics and frontal systems (Bjerknes, 1919; Bjerknes & Solberg, 1922). Decades before the advent of radiosondes, weather radar, or satellite imagery, manned summit observatories provided critical insights into upper-air dynamics. Long-term records from stations such as Fannaråki (2062 m a.s.l., established in 1926 and manned year-round from 1932 to 1978; Spinnangr, 1926; Hjortnæs, 1979) and Gaustatoppen (1804 m a.s.l., established in 1934, Fig. 1a) were essential in characterising air-mass structures and tracking low-pressure systems originating from the North Atlantic. Driven by early numerical weather prediction theories (Bjerknes, 1904; Bjerknes et al., 1933), these stations provided essential three-dimensional atmospheric data.

Beyond their contributions to the development of theoretical meteorology, high-elevation stations also played vital operational roles. They supplied real-time weather data for early aviation routes, mountain roads, and railway passes (e.g., Slirå on the Bergen Railway, 1300 m a.s.l.; and Fokstugu on the Dovre Railway, 973 m a.s.l.). As Norway expanded its hydro-electric power sector, these stations provided essential meteorological and snowpack data for runoff forecasting and reservoir

https://doi.org/10.5194/egusphere-2026-5858
Preprint. Discussion started: 4 November 2026
© Author(s) 2026. CC BY 4.0 License.

management. Furthermore, they pioneered daily mountain weather forecasts, which became critical for mountaineers, winter recreationalists, and rescue teams during an era when alpine weather dynamics were poorly understood. The establishment of high-elevation observatories in Norway, such as Fannaråki and Gaustatoppen, initiated a long tradition of mountain climatology. Early efforts to systematize and analyze these mountain observations were pioneered by Spinnangr and Eide (1948), who provided one of the first comprehensive overviews of the alpine climate in southern Norway.

2.2 Study area

Mainland Norway spans a pronounced latitudinal gradient from approximately 58°N to 71°N, featuring a highly complex topography characterised by steep maritime fjords, deep inland valleys, and extensive high-alpine plateaus. In addition to the latitudinal gradient, there is a strong west-east gradient, with increasing continentality, and winter inversions, towards east. The forest line functionally defines the mountain–lowland interface in Norway, rising from 400–600 m a.s.l. along exposed coasts to 900–1100 m a.s.l. in the continental interior and dipping below 200 m a.s.l. in the far north (Bryn & Potthoff, 2018).

To systematically account for this spatial and climatic variability, the study area is categorised into seven standard climatological temperature regions (Hanssen-Bauer et al., 2022) that capture the dominant macro-climatic boundaries across the country (Fig. 1). Within this broader national framework, the analysis further isolates specifically defined mountain domains (Fig. 1b, Table 1). These localised mountain domains are centered on prominent alpine massifs and key high-elevation observatories. To contextualise the topographic diversity, the minimum, maximum, and mean altitudes for each domain are detailed in Table 1. This provides the necessary spatial constraints to evaluate fine-scale topographical temperature gradients across the mountain-lowland interface (Fig. 1).

https://doi.org/10.5194/egusphere-2026-5858
Preprint. Discussion started: 4 November 2026
© Author(s) 2026. CC BY 4.0 License.

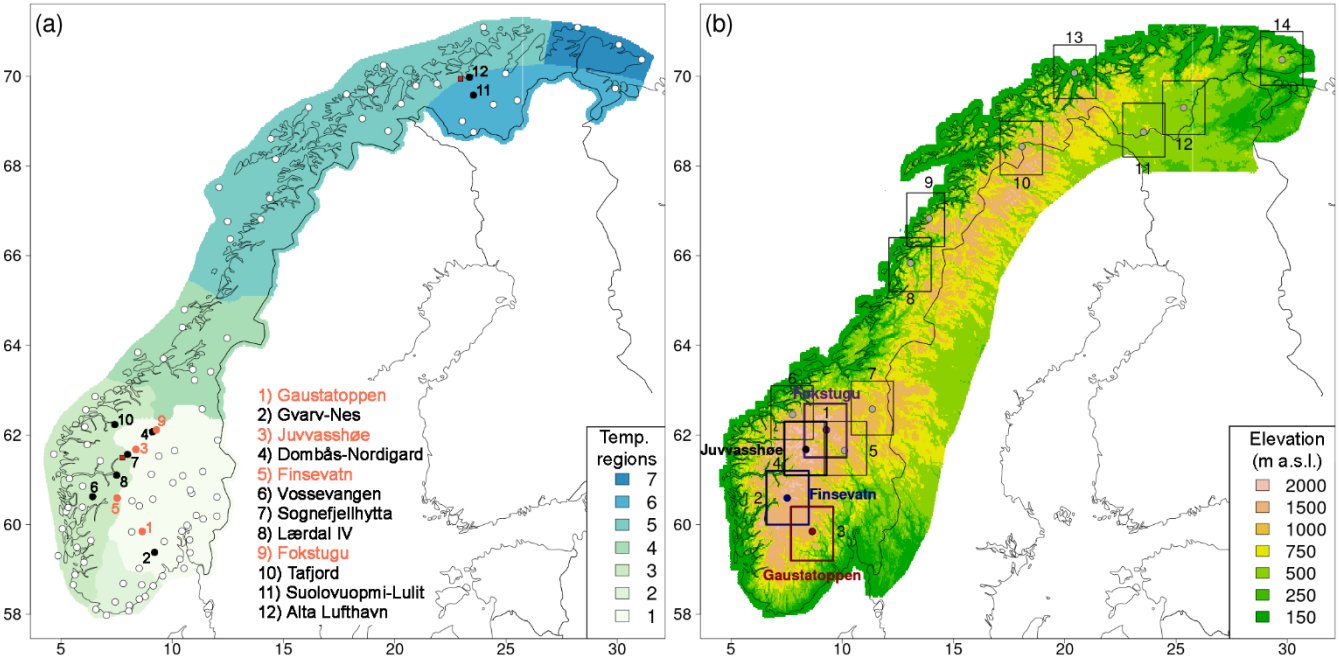


Figure 1. Overview of the study areas, observational station network, and mountain domains across Norway. (a) Seven climatological temperature regions (1–7): Eastern Norway (region 1), Southern Norway (region 2), Western Norway (region 3), Central Norway (region 4), Northern Norway-West (region 5), Inland-Finnmark (region 6), Varanger (region 7). White dots indicate the locations of the observational weather stations used in this study. Numbered dots (1–12) indicate the stations used for the pairwise comparisons in Fig. 3, with corresponding names listed in the legend. Red dots highlight the key high-elevation stations, while black dots indicate the other stations included in these pairwise analyses. Red squares mark the locations of Norway's first summit observatories, Haldde (northern Norway) and Fannaråki (southern Norway). (b) A topographical elevation map (m a.s.l.) of Norway highlighting the mountain domains (rectangles, numbered 1–14) centered on key high-elevation observation sites (indicated by grey dots) used for localised NORA3 reanalysis. The names of the four key southern Norway mountain domains are denoted. See Table 1 for further information about each numbered mountain domain and its corresponding central observation site.

https://doi.org/10.5194/egusphere-2026-5858
Preprint. Discussion started: 4 November 2026
© Author(s) 2026. CC BY 4.0 License.

Table 1. Overview of mountain domains and central weather stations. The table includes the geographic coordinates for both the central in-situ stations and the spatial extent of their respective NORA3 analysis domains. To illustrate the topographic characteristics of each region, the minimum and maximum elevation range and the mean elevation (m a.s.l.) of the topography within each domain are provided.

ID	Mountain Domain	Central Station	Station Longitude (°E)	Station Latitude (°N)	Domain Longitude Range (°E)	Domain Latitude Range (°N)	Domain Elevation Range (m a.s.l.)	Domain Mean Elevation (m a.s.l.)
1	Dovrefjell	Fokstugu	9.2862	62.1133	8.3–10.2	61.5–62.7	6–2156	1121
2	Hardangervidda North	Finsevatn	7.5270	60.5938	6.6–8.5	60.0–61.2	0–1833	1126
3	Hardangervidda South	Gaustatoppen	8.6562	59.8497	7.7–9.6	59.2–60.4	19–1540	781
4	Jotunheimen	Juvvasshøe	8.3690	61.6775	7.4–9.3	61.1–62.3	0–2156	1207
5	Rondane	Venabu	10.1082	61.6513	9.2–11.1	61.1–62.3	138–1789	906
6	Romsdalsalpene	Mannen	7.7703	62.4555	6.8–8.7	61.9–63.1	0–1843	680
7	Rørosvidda	Røros lufthavn	11.3518	62.5773	10.4–12.3	62.0–63.2	191–1457	811
8	Vistfjellan	Middagseidklumpen	13.0760	65.8350	12.1–14.0	65.2–66.4	0–1495	328
9	Meløyalpene	Glomfjord - Tverrfjellet	13.9067	66.8303	12.9–14.6	66.2–67.4	0–1435	280
10	Narvikfjellene	Bjørnfjell	18.0767	68.4323	17.1–19.0	67.8–69.0	0–1776	716
11	Finnmarksvidda South	Sihccajavri	23.5387	68.7553	22.6–24.5	68.2–69.4	259–819	406
12	Finnmarksvidda East	Iskoras	25.3460	69.3003	24.4–26.3	68.7–69.9	73–986	342
13	Lyngsalpan	Arnøya - Trolltinden	20.4310	70.0750	19.5–21.4	69.5–70.7	0–1292	152
14	Varangervidda	Ragnarokk	29.7663	70.3670	28.8–30.7	69.8–71.0	0–576	148

https://doi.org/10.5194/egusphere-2026-5858
Preprint. Discussion started: 4 November 2026
© Author(s) 2026. CC BY 4.0 License.

2.3 Datasets

2.3.1 Long-term mountain reference series

We established long-term (spanning 1904–2025) homogeneous monthly temperature series for four high-elevation reference stations in southern and central Norway (Table 2).

High-elevation meteorological observations are scarce, often disrupted by station relocations, instrumentation changes, and environmental alterations. To ensure data reliability, a comprehensive homogeneity analysis was performed.
The four series were homogenised using HOMER software (Mestre et al., 2013) and metadata from station history archives at MET Norway.

The analysis included initial quality checks, outlier removal, and correction of identified digitisation errors. To create the longest possible continuous records, some of the series were merged with data from neighbouring stations and data gaps were interpolated. Detailed descriptions on the methods and analyses can be found in Appendix A.

Table 2. The four target mountain reference series analysed in this study.

Station	Elevation (m a.s.l.)	Period	Key inhomogeneities
Fokstugu	973	1923–2025	Relocation and change in equipment
Finsevatn	1210	1904–2025	Relocations and change in equipment
Gaustatoppen	1804	1934–2025	Change in equipment
Juvvasshøe	1894	1931–2025	Relocation

2.3.2 National Homogenised Station Network

Monthly mean near-surface air temperature time series from other stations were extracted from a national homogenised temperature reference dataset developed by the Norwegian Meteorological Institute (MET Norway; Kuya et al., 2020). This dataset, originally designed for calculating climate normals (1991–2020; Tveito, 2021), includes 108 homogenised monthly mean temperature series covering mainland Norway (1961–2018, extended to 2025).

Stations were selected based on World Meteorological Organisation (WMO) criteria, requiring at least 80% data coverage over a 60-year period. The baseline dataset was supplemented with the four primary high-elevation target series and additional data from the Sognefjellhytta and Venabu stations (see Appendix A) to improve spatial coverage in mountain environments.

https://doi.org/10.5194/egusphere-2026-5858
Preprint. Discussion started: 4 November 2026
© Author(s) 2026. CC BY 4.0 License.

Broad macro-climatic gradients, driven by Norway's latitudinal span (58°N–71°N) and variable proximity to the coast, mask vertical temperature trends on a national scale. To isolate EDW signals, observational series were stratified into seven temperature regions (Fig. 1) and evaluated against regional climatic forest lines. Several regions lie entirely below the forest line, and the station network is inherently skewed toward inhabited lowland and coastal areas. To address this alpine data sparsity, the four key reference series and Sognefjellhytta were included in the upper-elevation tiers of Eastern and Western Norway (Regions 1 and 3).

2.3.3 High-Resolution Reanalysis Dataset (NORA3)

The NORA3 reanalysis (Haakenstad et al., 2021; Haakenstad & Breivik, 2022) provides 3-km resolution data for the Scandinavian Peninsula and adjacent seas, offering a significant improvement over global reanalyses like ERA5. It uses the HARMONIE-AROME convection-permitting numerical weather prediction model including a high-resolution digital elevation data. With the integrated SURFEX (Surface Externalisée, Masson et al., 2013) surface model, NORA3 resolves surface-atmosphere energy fluxes, boundary-layer dynamics, and local slope wind systems in steep topography, interacting with a surface analysis scheme that assimilates surface observations from different sources. Validation of near-surface (2-m) air temperature against in-situ weather stations demonstrates high accuracy (correlation coefficient r = 0.972, Haakenstad & Breivik, 2022).

To bring the NORA3 temperatures closer to the station observations, we interpolated the 2-m temperature field from the original 3 km grid onto a 1 km grid and corrected it for the elevation difference between the 3 km model orography and a 1 km digital elevation model (Danielson and Gesch, 2011). The correction uses an estimated lapse-rate that varies in space and time: at each high-resolution grid point, the local temperature lapse rate is obtained from a linear regression of 2-m temperature against surface elevation over the coarse resolution grid points in an 11 × 11 neighbourhood, and this rate is applied to the elevation difference between the two orographies. The lapse rate is capped at +/-10 °C/km. Additionally, only gridpoints with a land-area fraction above 50% are used in the regression, in order to prevent points over ocean to contribute to a lapse-rate that in reality is a land-sea gradient

2.3.4 Homogenised Gridded Reference Dataset (KlimGrid)

The KlimGrid dataset (Tveito, 2021, 2023) provides 1-km gridded monthly air temperature anomaly fields across mainland Norway (1901–2020). It serves as the official reference dataset established by MET Norway for calculating national climate normals (1991–2020) and monitoring long-term temperature trends in national climate assessment reports (Dyrrdal et al., 2025).

KlimGrid is constructed from a fixed set of 165 long-term temperature series, ensuring spatial and temporal consistency despite changes in weather station density over time (Tveito, 2023). Monthly temperature anomalies relative to the 1991–2020 standard normal period are interpolated onto the 1-km grid using a discretised thin-plate spline algorithm (Tveito, 2021, 2023). By correcting for non-climatic shifts caused by equipment upgrades, station relocations, and changing

https://doi.org/10.5194/egusphere-2026-5858
Preprint. Discussion started: 4 November 2026
© Author(s) 2026. CC BY 4.0 License.

network configurations, KlimGrid minimises local spatial variance and suppresses spurious local anomalies. Consequently, it provides a spatially coherent and robust observational baseline, making it an invaluable tool for evaluating regional and national trends in e.g. NORA3.

2.4 Statistical Analysis

Statistical analyses were executed across three time windows to quantify temperature variations, assess elevation-dependent warming, and evaluate model performance:

1) 1935–2025: Covers the operational period following the establishment of historical observatories (e.g., Fannaråki and Gaustatoppen), providing a unique near-century perspective on high-latitude alpine air temperature trends.

2) 1961–2025: Covers the two most recent standard climatological normal periods (1961–1990 and 1991–2020) and the subsequent years up to 2025, aligning with the coverage of national homogenised station networks, KlimGrid, and the NORA3 reanalysis.

3) 1981–2025: Focuses on the most recent 45-year period of rapid global and regional warming, optimal satellite/reanalysis data quality, and increased density of high-elevation automated weather stations (AWS).

Observational stations and gridded reanalysis fields were stratified into seven standard Norwegian temperature regions (Regions 1–7; Fig. 1a) as defined by Hanssen-Bauer et al. (2022). These regions group areas with spatially coherent multi-decadal temperature variations and align climatological boundaries with major geographical divides.

To isolate the vertical temperature signal, adjacent high-elevation and lowland stations from the national network were coupled to form localised station pairs. These pairs were selected based on close geographic proximity and continuous data coverage during the 1981–2025 period.

Time series were analysed annually (ANN) and seasonally (DJF, MAM, JJA, SON). Linear trends were computed using Ordinary Least Squares (OLS) regression, expressed as rates of change per decade (°C per decade). Statistical significance was assessed with non-parametric Mann-Kendall tests (Mann, 1945; McLeod, 2005) at thresholds of $p < 0.05$ and $p < 0.01$.

To capture multi-decadal variability and long-term climatic trajectories without assuming predefined trend forms, temperature anomaly time series (relative to the 1991–2020 WMO baseline) were smoothed using Locally Estimated Scatterplot Smoothing (LOESS) filters. LOESS spans of ~10 years and ~30 years were applied to depict inter-decadal oscillations and multi-decadal trends, respectively.

To evaluate fine-scale spatial EDW patterns across complex topography, high-resolution NORA3 reanalysis grid-cell linear trends (1981–2025) were analysed within standardised 1.9° x 1.2° spatial mountain domains, each centered on a primary weather station representing its respective mountain massif.

Grid cells within each mountain domain were classified into 250-m elevational bands (e.g., 0–249 m, 250–499 m, ..., >1750 m a.s.l.). In the northern mountain domains with smaller elevation ranges (Finnmarksvidda south, Finnmarksvidda east and Varangervidda, Fig. 1b, Table 1), 100-m bands were used. Decadal warming trends within each elevation band were

https://doi.org/10.5194/egusphere-2026-5858
Preprint. Discussion started: 4 November 2026
© Author(s) 2026. CC BY 4.0 License.

visualised using kernel density estimation via violin plots, depicting distribution spread, medians, interquartile ranges, and grid-cell sample sizes (n). Caution is advised when interpreting trend for tail-end elevation bands (e.g., deep valley bottoms < 250 m a.s.l. or isolated mountain peaks > 1750–2100 m a.s.l.), as small sample sizes (n < 50) may increase noise or introduce minor smoothing artifacts.

The trend analysis for NORA3 is conducted using the Theil-Sen slope estimator (Sen, 1968), a robust method suited for non-parametric data. Trend significance was assessed using the Mann-Kendall test (Mann, 1945; McLeod, 2005). To address multiple testing issues across mountain domains, the False Discovery Rate (FDR) correction was applied (Benjamini & Hochberg, 1995; Wilks, 2006). Grid-point trend significance was assessed with the Mann–Kendall test, controlling the false discovery rate across all grid cells following Benjamini and Hochberg (1995). Because spatial correlation between neighbouring grid cells makes the test overly permissive, the FDR control level was set to twice the desired global level, $\alpha_FDR = 2\alpha_global$, which yields approximately correct global significance (Wilks, 2016, 2019). Trends were therefore considered significant where the Benjamini–Hochberg adjusted p-value was below $\alpha_FDR = 0.10$, corresponding to a global significance level of 0.05.

Finally, to assess the correspondence between station observations and NORA3 reanalysis data, Pearson correlation coefficients (r) were calculated from monthly temperature series, quantifying temporal covariance between in-situ observations and co-located NORA3 grid cells.

3. Results

3.1 Homogeneous Mountain Reference Series

The homogenised temperature series for Fokstugu, Finsevatn, Gaustatoppen, and Juvvasshøe reveal a consistent long-term warming trend (Fig. 2a-d). Superimposed on this overarching trend, the smoothed anomalies show pronounced multi-decadal variability (Fig. 2e-f). This is marked by a distinct warm phase in the 1930s and 1940s, a subsequent cooler period during the 1960s and 1970s, and a sharp, uninterrupted temperature increase thereafter.

Multi-decadal annual warming rates across the sites show regional coherence and statistical significance.

1935–2025: Annual mean air temperatures increased at a highly significant rate ($p < 0.01$) of 0.16 °C per decade at Fokstugu, Gaustatoppen, and Juvvasshøe, and 0.17 °C per decade at Finsevatn (Table 3).

1961–2025: Warming accelerated significantly, with rates of 0.31–0.32 °C per decade ($p < 0.01$) across all sites (Table 3). This strong spatial uniformity in multi-decadal temperature anomalies is illustrated in Fig. 2e-f, where the series for all four sites follow nearly identical decadal trajectories.

1981–2025: During the most recent 45 years, annual warming further intensified to 0.39 °C per decade ($p < 0.01$) at Fokstugu, Gaustatoppen, and Juvvasshøe, and 0.41 °C per decade ($p < 0.01$) at Finsevatn (Table 3).

When examined seasonally for the period 1981–2025, elevation-dependent warming patterns and varying statistical significance emerge.

https://doi.org/10.5194/egusphere-2026-5858
Preprint. Discussion started: 4 November 2026
© Author(s) 2026. CC BY 4.0 License.

Autumn (SON) shows the strongest and most consistent warming rates, statistically significant across all stations ($p < 0.01$ at Finsevatn, Gaustatoppen, and Juvvasshøe; $p < 0.05$ at Fokstugu). Rates range from 0.38 °C per decade at Fokstugu, the lowest-elevation site (973 m a.s.l.), to 0.47 °C per decade at Gaustatoppen (1804 m a.s.l.).

Summer (JJA) displays similarly strong and highly significant warming (0.37–0.46 °C per decade, $p < 0.01$). The highest warming rates are observed at the highest-elevation sites (Table 3).

Winter (DJF) trends reveal spatial and elevational contrasts. Substantial warming occurs across three of the mountain sites: Fokstugu (0.41 °C per decade), Finsevatn (0.40 °C per decade), and Juvvasshøe (0.38 °C per decade). In contrast, Gaustatoppen, the most exposed summit station, records a notably weaker trend of 0.25 °C per decade (Table 3). However, due to higher interannual variability in winter temperatures, none of these trends reach statistical significance at the 5% level (Table 3).

Spring (MAM) warming ranges from 0.31 to 0.37 °C per decade across all sites. Finsevatn shows the strongest statistical significance ($p < 0.01$), while the remaining three sites show significant trends at the 5% level ($p < 0.05$; Table 3). Several of the warmest years on record for the high-mountain network occurred within the last decade, including 2014, 2020, 2024, and 2025 (Fig. 2a-d). This highlights the ongoing intensification of warming trends, particularly in the most recent years.

https://doi.org/10.5194/egusphere-2026-5858
Preprint. Discussion started: 4 November 2026
© Author(s) 2026. CC BY 4.0 License.

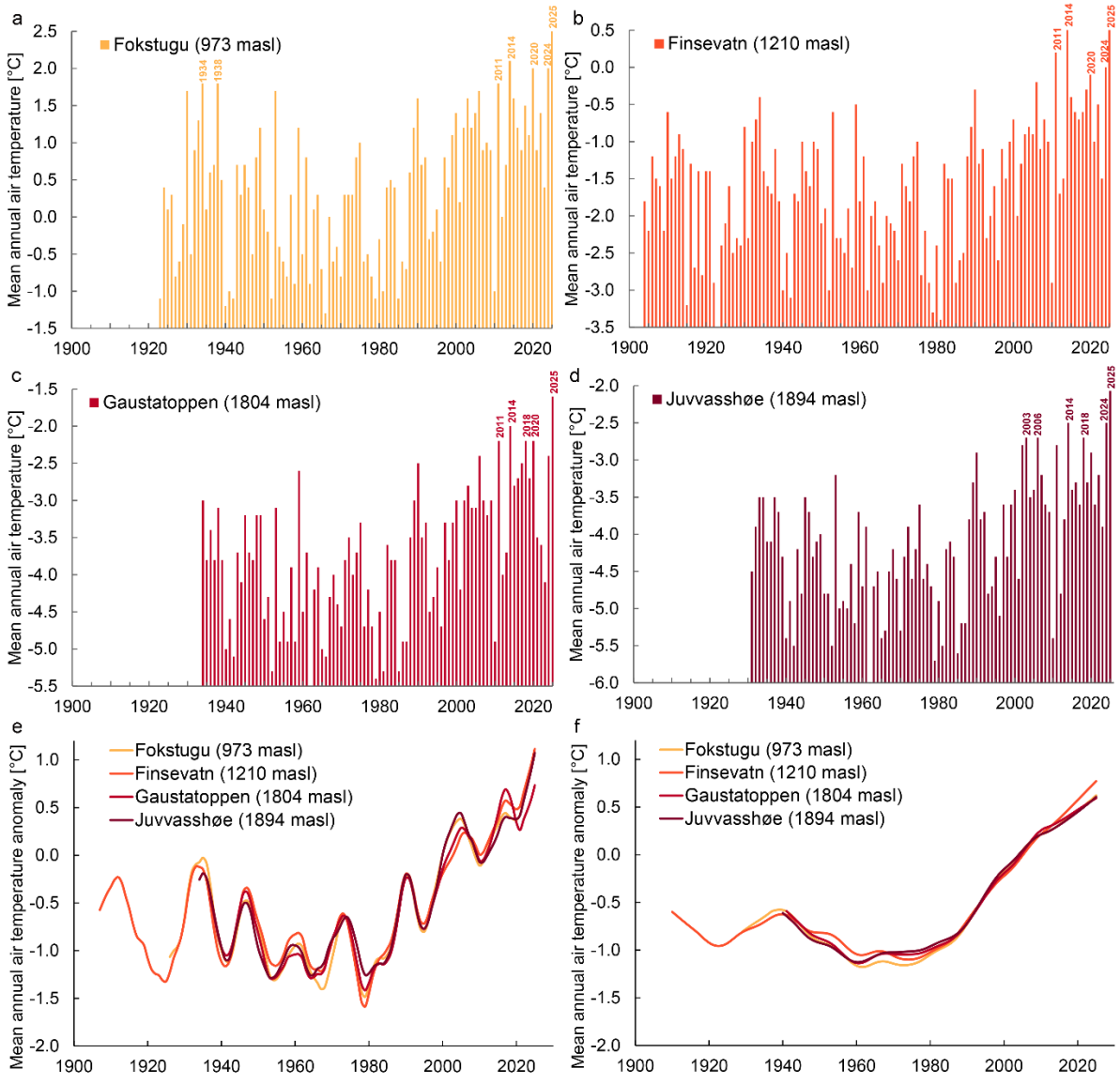


Figure 2. Long-term mean annual air temperature (MAAT) records from four homogenised high-elevation meteorological stations in Norway. (a-d) Absolute MAATs for (a) Fokstugu (973 masl), (b) Finsevatn (1210 masl), (c) Gaustatoppen (1804 masl), and (d) Juvvasshøe (1894 masl), with the warmest years annotated. (e) MAAT anomalies relative to the 1991–2020 baseline, smoothed using a ~10-year LOESS filter to illustrate decadal variability. (f) MAAT anomalies smoothed with a ~30-year LOESS filter to emphasise long-term climatic trends. Panels (e) and (f) share narrower y-axis scales to better highlight climatic progression.

https://doi.org/10.5194/egusphere-2026-5858
Preprint. Discussion started: 4 November 2026
© Author(s) 2026. CC BY 4.0 License.

Table 3. Linear temperature trends (°C per decade) at four homogenised mountain stations in Norway. Seasonal (DJF, MAM, JJA, SON) and annual trends are shown for 1981–2025, along with long-term annual trends for 1961–2025 and 1935–2025. Significant trends are highlighted in bold ($p < 0.01$) and italics ($p < 0.05$).

Trends (°C per decade)	1935–2025	1961–2025	1981–2025				
	ANN	ANN	ANN	DJF	MAM	JJA	SON
Fokstugu	**0.16**	**0.31**	**0.39**	0.41	*0.35*	**0.38**	*0.38*
Finsevatn	**0.17**	**0.32**	**0.41**	0.40	**0.37**	**0.40**	**0.43**
Gaustatoppen	**0.16**	**0.31**	**0.39**	0.25	*0.34*	**0.46**	**0.47**
Juvvasshøe	**0.16**	**0.31**	**0.39**	0.38	*0.31*	**0.37**	**0.45**

3.2 Elevation-Dependent Warming Patterns Across Regions

3.2.1 Regional Pairwise Comparisons

The selected station pairs (Fig. 3) reveal distinct seasonal EDW contrasts. During summer (JJA) and autumn (SON), a consistent positive EDW signal dominates across the country. In Western Norway, mountain stations (Finsevatn, Sognefjellhytta) warm up to 0.15–0.23 °C per decade faster than their lowland fjord counterparts (Vossevangen, Lærdal IV). A similar positive gradient is observed in Eastern Norway, where summit stations (Gaustatoppen, Juvvasshøe) warm more rapidly than adjacent lowlands. In Northern Norway, despite high-elevation data sparsity, this altitudinal contrast persists across all seasons; the interior plateau (Suolovuopmi-Lulit) consistently warms faster than the coast (Alta Lufthavn), reaching annual rates of 0.60 °C per decade.

Winter (DJF) and spring (MAM) show mixed or reversed elevational warming patterns. The most pronounced inverse EDW relationship occurs during winter in Eastern Norway, where lowland valley stations warm more than twice as fast as exposed summits (e.g., Gvarv-Nes at 0.56 °C per decade versus Gaustatoppen at 0.25 °C per decade). Along the cross-regional divide, the winter warming trend at the Fokstugu plateau (0.41 °C per decade) only slightly exceeds the maritime lowland station Tafjord (0.35 °C per decade), illustrating how positive EDW is dampened or reversed during the cold season.

https://doi.org/10.5194/egusphere-2026-5858
Preprint. Discussion started: 4 November 2026
© Author(s) 2026. CC BY 4.0 License.

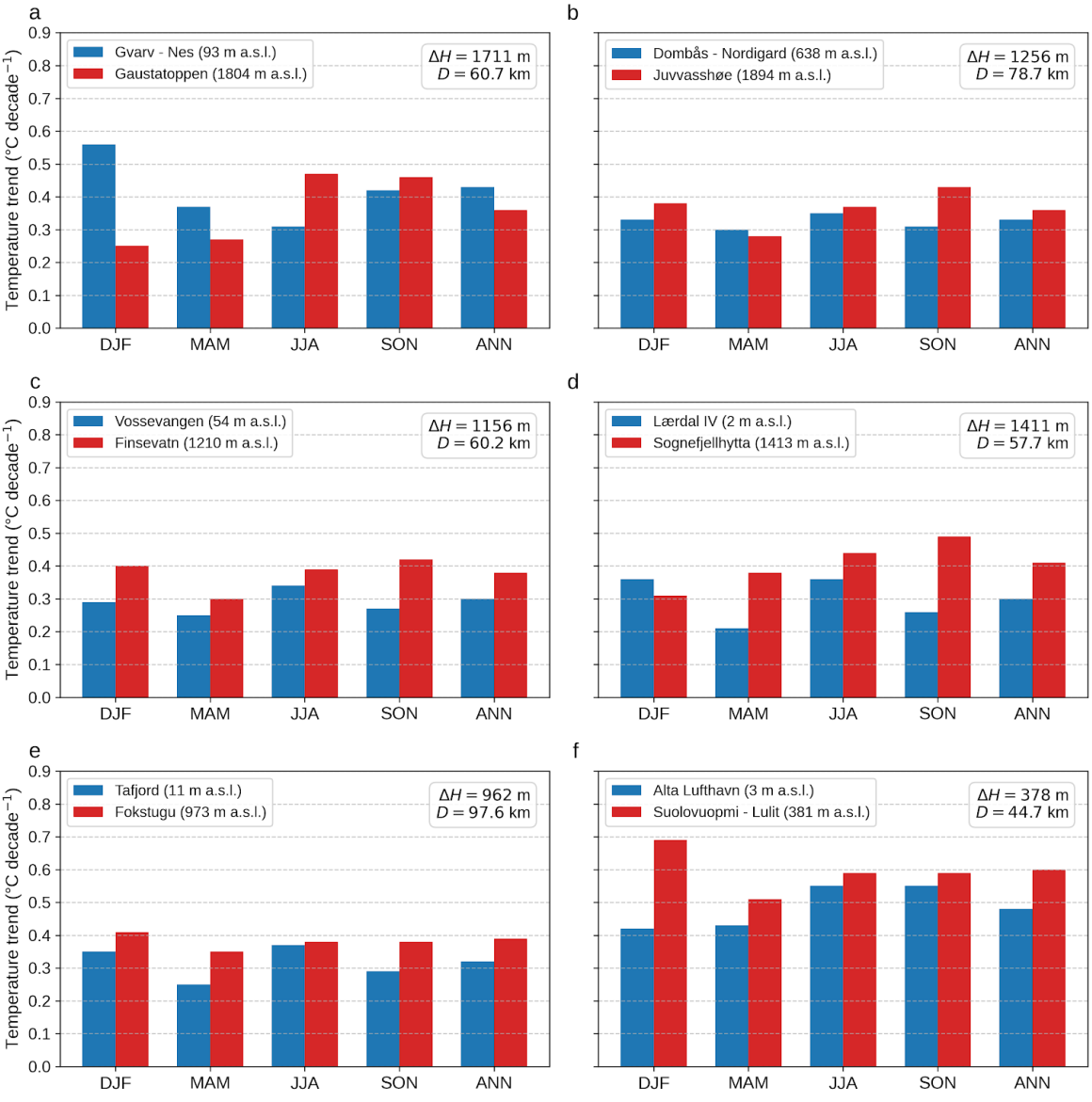


Figure 3. Seasonal (DJF, MAM, JJA, SON) and annual (ANN) air temperature trends (°C per decade) for 1981–2025 across representative station pairs in Norway, illustrating EDW patterns. The geographic locations of these stations are indicated by numbered dots (1–12) in Fig. 1a. Each panel compares a low-elevation valley/fjord station (blue bars) with a high-elevation mountain/plateau station (red bars): (a, b) Eastern Norway: (a) Gaustatoppen vs. Gvarv-Nes; (b) Juvvasshøe vs. Dombås-Nordigard. (c, d) Western Norway: (c) Finsevatn vs. Vossevangen; (d) Sognefjellhytta vs. Lærdal IV. (e, f) Mid- and Northern Norway: (e) Fokstugu vs. Tafjord; (f) Suolovuopmi-Lulit vs. Alta Lufthavn. Station elevations (m a.s.l.) are listed in the legend. Elevation differences (ΔH, in meters) and geographic distances (D, in kilometers) between station pairs are annotated within each panel. Due to data scarcity at high elevations in Mid- and Northern Norway, only two representative pairs are included for this region. Note that Fokstugu, while geographically located in Eastern Norway on the Dovrefjell mountain plateau, lies at the weather divide near the border with Mid-Norway.

https://doi.org/10.5194/egusphere-2026-5858
Preprint. Discussion started: 4 November 2026
© Author(s) 2026. CC BY 4.0 License.

3.2.2 Altitudinal Gradients and Regional Differences

Due to the spatial constraints of the station network, only Eastern and Western Norway (Regions 1 and 3) contain sufficient long-term records above the forest line to resolve vertical temperature contrasts (Fig. 4a). During the warm season, distinct regional differences emerge across the mountain-lowland interface (Fig. 4b, c, f, g). In Western Norway, a robust and statistically significant positive EDW signal is present. Mountain stations above the 600 m a.s.l. forest line warmed significantly faster than lowland sites during both summer (+0.40 vs. +0.32 °C per decade, $p=0.027$) and autumn (+0.45 vs. +0.38 °C per decade, $p<0.001$). In contrast, Eastern Norway experienced high background warming across all elevations. While high-elevation warming rates above 900 m a.s.l. were slightly higher than in the lowlands during summer (+0.37 vs. +0.34 °C per decade) and autumn (+0.44 vs. +0.43 °C per decade), these differences were not statistically significant ($p=0.36$ in summer; $p=0.67$ in autumn).

During the cold season, temperature trends show complex elevational gradients (Fig. 4d, e, h, i). Winter (DJF) in Eastern Norway is characterised by a pronounced inverse EDW pattern; sheltered lowland stations recorded rapid median warming exceeding +0.50 °C per decade, while warming at exposed high-elevation sites was substantially suppressed. Conversely, winter warming in Western Norway remains highly variable, showing only a weak positive trend-elevation gradient. Spring (MAM) acts as a transitional period with spatially uniform warming across both regions; median decadal warming rates hovered steadily between +0.35 °C and +0.42 °C, with no distinct trend-elevation gradients in either Eastern or Western Norway.

https://doi.org/10.5194/egusphere-2026-5858
Preprint. Discussion started: 4 November 2026
© Author(s) 2026. CC BY 4.0 License.

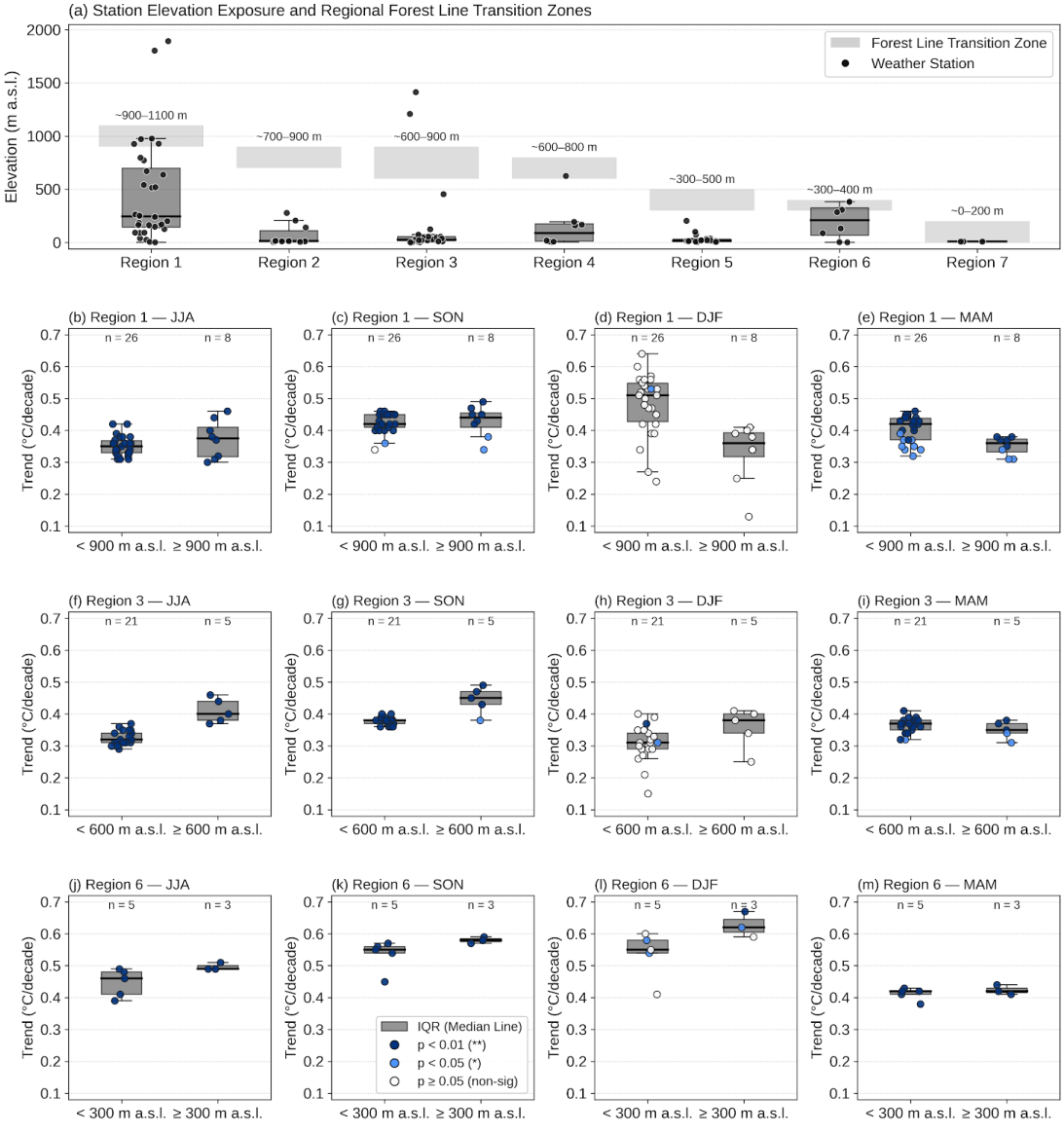


Figure 4. Weather station elevation exposure and seasonal warming trends (1981–2025, °C per decade) relative to regional climatic forest lines across temperature regions in Norway (Hanssen-Bauer et al., 2022; regional forest line transition zones adapted from Bryn & Potthoff, 2018). (a) Elevational distribution of weather stations (n = 103) within each temperature region: Eastern Norway (region 1), Southern Norway (region 2), Western Norway (region 3), Central Norway (region 4), Northern Norway-west (region 5), Inland-Finnmark (region 6), Varanger (region 7). Shaded grey bands indicate regional forest line transition zones. (b-m) Near-surface air temperature trends stratified into two elevation classes based on the lower regional forest line thresholds: 900 m a.s.l. for Region 1 (panels b–e), 600 m a.s.l. for Region 3 (panels f–i), and 300 m a.s.l. for Region 6 (panels j–m) across summer (JJA; b, f, j), autumn (SON; c, g, k), winter (DJF; d, h, l), and spring (MAM; e, i, m). Boxplots display the median (thick horizontal line) and interquartile range (IQR, grey box), while scatter points depict individual weather stations. Circles fill shades indicate trend significance. Sample sizes (n) are annotated at the top of each panel.

https://doi.org/10.5194/egusphere-2026-5858
Preprint. Discussion started: 4 November 2026
© Author(s) 2026. CC BY 4.0 License.

Linear trend-elevation regressions across individual months further illuminate these regional contrasts (Fig. B1, B2). Western Norway shows persistent positive elevation-dependent warming throughout summer and early autumn; warming rates approach +0.60 °C per decade for high-elevation summits (>1200 m a.s.l.) in July, with the positive trend-elevation slope peaking in September at approximately +0.7 °C per decade above 1400 m a.s.l. In Eastern Norway, the overall flat summer slope masks significant intra-seasonal compensation: a distinct negative gradient in June is cancelled out by weakly positive slopes in July and August. During winter, Eastern Norway consistently shows steep negative slopes, confirming a widespread inverse EDW regime.

Despite the rapid winter warming observed in sheltered interior valleys, cold-season trends (DJF and MAM) exhibit lower statistical robustness across the entire observational network (Fig. 4, Table 3, Table B1). Pronounced interannual temperature variability prevents the majority of winter and spring trends - whether at high-elevation observatories (+0.36 to +0.38 °C per decade) or in lowland valleys (>+0.50 °C per decade) - from achieving statistical significance at the 5% level.

Finally, in Inland Finnmark (Region 6), stratifying stations across the 300 m a.s.l. sub-Arctic forest line reveals high baseline warming accompanied by high-elevation amplification (Fig. 4j-m). During summer and autumn, the Finnmarksvidda plateau warmed at highly significant rates ($p < 0.01$) of +0.49 and +0.58 °C per decade, slightly outpacing the adjacent lowlands (+0.46 and +0.55 °C per decade). This plateau amplification becomes most pronounced in winter, when elevated sites experienced the region's highest warming rates (averaging +0.62 °C per decade, peaking at +0.67 °C at Suolovuopmi-Lulit) compared to +0.55 °C per decade below the forest line. Spring warming remained spatially uniform across both elevation classes at +0.42 °C per decade.

3.2.3 High-Resolution Spatial and Elevational Warming Patterns from NORA3 Reanalysis

To examine the spatial structure and altitudinal scaling of near-surface warming across southern Norway (Regions 1–3), macro-regional NORA3 reanalysis fields for 1981–2025 were evaluated (Fig. 5). On an annual basis, warming is spatially coherent, with 100% statistically significant field-wide trends ranging from +0.35 to +0.45 °C per decade. However, this annual aggregate masks pronounced seasonal and topographical contrasts.

During the warm season, the reanalysis captures a distinct high-elevation warming amplification. Autumn exhibits the most spatially coherent and robust trends (100% field significance); high-mountain massifs such as Jotunheimen, Hardangervidda, and Dovrefjell (Table 1, Fig. 1) show the strongest warming (>0.45–0.50 °C per decade), contrasting with the slower-warming valley floors (0.35–0.40 °C per decade). Summer displays a similar elevation-dependent pattern, though strongly modulated by a west-to-east gradient. The highest summer warming rates (>0.40–0.50 °C per decade) are concentrated in Western Norway and along high-alpine areas, whereas sheltered interior lowlands in Eastern Norway show weaker, statistically non-significant trends (<0.30 °C per decade).

Conversely, the cold season is characterised by lower field significance and reversed or muted altitudinal gradients. In winter, rapid warming (>0.50 °C per decade) is heavily concentrated in the cold interior valleys of Eastern Norway.

https://doi.org/10.5194/egusphere-2026-5858
Preprint. Discussion started: 4 November 2026
© Author(s) 2026. CC BY 4.0 License.



However, widespread non-significant trends dominate the upper mountain elevations and much of the broader eastern areas, directly mirroring the high interannual variability seen in the station observations (Table 3, Table B1). Spring acts as a moderate transitional phase (+0.25 to +0.45 °C per decade), where statistically significant trends are largely confined to southern and southeastern areas, leaving the central high-alpine plateaus statistically non-significant.

While Figure 5 highlights the topographic signatures of elevation-dependent warming across southern Norway, an expansion to the national scale confirms that this EDW-signal, alongside a significant latitudinal warming gradient, is a robust feature across all of mainland Norway (Appendix Fig. C1).

https://doi.org/10.5194/egusphere-2026-5858
Preprint. Discussion started: 4 November 2026
© Author(s) 2026. CC BY 4.0 License.

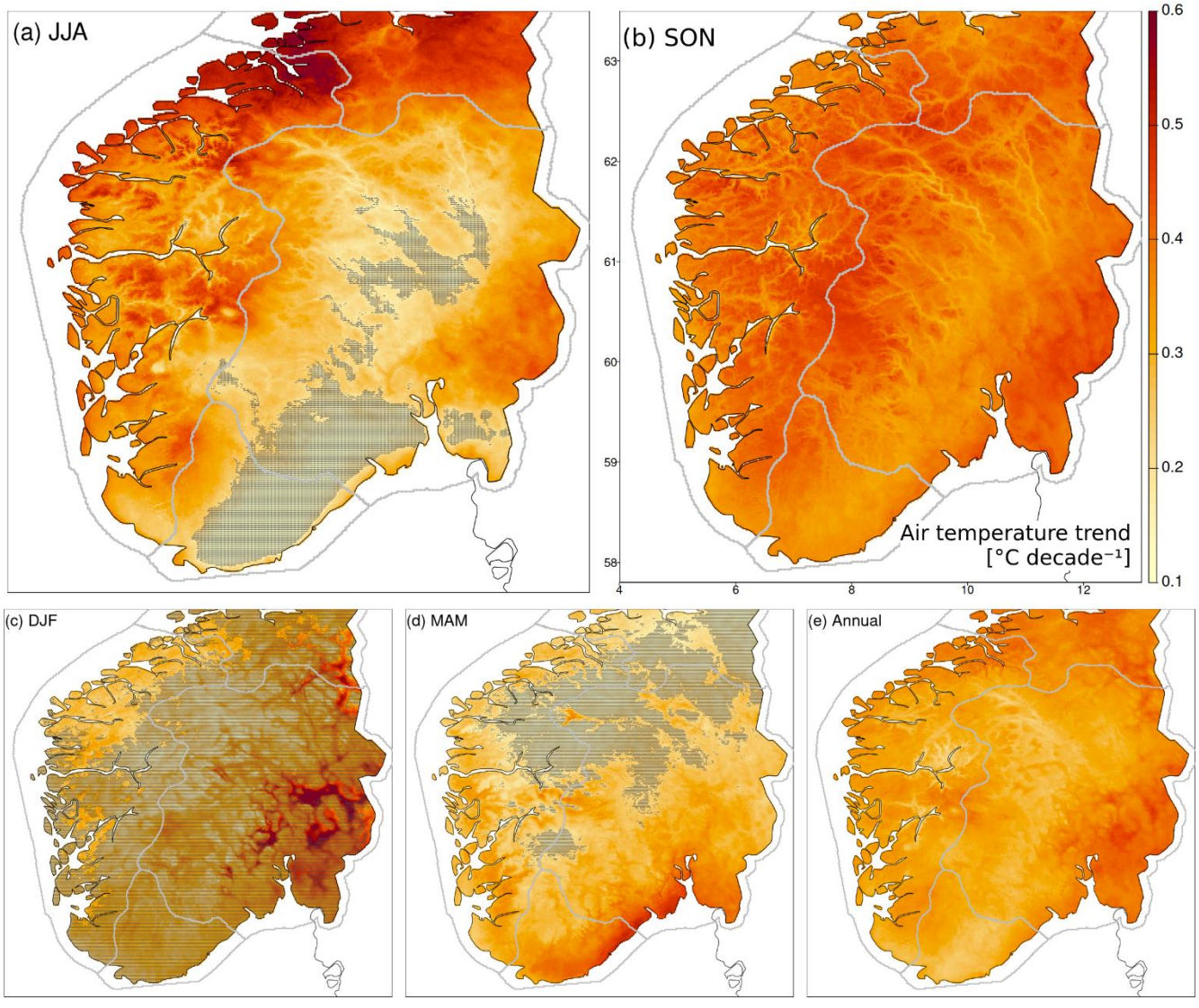


Figure 5. Near-surface air temperature warming trends (1981–2025, °C per decade) across southern Norway from NORA3, for (a) summer (JJA), (b) autumn (SON), (c) winter (DJF), (d) spring (MAM), and (e) the annual mean. Grey stippling marks grid cells where the trend is not significant under a Mann-Kendall test with Benjamini–Hochberg false discovery rate control at $\alpha_FDR = 0.10$, corresponding to a global significance level of 0.05 (Wilks, 2016). Solid grey lines are the boundaries of temperature regions 1 (Eastern Norway), 2 (Southern Norway), and 3 (Western Norway) as defined by Hanssen-Bauer et al. (2022).

To assess the fine-scale altitudinal scaling across Norway's core mountain regions, NORA3 data were analysed over four standardised 1.9° × 1.2° mountain domains centered on the key reference sites: Dovrefjell, Hardangervidda North, Hardangervidda South, and Jotunheimen (Fig. 6). Grouping grid-cell linear trends into 250-m elevation bands reveals clear seasonal EDW contrasts across all mountain domains. Minor distributional irregularities at the lowest and highest elevation

https://doi.org/10.5194/egusphere-2026-5858
Preprint. Discussion started: 4 November 2026
© Author(s) 2026. CC BY 4.0 License.

bins primarily stem from small sample sizes (n < 50), where local topographic features disproportionately distort the kernel density estimates (Fig. 6, C2–C11).

The most continuous and widespread positive EDW pattern occurs during the warm half-year. Autumn (SON) exhibits the strongest, most coherent signal, with median warming trends scaling monotonically with elevation across the alpine and steep mountain domains. Lowland and valley bottom grid cells (<500 m a.s.l.) warmed at 0.30–0.35 °C per decade, while high mountain plateaus and summits (>1500–2100 m a.s.l.) reached peak rates of 0.45–0.50 °C per decade with spatially uniform warming across the upper terrain. Summer (JJA) shows a similar, albeit slightly weaker, positive trend-elevation gradient, with high-alpine peaks warming significantly faster (0.35–0.45 °C per decade) than surrounding lowlands (0.15–0.25 °C per decade).

These altitudinal contrasts are vividly captured in the high-resolution spatial maps (Fig. 6, C3, C10), where warming rates sharply delineate the topography. Deep valleys and fjord systems - such as in Jotunheimen, Romsdalsalpene, and Lyngsalpan - emerge as distinct low-warming corridors, contrasting starkly against the rapidly warming, dark red high-alpine terrain.

In stark contrast, winter (DJF) shows a topographically constrained inverse EDW pattern (Fig. 6). Rapid warming (0.35–0.45 °C per decade) is confined to sheltered interior basins and deep valleys (<500–750 m a.s.l.), while high-elevation areas (>1500 m a.s.l.) show significantly suppressed rates (0.20–0.25 °C per decade). This inverse slope is particularly pronounced in the eastern and southern continental mountain domains (Dovrefjell and Hardangervidda South), where median trends decline sharply above 1000 m a.s.l. Finally, spring (MAM) serves as a transitional period with lower overall warming (0.15–0.30 °C per decade) and muted, complex gradients. While Hardangervidda South retains a weak inverse profile, central massifs like Jotunheimen and Hardangervidda North display slightly humped distributions, with maximum warming concentrated at intermediate forest-line elevations (750–1250 m a.s.l.).

https://doi.org/10.5194/egusphere-2026-5858
Preprint. Discussion started: 4 November 2026
© Author(s) 2026. CC BY 4.0 License.

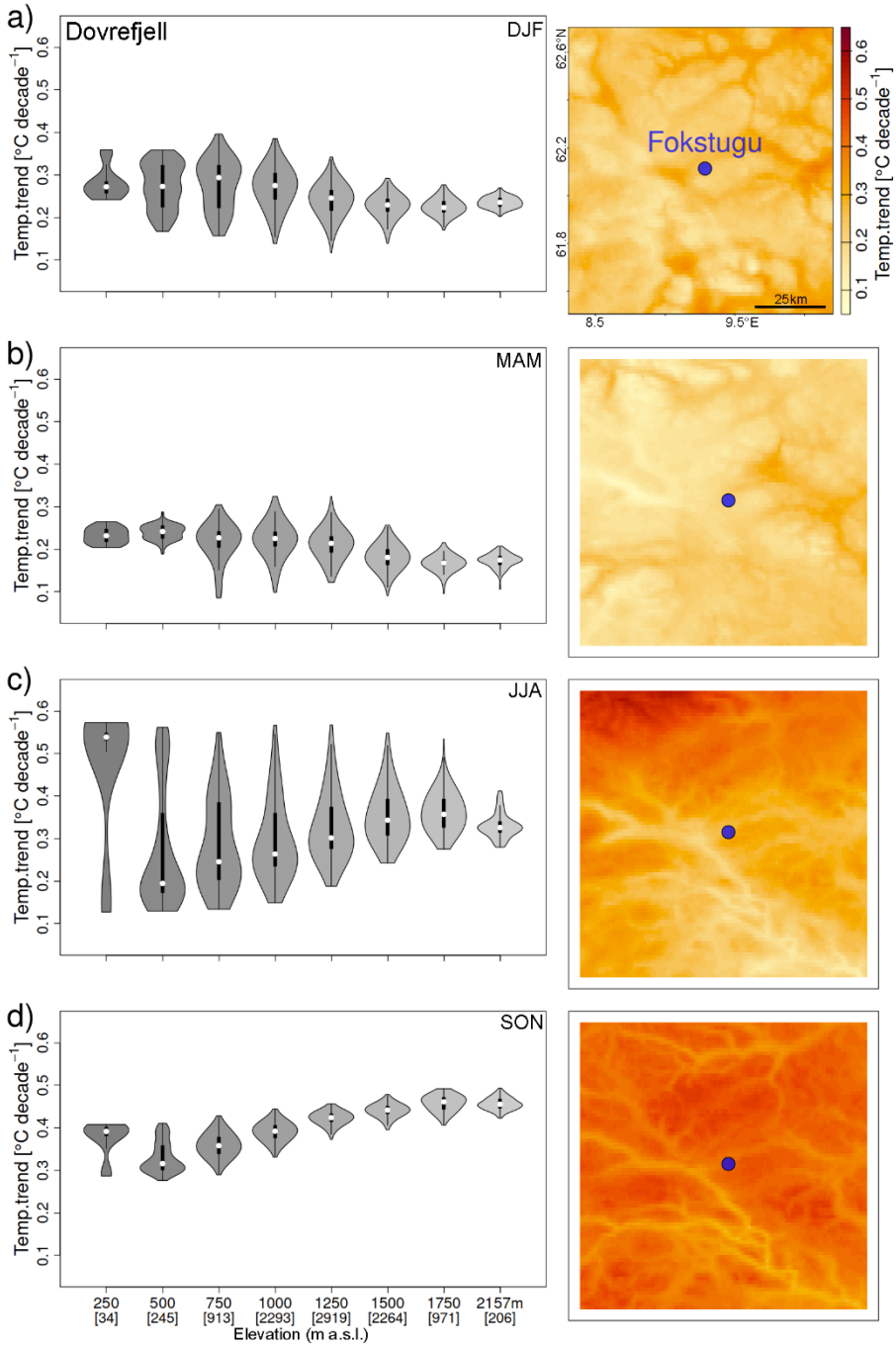


Figure 6a. Seasonal near-surface air temperature trends (°C per decade) over Dovrefjell (8.3–10.2° E, 61.5–62.7° N; centred on Fokstugu, 973 m a.s.l.) from NORA3, 1981–2025, for (a) winter, (b) spring, (c) summer, and (d) autumn. Each panel shows the distribution of grid-cell trends in 250 m elevation bands (left; white dots, medians; black bars, interquartile ranges; n, number of grid cells) and the corresponding spatial trend map (right), with reference stations marked in blue.

https://doi.org/10.5194/egusphere-2026-5858
Preprint. Discussion started: 4 November 2026
© Author(s) 2026. CC BY 4.0 License.

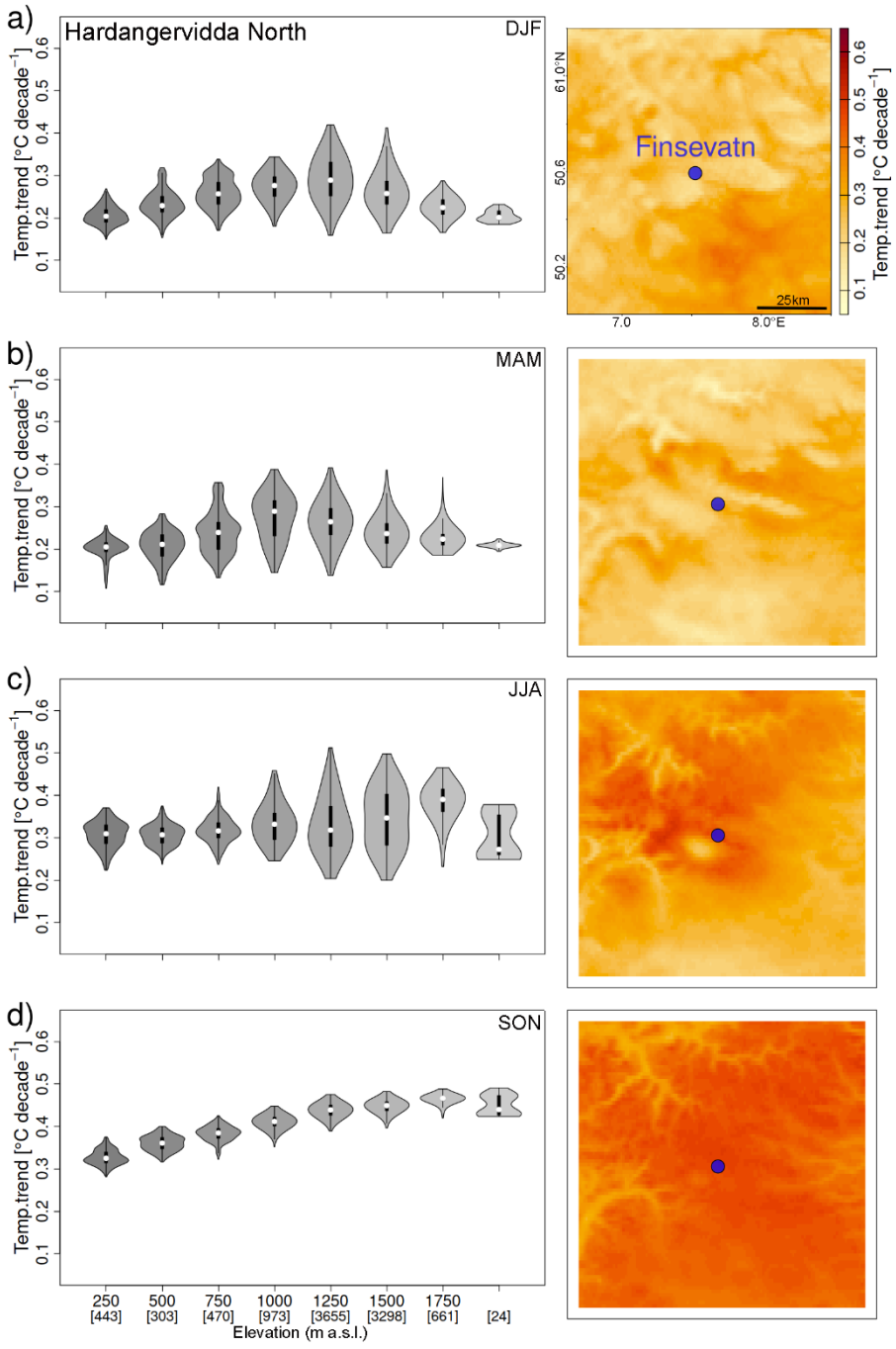


Figure 6b. As Fig. 6a but for Hardangervidda north (6.6–8.5°E, 60.0–61.2°N, Finsevatn, 1210 m a.s.l.).

https://doi.org/10.5194/egusphere-2026-5858
Preprint. Discussion started: 4 November 2026
© Author(s) 2026. CC BY 4.0 License.

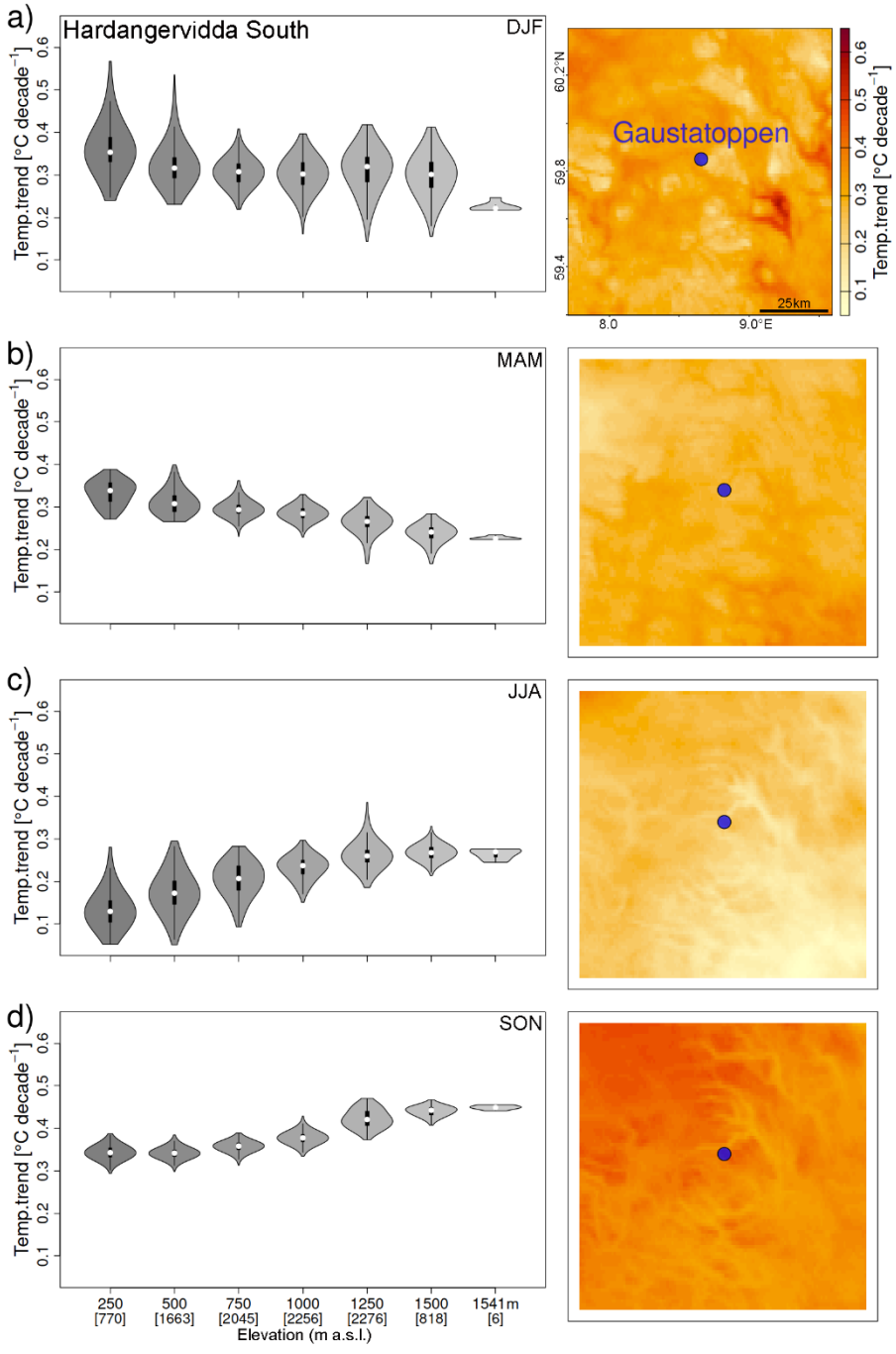


Figure 6c. As Fig. 6a but for Hardangervidda south (7.7–9.6°E, 59.2–60.4°N, Gaustatoppen, 1804 m a.s.l.).

445

https://doi.org/10.5194/egusphere-2026-5858
Preprint. Discussion started: 4 November 2026
© Author(s) 2026. CC BY 4.0 License.

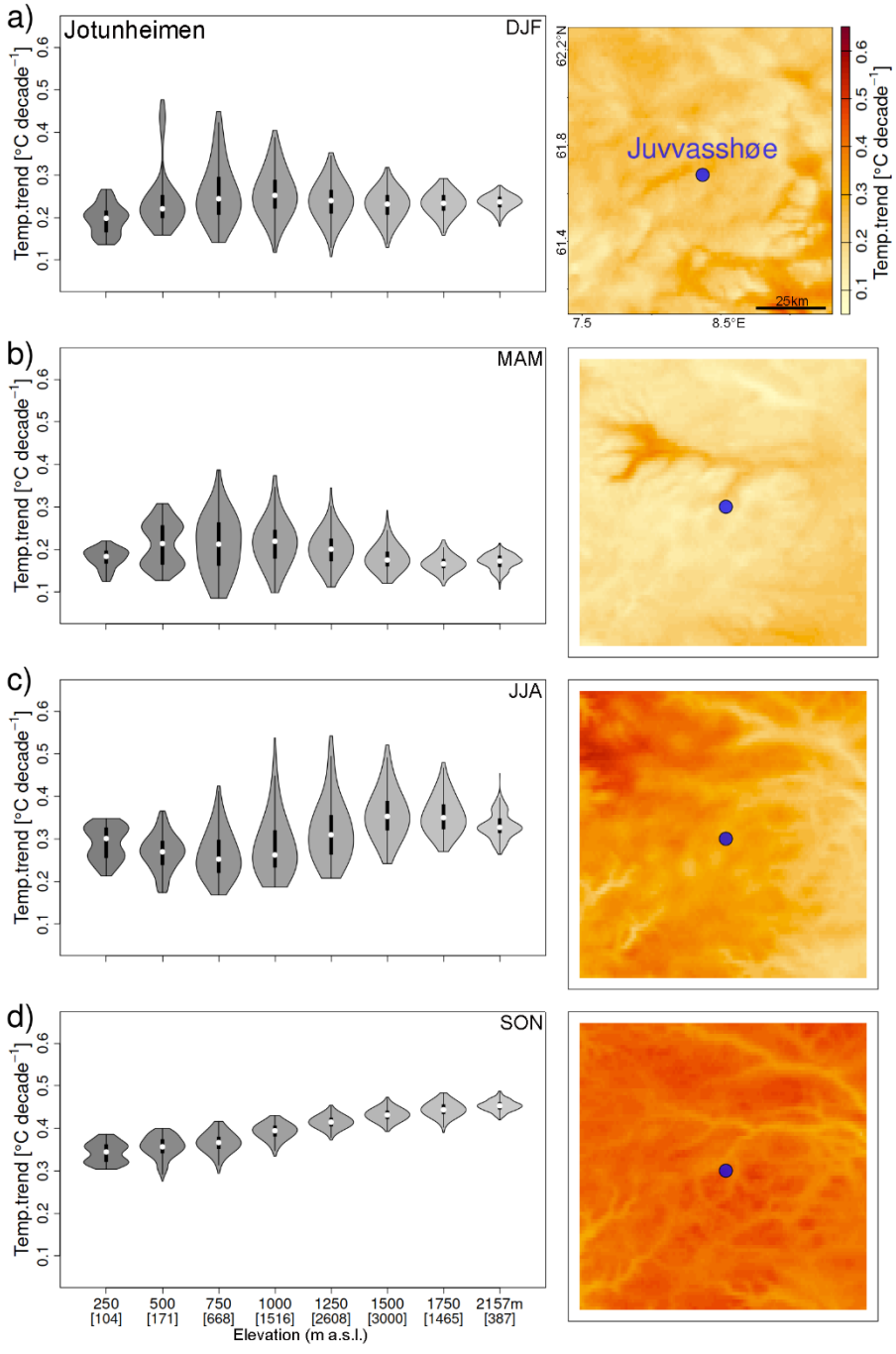


Figure 6d. As Fig. 6a but for Jotunheimen (7.4–9.3°E, 61.1–62.3°N, Juvvasshøe, 1894 m a.s.l.).

450

https://doi.org/10.5194/egusphere-2026-5858
Preprint. Discussion started: 4 November 2026
© Author(s) 2026. CC BY 4.0 License.

An evaluation of the ten supplementary mountain domains (Fig. C2–C11) confirms that these elevation-dependent trends persist across diverse geographic settings, albeit with distinct latitudinal and topographical variations.

During autumn, a positive EDW signal is widespread, and the magnitude of warming increases sharply with latitude. While southern and central massifs (e.g., Romsdalsalpene, Rørosvidda; Fig. C3, C4) exhibit high-elevation warming of 0.40–0.50 °C per decade, northern mountain domains (e.g., Narvikfjellene, Lyngsalpan, Varangervidda; Fig. C7, C10, C11) amplify to exceed 0.60–0.70 °C per decade. Summer (JJA) also features positive altitudinal gradients across interior regions (e.g., Vistfjellan, Finnmarksvidda South; Fig. C5, C8). However, in steep coastal fjord landscapes (e.g., Romsdalsalpene, Meløyalpene; Fig. C3, C6), peak summer warming is often concentrated within the low-lying valley floors.

In winter (DJF), the inverse EDW pattern is mainly restricted to inland, valley-dominated, and high-plateau mountain domains (e.g., Rondane, Rørosvidda, Finnmarksvidda South and East; Fig. C2, C4, C8, C9). Here, lower-elevation basins record prominent warming peaks (0.40–0.75 °C per decade), while upper slopes show significantly lower median trends. Conversely, exposed northern maritime mountain domains (e.g., Narvikfjellene, Lyngsalpan; Fig. C7, C10) deviate considerably, displaying flat or weakly positive winter gradients across all elevations. Finally, spring (MAM) uniformly shows the lowest seasonal warming rates (0.10–0.28 °C per decade) and subdued elevation gradients across all supplementary mountain domains.

3.3. Temporal Consistency and Evaluation of NORA3

3.3.1 Evaluation of NORA3 against KlimGrid, ERA5, and CERRA

The temporal consistency of NORA3 over mainland Norway was assessed against the homogenised KlimGrid dataset, together with the ERA5 and CERRA reanalyses (Fig. 7). For NORA3, the deviation from KlimGrid remains stable over the full record. The linear trend in the monthly deviations is −0.02 °C per decade, and the LOESS-smoothed annual mean deviation stays close to 0.0 °C (Fig. 7a, b). NORA3 therefore reproduces the KlimGrid warming rate of 0.30 °C per decade over 1961–2024 (Fig. 7c).

Because ERA5 and CERRA are coarser than both KlimGrid and NORA3, their smoother orographic representation introduces systematic biases in 2-m temperature fields (Cavalleri et al., 2024). To isolate the temporal signal from these resolution effects, 1961–2025 trends were computed using annual anomalies relative to each dataset's 1991–2020 climatology (Fig. 7d). NORA3 closely tracks KlimGrid throughout the period. Conversely, ERA5 transitions from a relatively cold anomaly in early decades to a warm anomaly recently. While CERRA performs better than ERA5, NORA3 remains the closest match to KlimGrid. The divergences at the beginning of shorter records reflect edge effects in the LOESS smoothing rather than physical differences; when all records are truncated to a common 1991 start, the smoothed curves align closely, as shown in Fig. D1.

Overall, these differences are consistent with how data is assimilated in the production of the three datasets. NORA3 is a dynamical downscaling of ERA5 with a simple data assimilation setup that is frozen throughout the complete period and

https://doi.org/10.5194/egusphere-2026-5858
Preprint. Discussion started: 4 November 2026
© Author(s) 2026. CC BY 4.0 License.

includes only a limited amount of surface observations to adjust soil conditions. In ERA5 and CERRA, data assimilation includes a much larger amount and range of surface and upper-air observations and, to reconstruct finer spatial scales, the assimilation setup is adapted when more observations become available. Thus, the use and impact of observations varies more in time than for NORA3 as the observing network changes, particularly during the dawn of the satellite era. Consequently, NORA3's frozen data assimilation configuration successfully maintains high temporal consistency with long-term homogenised observations.

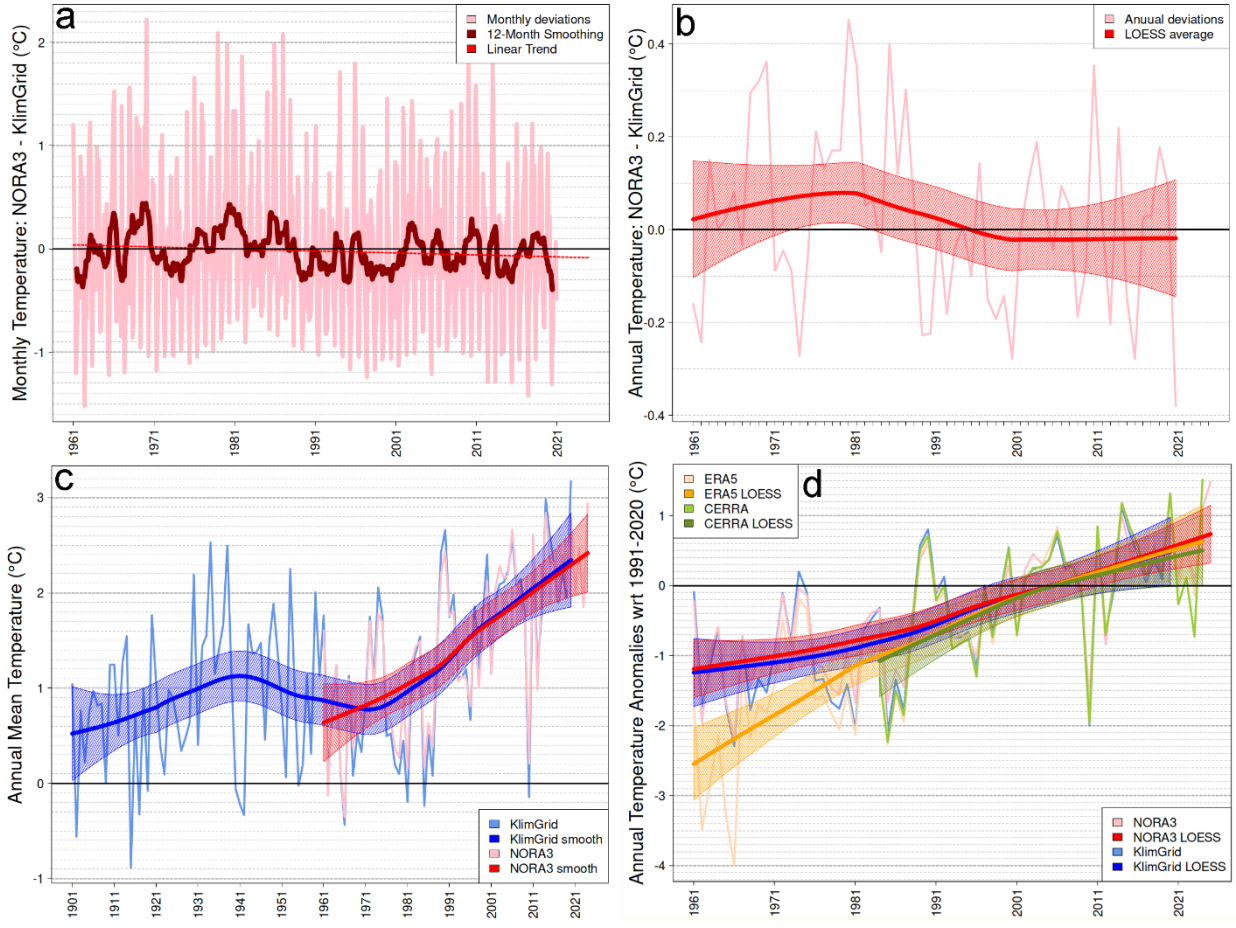


Figure 7. Temporal consistency and decadal trends in NORA3 near-surface air temperature, compared with KlimGrid, ERA5, and CERRA over mainland Norway. (a) Monthly mean differences between NORA3 and KlimGrid, 1961–2024: raw monthly values (pink bars), 12-month running mean (dark red), and linear trend (dashed red; −0.02 °C per decade). (b) Annual mean differences, 1961–2020: yearly values (pink), LOESS fit (thick red), and 95 % confidence interval (hatched band). (c) Annual mean near-surface air temperature from KlimGrid (1901–2020, blue) and NORA3 (1961–2024, red), with LOESS fits. (d) As (c), but as anomalies in respect to 1991-2020 baseline with ERA5 (1961–2024, orange) and CERRA (1985–2020, green) added. LOESS fits and confidence bands are shown in (c) and (d).

https://doi.org/10.5194/egusphere-2026-5858
Preprint. Discussion started: 4 November 2026
© Author(s) 2026. CC BY 4.0 License.



3.3.2 Evaluation of NORA3 Against Mountain Reference Series

Direct point-to-grid benchmarking of NORA3 against the four key mountain reference series (1961–2024) demonstrates high temporal agreement (Fig. D2). NORA3 accurately reproduces interannual variability and multi-decadal LOESS trend trajectories. Minor constant offsets in absolute temperatures are primarily due to sub-grid elevation differences within the 3-km grid cells, alongside local topographic and boundary-layer effects. Monthly temporal covariance remains consistently high across all sites and seasons ($r > 0.87$, predominantly 0.94–0.98; Fig. D3), with minor reductions occurring only during mid-winter at exposed summits (e.g., Juvvasshøe, $r = 0.87$–0.88) and mid-summer at plateaus (e.g., Finsevatn, $r = 0.89$).

When evaluating the 1981–2025 linear warming trends, NORA3 captures annual and autumn (SON) rates with high accuracy across all reference sites (Fig. D4). Autumn trends, for instance, closely match in-situ observations at Gaustatoppen and Juvvasshøe (~0.44–0.45 °C per decade). However, NORA3 tends to underestimate winter (DJF) and spring (MAM) warming at valley and plateau locations (e.g., Fokstugu), as well as summer (JJA) warming at Gaustatoppen. This overall performance is supported by the supplementary regional stations (Fig. D5, D6). These additional sites exhibit similarly high monthly correlations ($r > 0.88$, predominantly 0.94–0.99) and confirm that NORA3 successfully reproduces multi-decadal trajectories, such as at the continental sub-Arctic station Sihccajavri, despite a recurrent slight dampening of cold-season warming rates.

4. Discussion

Early meteorological studies of the Norwegian mountains noted emerging signs of warming by the mid-20th century. Comparing records up to 1946 with the 1901–1930 baseline, Spinnangr and Eide (1948) documented a 0.1 to 0.4 °C annual increase across southern Norwegian high-elevation sites. These early historical findings are consistent with our two longest homogenised mountain series (Fig. 2e, f), which capture a distinct warm anomaly during the 1930s and 1940s - a climatic feature also well-documented in the adjacent Norwegian lowlands (Dyrrdal et al., 2025). However, compared to this mid-century fluctuation, our long-term reference series confirm that warming across Norwegian mountain regions has accelerated in recent decades. Annual warming rates reached 0.39–0.41 °C per decade in southern Norway (1981–2025) and amplified with latitude, reaching 0.55 °C per decade across northern mountain domains (Fig. C1). Beneath these broad trends, the EDW signal shows a distinct seasonal duality: a pronounced inverse EDW pattern dominates sheltered continental valleys in winter, while a robust positive EDW pattern emerges in autumn, alongside a more regionally nuanced positive signal in summer.

4.1 Physical Mechanisms Driving Seasonal Elevation-Dependent Warming

4.1.1 Inverse EDW in Winter

During winter and early spring, a distinct inverse EDW signal emerges across the continental interior, with valleys warming faster than adjacent summits. This lowland enhancement is evident across all investigated spatial scales: from observational station pairs (e.g., Gvarv-Nes at +0.56 °C vs. Gaustatoppen at +0.25 °C per decade; Table 3, Fig. 2, 3), to regional regressions (Fig. B1a), and high-resolution NORA3 reanalysis (Fig. 6a, 6c, C2, C4, C8, C9). Although high interannual, circulation-driven

https://doi.org/10.5194/egusphere-2026-5858
Preprint. Discussion started: 4 November 2026
© Author(s) 2026. CC BY 4.0 License.

variability prevents most winter trends from achieving 5% statistical significance, the strong spatial coherence of this lowland amplification points directly to underlying boundary-layer processes rather than random sampling artifacts.

Two primary mechanisms may explain this wintertime lowland enhancement. First, a diminishing winter snow cover (Nilsen et al., 2025) triggers localised snow-albedo feedbacks at lower elevations, particularly in mild valley and fjord sites operating near the freezing threshold (Hanssen-Bauer & Isaksen, 2026). In contrast, high plateaus (e.g., Finsevatn, Juvvasshøe) maintain near-continuous winter snow cover, completely suppressing such high-elevation albedo feedbacks.

The most extreme winter warming occurs in cold interior basins prone to cold-air pools and radiation driven inversions (Fig. 6a, C4, C9; Dyrrdal et al., 2025). Here, minor snow cover reductions cannot fully explain the rapid warming. Instead, systematic shifts toward higher winter North Atlantic Oscillation (NAO) indices have driven increased cyclonic activity, stronger westerlies, and increased cloudiness (Tajet et al., 2024; Lutz et al., 2024; Ruosteenoja & Räisänen, 2021). This resulting weather pattern likely weakens stratification and erodes inversions (Hanssen-Bauer & Isaksen, 2026). Because these cold-air pools initially form very shallow boundary layers with low effective heat capacity, such circulation shifts trigger a heavily amplified surface temperature response (Davy & Esau, 2016) driving outsized warming in sheltered valley floors beyond what is expected from global background trends alone (Dyrrdal et al., 2025).

4.1.2 Positive EDW in Summer and Autumn

Summer (JJA) and autumn (SON) exhibit a robust positive EDW signal across most regions, with trends peaking in September at approximately +0.7 °C per decade above 1500 m a.s.l. (Fig. 3, 6, B1, B2i). This topographical amplification, where high-alpine regions and mountain plateaus warm faster than adjacent lowlands, is likely strongly influenced by a temporal shift in the snow-free window (Nilsen et al., 2025; Hanssen-Bauer & Isaksen, 2026). At high elevations in Norway, earlier snow and glacier melt (Etzelmüller et al., 2020, 2023; Dyrrdal et al., 2025; Andreassen et al., 2026) coincides with peak solar irradiance, triggering a snow-albedo feedback that acts as a contributing factor. Because lowland areas are already snow-free by early summer, they experience no corresponding albedo shift. This albedo drop at higher elevations transfers substantial sensible heat to the shallow mountain boundary layer. Evidence for this mechanism is further supported by diurnal asymmetry in warming rates: at Fokstugu, daytime maximum temperatures (Tmax) increase significantly faster than nighttime minimums (Tmin), widening the diurnal temperature range by +0.19 °C per decade. This is a classic signature of enhanced daytime shortwave absorption following earlier snowmelt (Rangwala & Miller, 2012; MRI EDW Working Group, 2015).

Operating in synergy with this snow-albedo feedback, long-term atmospheric moistening may serve as a thermodynamic amplifier of high-elevation warming (Fig. 8, Table E1). Over the 1981–2025 period, the atmospheric water vapour mixing ratio (w) increased significantly across the central mountain transect, accelerating from +0.18 g/kg per decade at Fokstugu ($p < 0.001$) to +0.25 g/kg per decade at Sognefjellhytta ($p < 0.0001$), with contemporary records at Juvvasshøe confirming this extends to the highest summits. Because baseline mixing ratio drops sharply with elevation, these modest absolute additions represent disproportionately large fractional increases in cold mountain air. During summer, the relative moistening rate (the fractional increase in mixing ratio, $\Delta w/w$) rose by +3.1% to +4.5% per decade at high-elevation sites,

https://doi.org/10.5194/egusphere-2026-5858
Preprint. Discussion started: 4 November 2026
© Author(s) 2026. CC BY 4.0 License.

compared to +1.6% to +2.3% per decade in lowland fjord valleys. In the optically thin alpine atmosphere, these high fractional gains enhance downwelling longwave radiation far more efficiently than in moisture-saturated lowlands (MRI EDW Working Group, 2015; Pepin et al., 2025).

Because relative humidity at the mountain stations has remained relatively stable, the observed moistening suggests a temperature-driven process that closely tracks theoretical Clausius-Clapeyron scaling (5.7% to 7.0% per K; Fig. 8c, d). As this increasingly moisture-laden air is forced over the mountains, enhanced latent heat release during condensation disproportionately warms higher elevations. This reduces the vertical temperature lapse rate, serving as a main thermodynamic driver for the observed elevation-dependent warming (cf. Ohmura, 2012; Pepin et al., 2025).

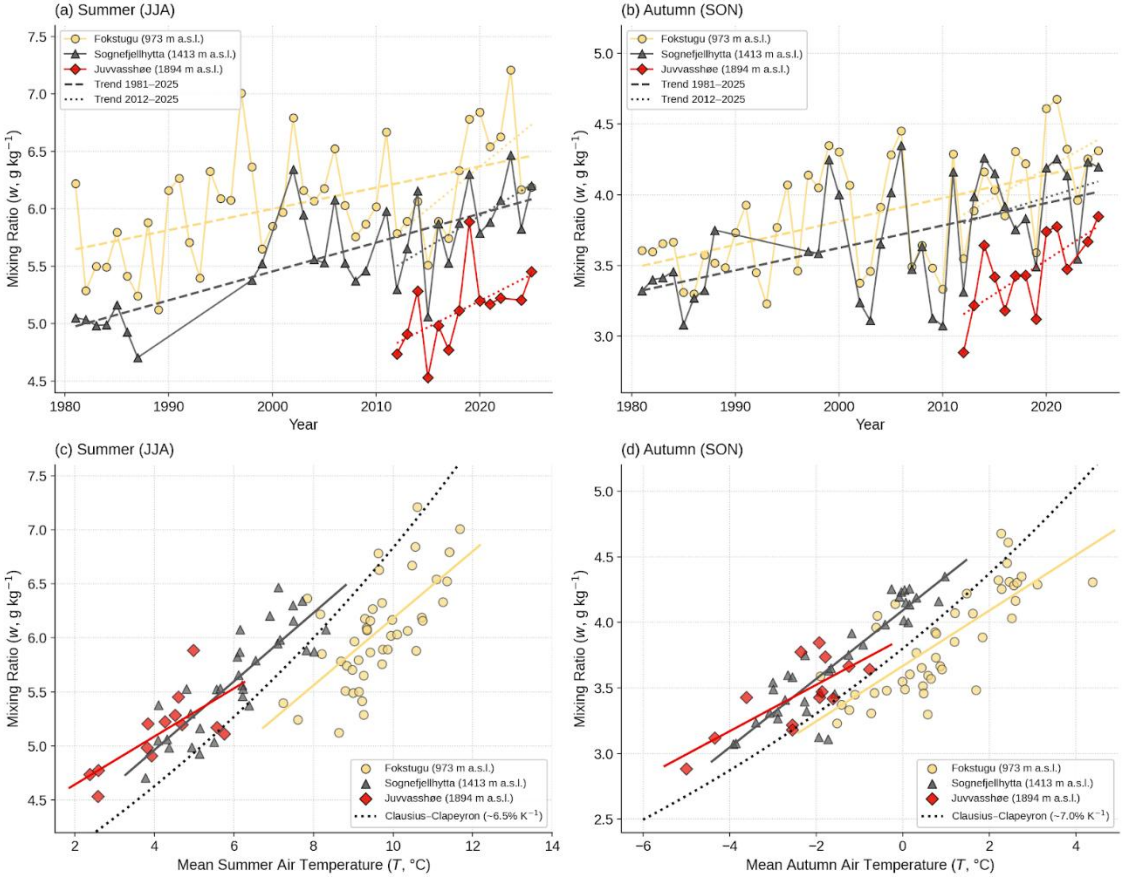


Figure 8. Long-term observations of atmospheric water vapour mixing ratio (w, g kg-1) and temperature sensitivity at key mountain stations in southern Norway (1981–2025). (a, b) Seasonal mean time series of atmospheric water vapour mixing ratio (w) for summer (JJA; a) and autumn (SON; b) at Fokstugu (973 m a.s.l., yellow circles), Sognefjellhytta (1413 m a.s.l., grey triangles), and the high-alpine station at Juvvasshøe (1894 m a.s.l., red diamonds). Dashed lines denote ordinary least-square linear trends over the 1981–2025 period (Fokstugu and Sognefjellhytta); dotted lines denote the 2012–2025 period across all three stations for direct multi-station comparison. (c, d) Empirical relationship between seasonal mean air temperature (T, °C) and atmospheric water vapour mixing ratio (w) during summer (c) and autumn

https://doi.org/10.5194/egusphere-2026-5858
Preprint. Discussion started: 4 November 2026
© Author(s) 2026. CC BY 4.0 License.

(d). Solid colored lines represent empirical linear regressions, and the black dotted curves depict theoretical Clausius-Clapeyron scaling (~6.5% per K for summer and ~7.0% per K for autumn; e.g., Held and Soden, 2006). The Clausius-Clapeyron curves serve solely as relative scaling references to illustrate the expected thermodynamic rate of change, and do not represent absolute saturation limits.These curves are calculated as exponential functions over the observed temperature intervals, with arbitrary vertical anchor points chosen to align the slopes for visual comparison.

4.2 Mechanisms Driving Regional Disparities and Scale-Dependent EDW Signals

The contrasting EDW regimes between Eastern and Western Norway (Fig. 4, 5, B1, B2) reflect a complex interplay of synoptic exposure, boundary-layer dynamics, and regional spatial gradients. In Eastern Norway, the lack of a clear summer and autumn EDW signal in the observational record is largely a methodological artifact of temporal and spatial aggregation. Temporally, intra-seasonal compensation flattens the seasonal aggregate: an anomalous negative trend-elevation slope in June, likely driven by circulation shifts that enhance early-summer radiative cooling and cold-air pooling (Tajet et al., 2024; Dyrrdal et al., 2025), cancels out the positive slopes of July and August (Fig. B2f-h). Consequently, robust positive EDW dynamics are delayed until mid-to-late summer, when background warming accelerates and snowpack depletion and atmospheric moistening triggers strong radiative feedbacks.

Spatially, pooling stations across Eastern Norway's broad zonal transition - from the maritime Oslofjord to the continental interior - introduces severe horizontal scatter (Fig. B3; cf. Tveito, 2023). Because longitudinal position heavily dictates local warming rates (as visualised by the high interior winter warming in NORA3; Fig. 5), a single large-scale regression allows the dominant zonal macro-gradient to artificially mask the vertical signal. This vulnerability to spatial aggregation strongly aligns with global assessments by Wang et al. (2014), who demonstrated that horizontal macro-gradients (such as latitude and longitude) frequently obscure or completely cancel out true altitudinal warming signals if aggregated over broad regions. Crucially, when evaluated at a localised scale, such as pairwise station comparisons (e.g., Gvarv–Gaustatoppen; Fig. 3a) or constrained NORA3 mountain domains (Fig. 6), this horizontal noise is eliminated. At this local scale, distinct vertical dynamics emerge, including summer thermal amplification and sharp winter inversion erosion, proving that elevation-dependent warming is physically present in Eastern Norway. The effectiveness of this localized approach is supported by a global meta-analysis by Pepin et al. (2022), which concluded that while global pooling of stations often obscures elevation-dependent trends, paired comparisons of adjacent high- and low-elevation stations consistently reveal enhanced mountain warming. Conversely, in Western Norway, the maritime-to-alpine transition spans much shorter horizontal distances. Because low-elevation coastal environments are thermally moderated by the marine boundary layer while high-alpine areas (e.g., Sognefjellhytta, Finsevatn) project directly into the free atmosphere, this sharp geographic contrast allows snow-albedo and shortwave absorption feedbacks to operate without being masked by broad zonal gradients. As a result, a positive EDW signal is consistently resolvable during summer and early autumn.

4.3 NORA3 Reanalysis Performance and Trend Stability in Complex Terrain

https://doi.org/10.5194/egusphere-2026-5858
Preprint. Discussion started: 4 November 2026
© Author(s) 2026. CC BY 4.0 License.

High-resolution reanalyses are needed to resolve elevation-dependent warming in complex terrain, but their usefulness for this purpose depends on how stable their trends are in time. As shown in Sect. 3.3.1, ERA5 drifts relative to KlimGrid across the record, and CERRA, while closer to the observations, still departs from them in its early years; NORA3 exhibits no such temporal drift, remaining consistent with KlimGrid over the full period (Fig. 7). Scherrer et al. (2026) report related problems in ERA5 and ERA5-Land for the Alps, where the elevation dependence of warming is misrepresented through an overestimated spring snow-albedo feedback and a failure to capture low-elevation winter warming associated with inversions and low stratus. NORA3's 3-km convection-permitting grid and its SURFEX surface scheme (Masson et al., 2013), combined with a frozen model configuration, retain topographically driven lapse rates that coarser grids smooth out (Haakenstad & Breivik, 2022).

This robust spatial and temporal fidelity is reflected in NORA3's high correlations with the newly established mountain reference series ($r > 0.87$; Fig. D3) and its near 1:1 reproduction of autumn warming trends across all elevations (Fig. D4). However, local boundary-layer processes and sub-grid topographic smoothing still pose limitations. Correlation reductions during mid-winter at exposed summits (e.g., Juvvasshøe), combined with an underestimation of winter and spring warming at valley and plateau locations (e.g., Fokstugu), suggest that shallow surface inversions and highly localised snow-albedo feedbacks remain partially dampened within the reanalysis's surface energy balance scheme (Fig. D3, D4). Consequently, while NORA3 successfully captures broad seasonal EDW shifts, in-situ observations at extreme topographies show even steeper trend-elevation gradients. This ultimate limitation underscores the indispensable value of homogenised, long-term high-elevation records (such as Juvvasshøe and Gaustatoppen) for validating and refining high-resolution climate models in complex terrain. Indeed, recent permafrost monitoring across some of these mountain areas independently corroborates this rapid high-elevation warming, while explicitly warning that extrapolating lowland trends to mountain environments may introduce strong biases precisely due to shifting winter inversions (Etzelmüller et al., 2023). Ultimately, by closing an observational gap across the high-latitude and high-elevation regions of Norway, the four newly established century-scale records will serve as baselines for continuous climate monitoring, long-term analysis, and future research into the impacts of climate change on vulnerable mountain environments.

5. Conclusions

This study provides the first multi-decadal assessment of elevation-dependent warming across Norwegian mountains. By integrating four newly constructed century-scale homogenised high-elevation air temperature series (1904–2025) with a national homogenised station network and the high-resolution NORA3 reanalysis, we quantified multi-decadal warming rates, resolved fine-scale elevation gradients, and examined the underlying physical mechanisms driving mountain climate change in Norway.

The main conclusions of this work are as follows:

– The newly established composite reference series demonstrate strong regional cohesion, with annual warming rates accelerating from 0.16–0.17 °C per decade (1935–2025) to 0.39–0.41 °C per decade over the most recent 45-year period

https://doi.org/10.5194/egusphere-2026-5858
Preprint. Discussion started: 4 November 2026
© Author(s) 2026. CC BY 4.0 License.

(1981–2025). Autumn (SON) and summer (JJA) recorded the highest seasonal warming rates, peaking at the highest summit observatories.

– A robust, widespread positive EDW signal dominates summer and autumn. In autumn, warming rates scale monotonically with elevation across alpine massifs, peaking in high-elevation regions (>0.45–0.50 °C per decade; $p < 0.01$). Similarly, sub-Arctic mountain plateaus experience amplified warming above the climatic forest line.

– While Western Norway shows a statistically significant step-up in high-elevation warming across both summer and autumn, Eastern Norway's summer EDW signal is masked in aggregated observational data due to anomalous early-summer cooling compensating for late-summer warming.

– Winter (DJF) warming is characterised by high interannual variability, which largely masks background trends. However, a distinct, topographically constrained inverse EDW regime emerges in sheltered continental valleys, where likely the erosion of static cold-air pools drives enhanced lowland warming. This inverse pattern is notably absent in exposed maritime and coastal mountain areas.

– Positive summer and autumn EDW is likely driven by the synergy of radiative and moisture feedbacks. Earlier snowpack depletion coincides with peak solar irradiance, triggering a strong localized snow-albedo feedback. Simultaneously, atmospheric moistening in the cold alpine air disproportionately raises water vapour mixing ratio and downwelling longwave radiation, while latent heat release shifts local lapse rates. Conversely, wintertime inverse EDW is driven by atmospheric circulation shifts that increase wind and cloudiness, effectively eroding valley cold-air pools and radiation inversions.

– By accurately reproducing multi-decadal trends ($r > 0.87$–0.99) and topographically constrained lapse rates, NORA3 successfully bridges the alpine observational gap to resolve elevation-dependent warming. It overcomes the trend drifts observed in coarser global reanalyses (e.g., ERA5). Ultimately, our evaluation demonstrates that NORA3's frozen data assimilation yields high temporal consistency with homogenised observations, making such configurations better suited for estimating local and elevation-dependent trends where temporal homogeneity matters.

To place these findings in a broader global context, our results both confirm and add knowledge to the current understanding of elevation-dependent climate change (Pepin et al., 2025). Recent forcing-feedback frameworks based on top-of-atmosphere energy balance demonstrate that the temperature-dependent Planck feedback and the surface albedo feedback are robust drivers that inherently enhance warming over elevated surfaces (Byrne et al., 2024). While these global frameworks predominantly capture signals across tropical and subtropical regions, our observation of a widespread positive EDW during summer and autumn provides high-latitude empirical support for these thermodynamic expectations, particularly the dominance of the snow-albedo feedback (Ohmura, 2012; MRI EDW Working Group, 2015; Byrne et al., 2024). Furthermore, while global top-of-atmosphere analyses suggest that water vapour and cloud feedbacks may oppose large-scale elevation-dependent warming (Byrne et al., 2024), our surface-level observations emphasize that localized atmospheric moistening strongly reinforces warm-season mountain warming through enhanced downwelling longwave radiation.

Our findings also highlight the role of atmospheric circulation. While shifts in large-scale atmospheric circulation and energy transport are known to influence EDW-patterns (e.g. Rangwala & Miller, 2012; Pepin et al., 2022, Byrne et al., 2024),

https://doi.org/10.5194/egusphere-2026-5858
Preprint. Discussion started: 4 November 2026
© Author(s) 2026. CC BY 4.0 License.

our winter records show how regional synoptic shifts - specifically wind-driven erosion of static cold-air pools - can override standard thermodynamic gradients to produce a pronounced inverse EDW regime. This mirrors recent findings from the European Alps, where negative cold-season EDW is driven by a reduction in fog and low stratus clouds (Scherrer et al., 2026), reinforcing that lowland-enhanced warming is a widespread, circulation- and topography-constrained feature in complex terrain.

Methodologically, our evaluation of the high-resolution NORA3 reanalysis corroborates recent findings that coarser global datasets like ERA5 struggle to capture fine-scale EDW patterns and suffer from decadal trend drifts in complex terrain (Scherrer et al., 2026).

Finally, this study presents the first systematic multi-decadal assessment of elevation-dependent warming across high-latitude European mountains. The newly established century-scale records address a persistent mid-latitude and lowland bias in global observational networks (Pepin et al., 2025), providing a baseline for future research into how climate change impacts the cryosphere, ecosystems, and mountain hazards, with profound implications for both nature and society.

Appendix A

Homogeneity analysis of long temperature series from four high-elevation locations in Southern Norway

A homogeneity analysis of monthly temperature series was performed for four locations in mountain areas in southern Norway using the homogenisation software HOMER. Before the homogeneity analysis, suiting networks of neighboring stations (reference stations) were constructed based on data coverage and correlation. Initial quality checks were performed. Some digitisation errors in the series were discovered and corrected, and some outliers were removed. The series were also merged with neighbouring series to get the longest series possible, see Table A1.

HOMER (HOMogenisation softwarE in R) is a homogenisation software that was developed during the European COST action ES0601 and includes features of several relative homogenisation methods (Mestre et al., 2013). A relative method is one that uses networks of neighbouring series (reference series) for the homogeneity break detection in a candidate series. The software also utilises the neighboring series to interpolate data gaps.

The following settings were used in the analysis:

– Additive correction

– Annual and seasonal testing in the pairwise detection

– All series were included in the reference series network (because each reference series had already been chosen beforehand based on correlation)

– After quality control and outlier checks, the homogeneity analysis was conducted in this order:

1. Pairwise detection
2. Joint detection

https://doi.org/10.5194/egusphere-2026-5858
Preprint. Discussion started: 4 November 2026
© Author(s) 2026. CC BY 4.0 License.

3. Correction and interpolation
4. Pairwise detection
5. ACMANT detection
6. Joint detection
7. Correction and interpolation
8. Pairwise detection
9. Correction and interpolation
10. Assess month of change
11. Final correction

A detailed description of HOMER can be found in e.g. Mestre et al. (2013) and Kuya et al. (2020).

Each possible break point detected with HOMER was checked against the available metadata from the historical station archive at MET Norway. This was to help decide whether to accept or reject a possible break point, and also to set the exact time of the break. Some break points did not have metadata to support it, but were still adjusted because the results from the Pairwise/Joint/Acmant detection were considered strong enough.

https://doi.org/10.5194/egusphere-2026-5858
Preprint. Discussion started: 4 November 2026
© Author(s) 2026. CC BY 4.0 License.

Table A1. Station information for the four high-elevation target stations as well as for the reference stations used in the homogeneity analysis. The name of the candidate series is given, and the merged station number and name show which series were included in which periods in the candidate series. For periods with no data, the reference stations were used to interpolate the candidate series. For stations that are still operating, the end date is given as "-".

Name	Merged station number	Merged station name	Altitude (m)	Start (yyyy.mm)	End (yyyy.mm)
Juvvasshøe	55230	Fannaråki	2062	1931.01	1978.08
	15270	Juvvasshøe	1894	1999.09	-
Fokstugu	16600	Fokstua	952	1923.02	1968.05
	16610	Fokstugu	973	1968.06	-
Finsevatn	25840	Finse	1223	1904.01	1924.12
	25900	Slirå	1300	1925.01	1969.08
	25840	Finse	1223	1969.09	1994.06
	25830	Finsevatn	1210	1994.07	-
Gaustatoppen	31970	Gaustatoppen	1828	1934.09	1974.09
	31970	Gaustatoppen	1804	2013.11	-
Reference stations:					
Røros	10380	Røros lufthavn	625	2002.08	-
	10400	Røros	628	1871.01	2002.03
Venabu	13420	Venabu	930	1980.08	-
Skåbu	13655	Skåbu	928	2011.06	-
	13670	Skåbu-Storslåen	890	1968.10	2010.03
Bråtå	15720	Bråtå	712	1965.10	1998.06
	15730	Bråtå-Slettom	664	1998.11	-
Dombås	16540	Dombås-Kirkenær	645	1972.07	1976.05
	16550	Dombås II	643	1870.09	1972.06
	16560	Dombås-Nordigård	638	2006.09	-
	16740	Kjøremsgrende	626	1976.06	2006.08

https://doi.org/10.5194/egusphere-2026-5858
Preprint. Discussion started: 4 November 2026
© Author(s) 2026. CC BY 4.0 License.

Åbjørsbråten	23160	Åbjørsbråten	693	1923.01	2017.12
Geilo	25590	Geilo-Geilostølen	795	1966.09	2005.11
	25600	Geilo II	794	1942.03	1951.10
	25610	Geilo-Strand	768	1951.12	1966.07
	25630	Geilo-Olderbråten	772	2006.11	-
Haugastøl	25720	Haugastøl II	996	1894.01	1940.07
	25730	Haugastøl	988	1940.09	1976.05
Møsstrand	31610	Møsstrand	948	1963.12	1976.04
	31620	Møsstrand II	977	1980.11	-
Midtlæger	46500	Svandalsflona	1048	1920.07	1964.12
	46510	Midtlæger	1079	1967.02	2015.03
Sognefjellhytta	55290	Sognefjellhytta	1413	1978	-
Oppdal	63705	Oppdal-Sæter	604	1999.12	-
	63710	Oppdal-Bjørke	625	1975	1992.08
	66770	Oppdal-Myrhaug	668	1993.10	1999.07

Adjustments

When adjusting breaks, the newest part of the time series is considered the homogeneous part and the level which we want to adjust the older and inhomogeneous parts of the series up or down to. For temperature, the adjustment is added (or subtracted) to the original value.

https://doi.org/10.5194/egusphere-2026-5858
Preprint. Discussion started: 4 November 2026
© Author(s) 2026. CC BY 4.0 License.

Table A2. Adjustments, adjusted period and the metadata for the breaks for the target station Fokstugu. Reference series network: Venabu, Dombås, Oppdal, Skåbu, Sognefjellhytta, Bråtå, Røros, Åbjørsbråten.

	MONTHLY ADJUSTMENTS FOKSTUGU (°C)		
Break	**1968.05**	**1997.07**	**2008.12**
Adjusted period	1923.01-1968.05	1968.06-1997.07	1997.08-2008.12
January	1.3	−0.3	0.4
February	0.8	−0.3	0.4
March	0.5	−0.2	0.3
April	0.3	−0.1	0.2
May	0.2	0.0	0.2
June	0.1	0.0	0.1
July	0.2	0.0	0.1
August	0.3	0.1	0.2
September	0.4	0.1	0.2
October	0.6	−0.1	0.3
November	1.0	−0.2	0.2
December	1.2	−0.3	0.4
	METADATA		
	Relocation from 16600 Fokstua to 16610 Fokstugu.	Automatic temperature sensor (still in wooden radiation screen)	The temperature sensor was moved 90 m S, new temperature screen (circular plastic screen)

https://doi.org/10.5194/egusphere-2026-5858
Preprint. Discussion started: 4 November 2026
© Author(s) 2026. CC BY 4.0 License.

Table A3. Adjustments, adjusted period and the metadata for the breaks for the target station Finsevatn. Reference series network: Fokstugu, Haugastøl, Midtlæger, Åbjørsbråten, Geilo.

MONTHLY ADJUSTMENTS FINSEVATN (°C)				
Break:	**1924.12**	**1936.06**	**1969.08**	**1994.06**
Adjusted period:	1904.01-1924.12	1925.01-1936.06	1936.07-1969.07	1969.08-1994.06
January	-0.6	-0.2	-0.7	-0.3
February	-0.7	-0.3	-0.8	-0.4
March	-0.8	-0.2	-0.5	-0.3
April	-0.8	0.1	-0.2	-0.3
May	-0.6	0.5	0.0	-0.2
June	-0.2	1.0	0.3	0.0
July	0.3	1.4	0.6	0.2
August	0.5	1.6	0.9	0.5
September	0.4	1.5	0.9	0.5
October	0.3	1.2	0.7	0.4
November	0.0	0.7	0.3	0.1
December	-0.4	0.2	-0.3	-0.2
METADATA				
	Relocation from 25840 Finse to 25900 Slirå	The small free-standing screen (Norwegian type) was replaced by a MI-30 free-standing wooden screen and relocated a few meters.	Relocation from 25900 Slirå to 25840 Finse	Relocation from 25840 Finse to 25830 Finsevatn

https://doi.org/10.5194/egusphere-2026-5858
Preprint. Discussion started: 4 November 2026
© Author(s) 2026. CC BY 4.0 License.

Table A4. Adjustments, adjusted period and the metadata for the breaks for the target station Gaustatoppen. Reference series network: Finsevatn, Juvvasshøe, Midtlæger.

MONTHLY ADJUSTMENTS GAUSTATOPPEN (°C)	
Break	1958.07
Adjusted period	**1934.01-1958.07**
January	0.2
February	0.0
March	-0.1
April	-0.2
May	0.0
June	0.0
July	0.0
August	0.3
September	0.4
October	0.5
November	0.4
December	0.3
METADATA	
The temperature screen was rebuilt from MI-30 to MI-33. New extreme thermometers.	

https://doi.org/10.5194/egusphere-2026-5858
Preprint. Discussion started: 4 November 2026
© Author(s) 2026. CC BY 4.0 License.

Table A5. Adjustments, adjusted period and the metadata for the breaks for the target station Juvvasshøe. Reference series network: Fokstugu, Finsevatn, Gaustatoppen, Midtlæger, Sognefjellhytta, Venabu, Skåbu, Åbjørsbråten. The break in 1939 has no clear explanation. The available metadata in the period is very sparse. An inspection report from 1940 says the minimum thermometer had been broken at some point, and that minimum temperatures were taken from the thermograph until a new minimum thermometer came in 1940. The break was adjusted even so, due to clear results in the Pairwise and Acmant run.

MONTHLY ADJUSTMENTS JUVVASSHØE (°C)			
Break	1939.07	1958.08	1978.12
Adjusted period	1931.01-1939.07	1939.08-1958.08	1958.09-1978.12
January	1.9	0.5	-1.5
February	1.3	0.1	-1.8
March	1.1	0.5	-1.2
April	1.1	0.9	-0.5
May	1.8	1.5	0.4
June	2.1	1.8	0.8
July	2.4	2.0	1.1
August	2.3	1.9	1.0
September	2.1	1.7	0.6
October	2.0	1.4	0.1
November	1.9	1.3	-0.4
December	1.9	0.9	-1.1
METADATA			
	Unclear	Relocation of the temperature screen	Merging of Fannaråki and Juvvasshøe

Manned operations on high, isolated summits faced extreme weather conditions. Fannaråken was shrouded in dense clouds for up to 300 days per year. Two year-round observers contended with severe rime icing, extreme winds, and heavy snow accumulation that frequently buried the main entrance. Observers were forced to exit through second-story windows to perform routine 3-hourly readings (Hjortnæs, 1979). Due to these harsh conditions, high maintenance costs, and the advent of radiosonde and satellite technologies, manned summit observatories were gradually decommissioned in the late 20th century (Hjortnæs, 1979). Regular manned observations at Fannaråki ceased in 1978, with monitoring temporarily relocated to Sognefjellhytta (1413 m a.s.l.), located 650 m lower and 7 km northeast. In 1999, an automatic weather and permafrost monitoring site was established at Juvvasshøe (1894 m a.s.l.), 30 km northeast of Fannaråki, as part of the European PACE

https://doi.org/10.5194/egusphere-2026-5858
Preprint. Discussion started: 4 November 2026
© Author(s) 2026. CC BY 4.0 License.

(Permafrost and Climate in Europe) project (Harris et al., 2001; Sollid et al., 2000). Upgraded to an official national weather station in 2009, Juvvasshøe now serves as Norway's highest official meteorological station.

Reconstruction of Missing Monthly Temperature Data for additional key High-Elevation Sites

To ensure continuous and robust climate trend calculations for the period 1981–2025 at high-elevation monitoring sites with incomplete observational records, missing monthly temperature values were reconstructed for Sognefjellhytta (1413 m a.s.l.) and Venabu (930 m a.s.l.). For Sognefjellhytta a total of 93 monthly values were missing within the 1981–2025 window (out of 540 months). The main data gap spanned from June 1989 through August 1997, caused by temporary operational gaps. Additional isolated missing months occurred in 1999 (February) and 2014 (December). For Venabu the observational record was nearly complete, with only 2 missing monthly values identified across the entire 1981–2025 period (April 2007 and July 2007).

Missing values were imputed using month-specific ordinary least squares (OLS) linear regressions based on neighboring high-altitude reference stations showing strong temperature covariance ($R > 0.95$). Regressions were calibrated independently for each calendar month (January-December) to account for seasonal variations in lapse rates. For Sognefjellhytta missing monthly values were imputed using a multiple linear regression model conditioned on observations from the high-elevation reference stations Finse (1210 m a.s.l.) and Fokstugu (973 m a.s.l.). Where one reference station was temporarily unavailable, a single linear regression based on the remaining adjacent site was applied. For Venabu the two missing monthly values (April and July 2007) were reconstructed using a single linear regression model based on corresponding monthly observations from Fokstugu (973 m a.s.l.). Following monthly imputation, seasonal (Winter/DJF, Spring/MAM, Summer/JJA, Autumn/SON) and annual (ANN) mean temperatures were calculated.

https://doi.org/10.5194/egusphere-2026-5858
Preprint. Discussion started: 4 November 2026
© Author(s) 2026. CC BY 4.0 License.

Appendix B

Table B1. Seasonal and annual near-surface air temperature trends (1981–2025, °C per decade) for homogenised observational stations across mainland Norway (Kuya et al., 2020; Tveito, 2021). Listed are station IDs, names, temperature regions (1–7), elevations (m a.s.l.), and decadal trends for winter (DJF), spring (MAM), summer (JJA), autumn (SON), and the annual mean (Year). Asterisks denote statistical significance based on the Mann-Kendall test (* < 0.05, ** < 0.01).

Station ID	Station Name	Region	Elevation (m a.s.l.)	DJF (°C/10yr)	MAM (°C/10yr)	JJA (°C/10yr)	SON (°C/10yr)	Year (°C/10yr)
SN700	DREVSJØ	1	672	0.39	0.32*	0.31**	0.36*	0.36**
SN4780	GARDERMOEN	1	202	0.60	0.43**	0.35**	0.45**	0.47**
SN4920	ÅRNES	1	160	0.53	0.40**	0.38**	0.45**	0.48**
SN5590	KONGSVINGER	1	148	0.64	0.40**	0.39**	0.45**	0.48**
SN6020	FLISA II	1	185	0.57	0.39*	0.38**	0.45**	0.46**
SN7950	RENA FLYPLASS	1	255	0.52	0.37*	0.42**	0.45**	0.47**
SN10380	RØROS LUFTHAVN	4	625	0.44	0.32	0.35**	0.35	0.42**
SN11500	ØSTRE TOTEN – APELSVOLL	1	264	0.47	0.37*	0.33**	0.40**	0.41**
SN12550	KISE PA HEDMARK	1	128	0.50	0.43*	0.42**	0.46**	0.46**
SN12680	LILLEHAMMER – SÆTHERENGEN	1	240	0.53	0.41**	0.34**	0.41*	0.44**
SN13420	VENABU	1	930	0.13	0.31*	0.30**	0.34*	0.28**
SN13655	SKÅBU	1	928	0.34	0.37**	0.32**	0.45**	0.41**
SN15270	JUVVASSHØE	1	1894	0.38	0.31*	0.37**	0.45**	0.39**
SN16560	DOMBÅS – NORDIGARD	1	638	0.34	0.34*	0.36**	0.34	0.36**
SN16610	FOKSTUGU	1	973	0.41	0.35*	0.38**	0.38*	0.39**
SN17150	RYGGE	1	40	0.54	0.46**	0.36**	0.45**	0.46**
SN17850	ÅS	1	92	0.56	0.44**	0.33**	0.45**	0.45**
SN18700	OSLO – BLINDERN	1	94	0.51	0.44**	0.36**	0.40**	0.44**
SN18950	TRYVANNSHØGDA	1	514	0.42	0.44**	0.35**	0.42**	0.41**
SN19710	ASKER	1	163	0.42	0.43**	0.33**	0.40**	0.41**
SN21680	VEST-TORPA II	1	542	0.53*	0.42**	0.37**	0.41**	0.44**
SN23500	LØKEN I VOLBU	1	521	0.39	0.35*	0.36**	0.41**	0.39**
SN24890	NESBYEN – TODOKK	1	166	0.47	0.42**	0.38**	0.46**	0.44**
SN25630	GEILO – OLDEBRÅTEN	1	772	0.27	0.35*	0.32**	0.42**	0.35**
SN25830	FINSEVATN	3	1210	0.40	0.37**	0.40**	0.43**	0.41**
SN27450	MELSOM	1	26	0.55	0.45**	0.34**	0.43**	0.45**
SN27500	FÆRDER FYR	1	6	0.51	0.45**	0.32**	0.41**	0.43**
SN28380	KONGSBERG BRANNSTASJON	1	170	0.45	0.44**	0.36**	0.45**	0.43**
SN29720	DAGALI LUFTHAVN	1	798	0.24	0.34*	0.34**	0.40**	0.34**
SN31620	MØSSTRAND II	1	977	0.39	0.38**	0.31**	0.42**	0.38**
SN31970	GAUSTATOPPEN	1	1804	0.25	0.34*	0.46**	0.47**	0.39**

https://doi.org/10.5194/egusphere-2026-5858
Preprint. Discussion started: 4 November 2026
© Author(s) 2026. CC BY 4.0 License.

SN32060	GVARV - NES	1	93	0.56	0.37**	0.31**	0.42**	0.43**
SN34130	JOMFRULAND	1	3	0.48	0.43**	0.31**	0.42**	0.42**
SN35860	LYNGØR FYR	2	4	0.41	0.43**	0.29**	0.41**	0.40**
SN36200	TORUNGEN FYR	2	12	0.49	0.43**	0.29**	0.41**	0.42**
SN36560	NELAUG	2	142	0.41	0.42**	0.32**	0.45**	0.41**
SN37230	TVEITSUND	1	252	0.56	0.43**	0.33**	0.45**	0.45**
SN38140	LANDVIK	2	6	0.48	0.44**	0.28**	0.40**	0.41**
SN39040	KJEVIK	2	12	0.48	0.44**	0.27**	0.41**	0.41**
SN39100	OKSØY FYR	2	9	0.48	0.43**	0.25**	0.40**	0.40**
SN39750	BYGLANDSFJORD - NESET	2	207	0.50	0.44**	0.32**	0.45**	0.44**
SN41175	LAUDAL - KLEIVEN	2	280	0.47	0.42**	0.32**	0.44**	0.42**
SN41770	LINDESNES FYR	2	16	0.45	0.42**	0.27**	0.41**	0.40**
SN42160	LISTA FYR	2	14	0.44	0.41**	0.28**	0.41**	0.39**
SN44080	OBRESTAD FYR	3	24	0.35	0.39**	0.31**	0.38**	0.37**
SN44560	SOLA	3	7	0.40	0.41**	0.31**	0.38**	0.38**
SN45870	FISTER - SIGMUNDSTAD	3	30	0.39	0.38**	0.32**	0.37**	0.37**
SN46610	SAUDA	3	5	0.21	0.32*	0.34**	0.36**	0.32**
SN46930	VATS I VINDAFJORD	3	20	0.31	0.36**	0.31**	0.38**	0.35**
SN47300	UTSIRA FYR	3	55	0.30	0.38**	0.29**	0.36**	0.34**
SN48330	SLÅTTERØY FYR	3	25	0.31	0.38**	0.30**	0.37**	0.35**
SN50310	KVAMSKOGEN - JONSHØGDI	3	455	0.29	0.34**	0.35**	0.40**	0.35**
SN50500	FLESLAND	3	48	0.31	0.36**	0.32**	0.38**	0.35**
SN50540	BERGEN - FLORIDA	3	12	0.30	0.37**	0.32**	0.37**	0.35**
SN51530	VOSSEVANGEN	3	54	0.26	0.35**	0.34**	0.38**	0.34**
SN52310	MODALEN III	3	125	0.34	0.36**	0.33**	0.39**	0.36**
SN52860	TAKLE	3	38	0.29	0.37**	0.31**	0.38**	0.35**
SN54110	LÆRDAL IV	3	2	0.32	0.34**	0.36**	0.37**	0.36**
SN55290	SOGNEFJELLHYTTA	3	1413	0.34	0.38**	0.44**	0.49**	0.41**
SN55820	FJÆRLAND - BREMUSEET	3	3	0.29	0.34**	0.35**	0.37**	0.34**
SN57770	YTTERØYANE FYR	3	26	0.31*	0.39**	0.30**	0.36**	0.35**
SN58070	SANDANE	3	51	0.15	0.32**	0.34**	0.36**	0.31**
SN59680	ØRSTA-VOLDA LUFTHAMN	3	74	0.35	0.37**	0.35**	0.39**	0.37**
SN60500	TAFJORD	3	11	0.33	0.36**	0.37**	0.40**	0.37**
SN60990	VIGRA	3	22	0.27	0.37**	0.31**	0.38**	0.34**
SN62480	ONA II	3	20	0.37**	0.38**	0.31**	0.38**	0.37**
SN65940	SULA	4	5	0.36*	0.39**	0.31**	0.37**	0.37**
SN68290	SELBU II	4	160	0.26	0.34**	0.35**	0.38**	0.34**
SN69100	VÆRNES	4	12	0.32	0.37**	0.35**	0.41**	0.38**
SN69380	MERÅKER - VARDETUN	4	169	0.38	0.35**	0.37**	0.40**	0.38**
SN70850	SNÅSA - KJEVLIA	4	195	0.51	0.35**	0.36**	0.38**	0.38**

https://doi.org/10.5194/egusphere-2026-5858
Preprint. Discussion started: 4 November 2026
© Author(s) 2026. CC BY 4.0 License.

SN71550	ØRLAND III	4	10	0.37	0.37**	0.31**	0.37**	0.36**
SN71990	BUHOLMRÅSA FYR	4	18	0.33	0.37**	0.29**	0.37**	0.35**
SN75410	NORDØYAN_FYR	4	33	0.36*	0.38**	0.29**	0.36**	0.35**
SN80102	SOLVÆR III	5	10	0.29	0.35**	0.28**	0.35**	0.33**
SN80610	MYKEN	5	17	0.32	0.37**	0.27**	0.36**	0.34**
SN80700	GLOMFJORD	5	39	0.34	0.34**	0.34**	0.38**	0.36**
SN82290	BODØ VI	5	16	0.32	0.34**	0.29**	0.38**	0.34**
SN85380	SKROVA FYR	5	14	0.32*	0.35**	0.29**	0.38**	0.34**
SN85890	RØST LUFTHAVN	5	4	0.37**	0.38**	0.28**	0.38**	0.36**
SN86740	BØ I VESTERÅLEN III	5	8	0.31*	0.36**	0.29**	0.38**	0.35**
SN87110	ANDØYA	5	10	0.33*	0.35**	0.29**	0.39**	0.35**
SN88690	HEKKINGEN FYR	5	33	0.35*	0.35**	0.29**	0.39**	0.35**
SN89350	BARDUFOSS	5	76	0.34	0.34**	0.35**	0.42**	0.37**
SN89940	DIVIDALEN II	5	204	0.44	0.35**	0.38**	0.44**	0.41**
SN90450	TROMSØ	5	100	0.33*	0.35**	0.31**	0.40**	0.36**
SN90490	TROMSØ - LANGNES	5	8	0.32	0.35**	0.31**	0.40**	0.36**
SN90800	TORSVÅG FYR	5	21	0.35*	0.36**	0.30**	0.41**	0.36**
SN91380	SKIBOTN II	5	20	0.42*	0.37**	0.36**	0.45**	0.41**
SN91740	SØRKJOSEN LUFTHAVN	5	6	0.41	0.37**	0.35**	0.44**	0.40**
SN92350	NORDSTRAUM KVÆNANGEN	I 5	20	0.35	0.38**	0.36**	0.43**	0.39**
SN93140	ALTA LUFTHAVN	6	3	0.41	0.38**	0.39**	0.45**	0.42**
SN93301	SUOLOVUOPMI - LULIT	6	381	0.67**	0.44**	0.49**	0.59**	0.55**
SN93700	KAUTOKEINO	6	307	0.59	0.42**	0.49**	0.57**	0.52**
SN93900	SIHCCAJAVRI	6	382	0.62*	0.41**	0.51**	0.58**	0.53**
SN94500	FRUHOLMEN FYR	5	13	0.34*	0.36**	0.31**	0.40**	0.36**
SN95350	BANAK	6	5	0.54*	0.42**	0.41**	0.54**	0.48**
SN96400	SLETTNES FYR	7	8	0.47**	0.36**	0.32**	0.42**	0.39**
SN97251	KARASJOK MARKANNJARGA	- 6	131	0.60	0.43**	0.49**	0.57**	0.53**
SN97350	CUOVDDATMOHKKI	6	286	0.55	0.41**	0.48**	0.56**	0.50**
SN98400	MAKKAUR FYR	7	9	0.35	0.35**	0.32**	0.40**	0.38**
SN98550	VARDØ RADIO	7	10	0.50**	0.37**	0.33**	0.44**	0.42**
SN99370	KIRKENES LUFTHAVN	6	89	0.58*	0.42**	0.46**	0.55**	0.51**

865

https://doi.org/10.5194/egusphere-2026-5858
Preprint. Discussion started: 4 November 2026
© Author(s) 2026. CC BY 4.0 License.

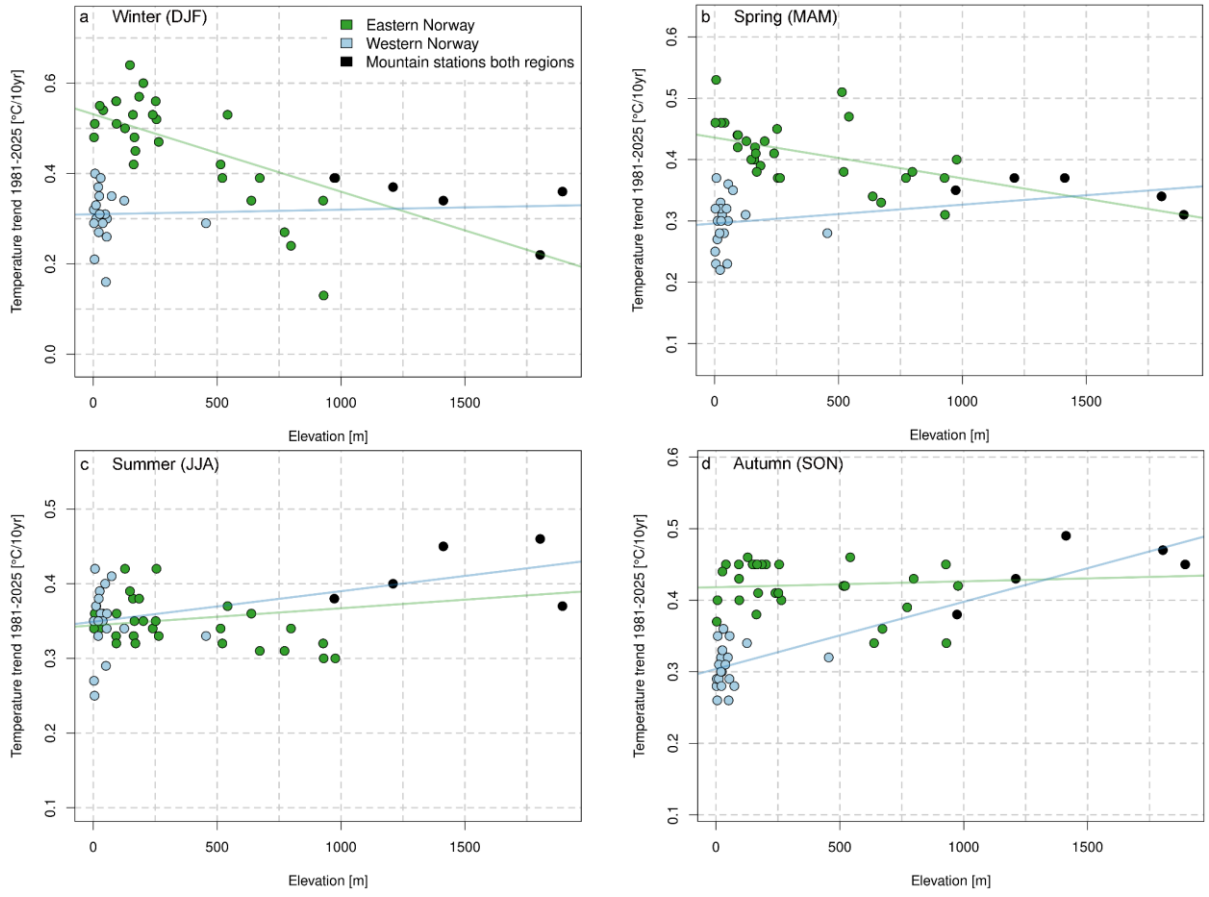


Figure B1. Seasonal surface air temperature trends (°C per decade) for the period 1981–2025 as a function of elevation (m a.s.l.) for high-quality weather station series in Eastern Norway (green circles) and Western Norway (blue circles). To address the scarcity of high-elevation observations along the main alpine divide, five primary high-elevation reference stations (Finsevatn, Fokstugu, Gaustatoppen, Juvvasshøe, and Sognefjellhytta) are included for both regions (black circles). Panels show: (a) winter (DJF), (b) spring (MAM), (c) summer (JJA), and (d) autumn (SON). Solid lines show ordinary least-squares (OLS) linear regression fits to highlight regional elevation-trend gradients.

https://doi.org/10.5194/egusphere-2026-5858
Preprint. Discussion started: 4 November 2026
© Author(s) 2026. CC BY 4.0 License.

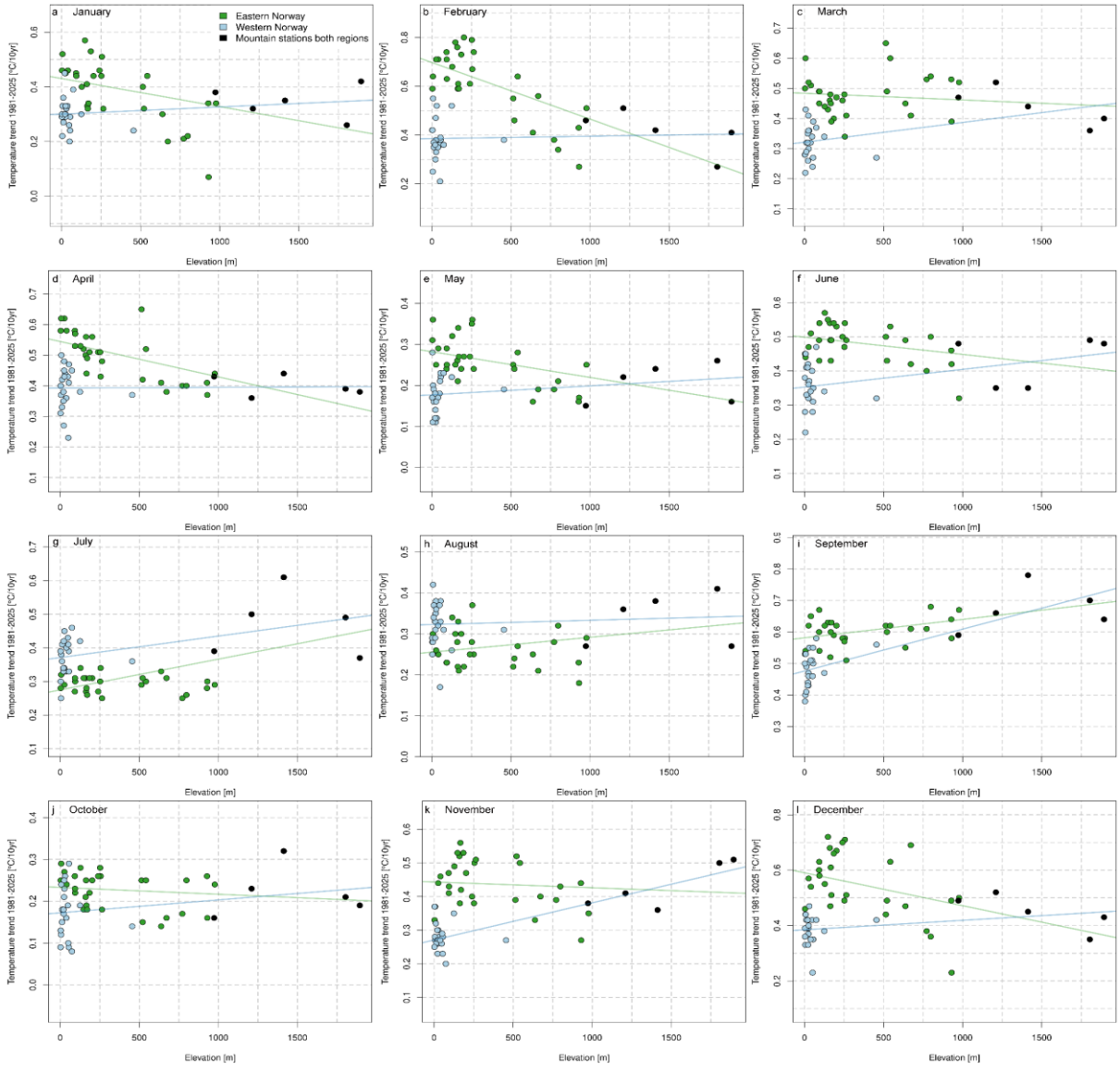


Figure B2. Linear monthly surface air temperature trends (1981–2025) versus station elevation across Eastern Norway (green circles) and Western Norway (blue circles) for all twelve calendar months. As in Fig. C, the five primary high-elevation reference stations along the main alpine divide are included for both regions (black circles). Panels show: (a) January, (b) February, (c) March, (d) April, (e) May, (f) June, (g) July, (h) August, (i) September, (j) October, (k) November, and (l) December. Solid lines display ordinary least-squares (OLS) linear regression fits.

https://doi.org/10.5194/egusphere-2026-5858
Preprint. Discussion started: 4 November 2026
© Author(s) 2026. CC BY 4.0 License.

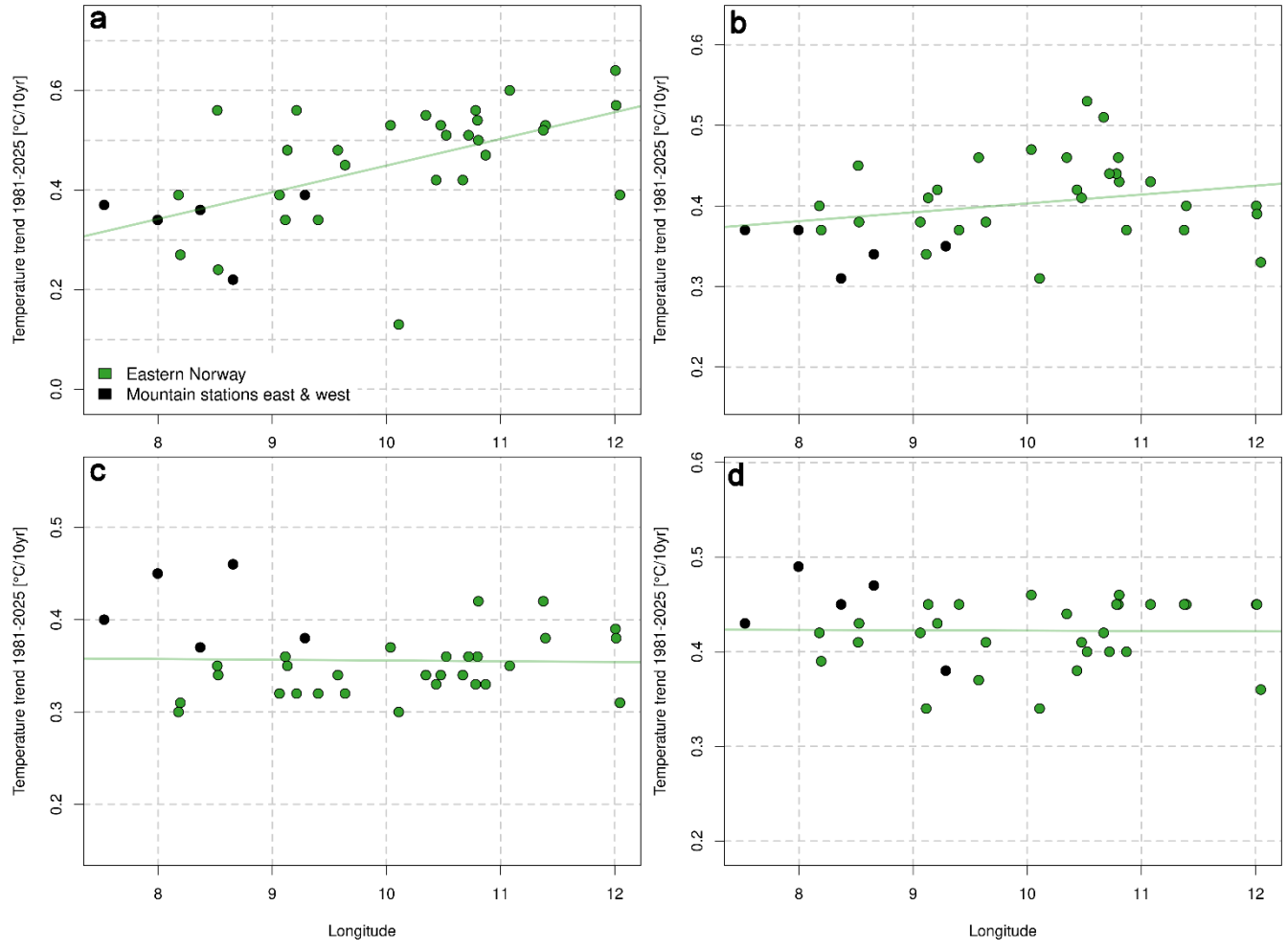


Figure B3. Seasonal surface air temperature trends (1981–2025) versus station longitude across Eastern Norway for: (a) winter (DJF), (b) spring (MAM), (c) summer (JJA), and (d) autumn (SON). Green circles represent individual observational weather stations. Solid light-green lines depict ordinary least-squares (OLS) linear regressions along the zonal gradient (Longitude in °E). Note the steep positive zonal slope during winter (a), reflecting significantly higher warming trends in the continental eastern valleys (11.5–12.0°E) compared to the western regional margins (8.0–9.0 °E), alongside weak positive slopes in spring (b) and summer (c), and a nearly flat relationship in autumn (d).

https://doi.org/10.5194/egusphere-2026-5858
Preprint. Discussion started: 4 November 2026
© Author(s) 2026. CC BY 4.0 License.

Appendix C

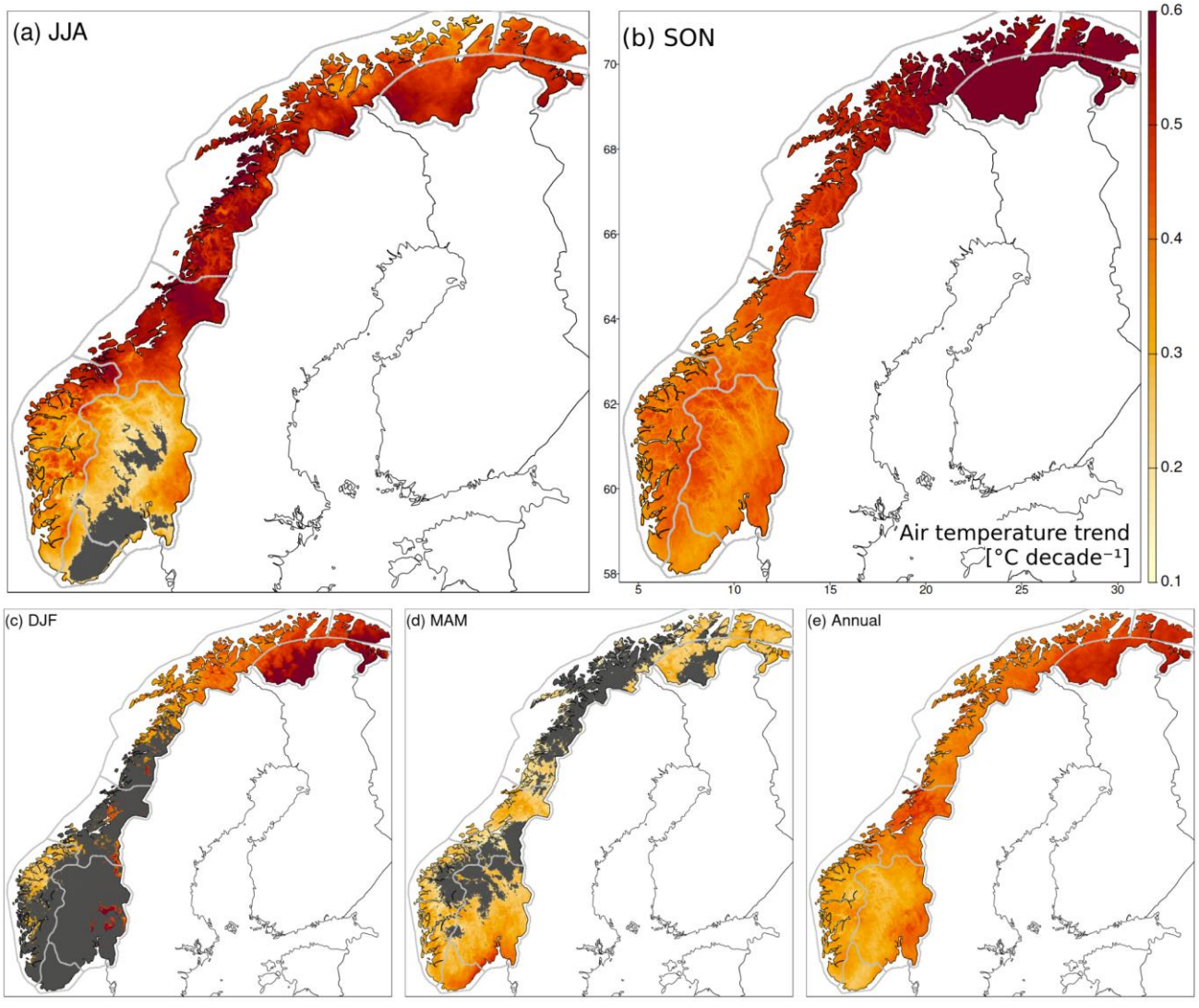


Figure C1. Seasonal and annual near-surface air temperature trends (°C per decade) across mainland Norway for the period 1981–2025. The layout and statistical significance masking (dark grey, $p > 0.05$) are identical to Fig. 5. This national-scale expansion illustrates the pronounced latitudinal warming gradient towards the Arctic, while confirming that the positive EDW signal over mountainous terrain remains robust on a country-wide scale, particularly during summer (a) and autumn (b).

https://doi.org/10.5194/egusphere-2026-5858
Preprint. Discussion started: 4 November 2026
© Author(s) 2026. CC BY 4.0 License.

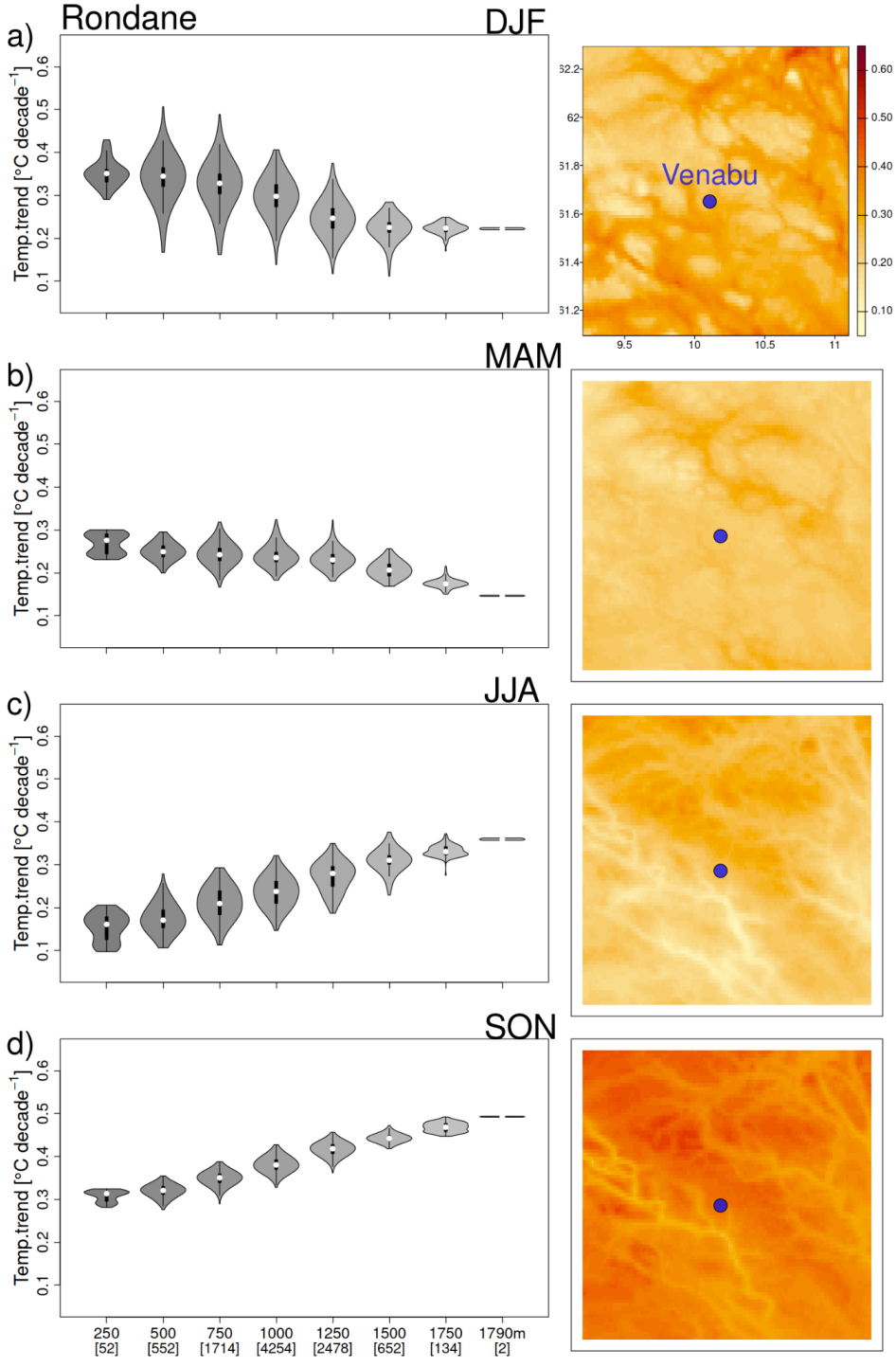


Figure C2. Rondane (Venabu, ~61.7°N).

https://doi.org/10.5194/egusphere-2026-5858
Preprint. Discussion started: 4 November 2026
© Author(s) 2026. CC BY 4.0 License.

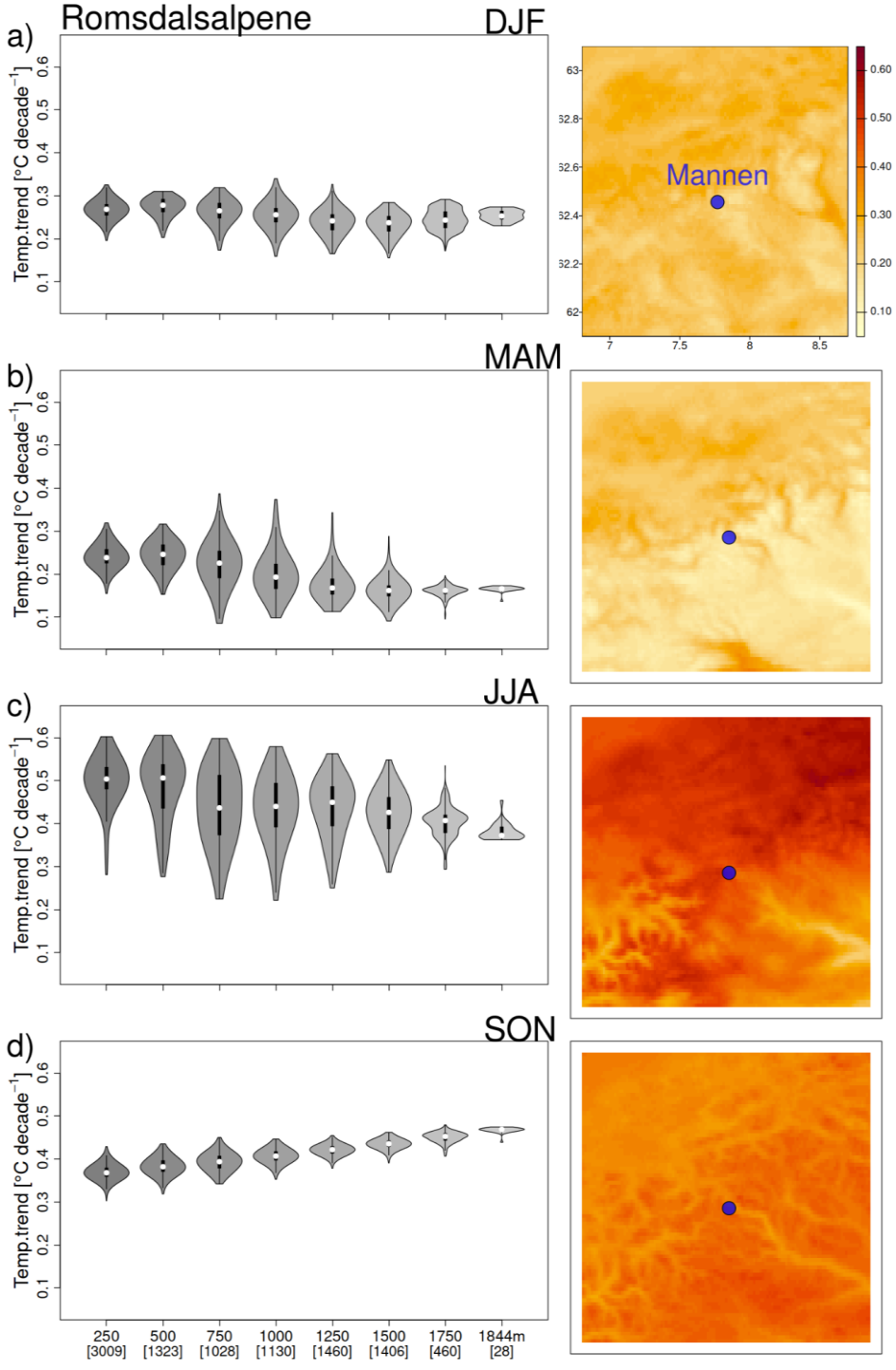
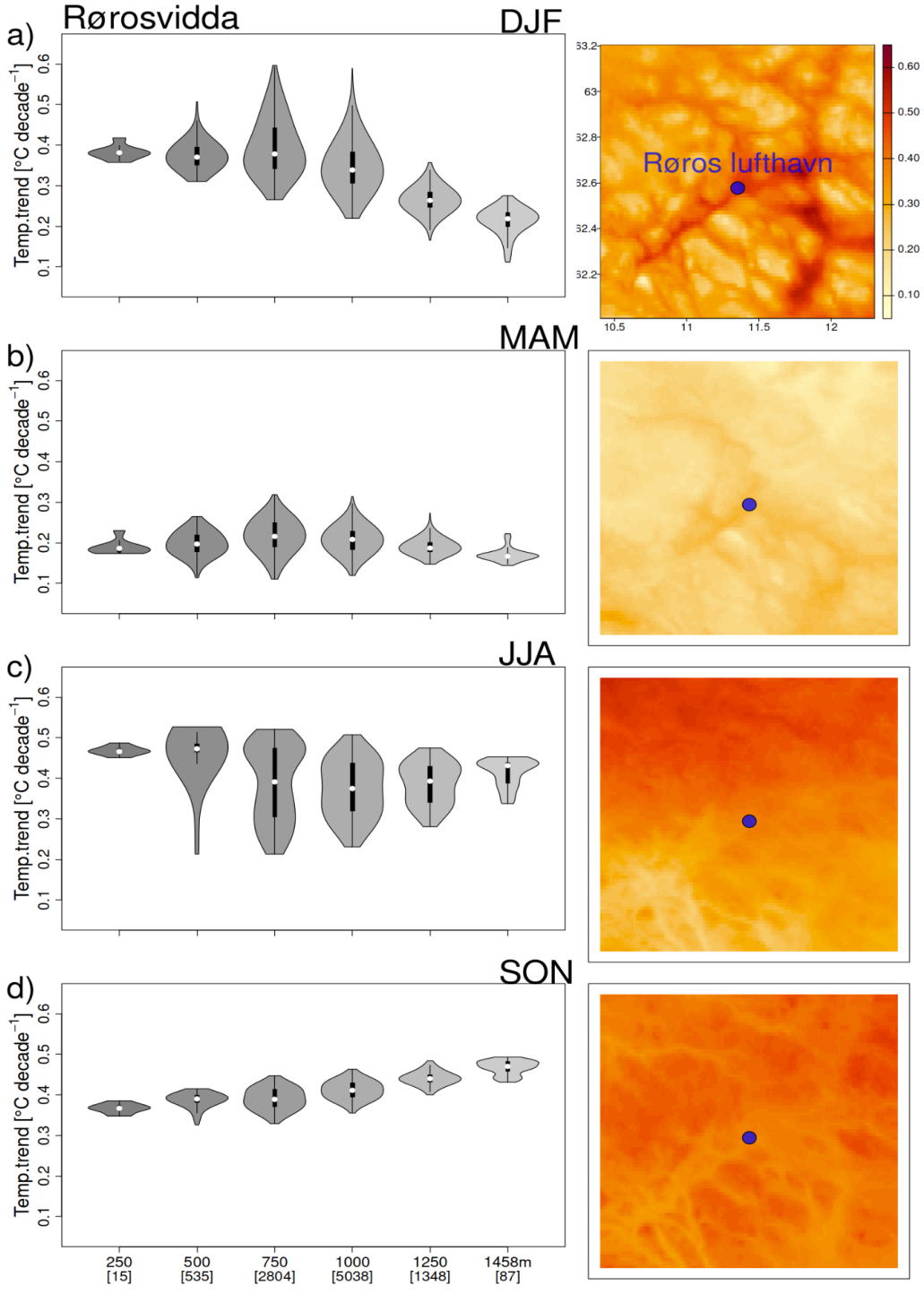


Figure C3. Romsdalsalpene (Mannen, ~62.5°N).

https://doi.org/10.5194/egusphere-2026-5858
Preprint. Discussion started: 4 November 2026
© Author(s) 2026. CC BY 4.0 License.



910 **Figure C4.** Rørosvidda (Røros lufthavn, ~62.6°N).

https://doi.org/10.5194/egusphere-2026-5858
Preprint. Discussion started: 4 November 2026
© Author(s) 2026. CC BY 4.0 License.

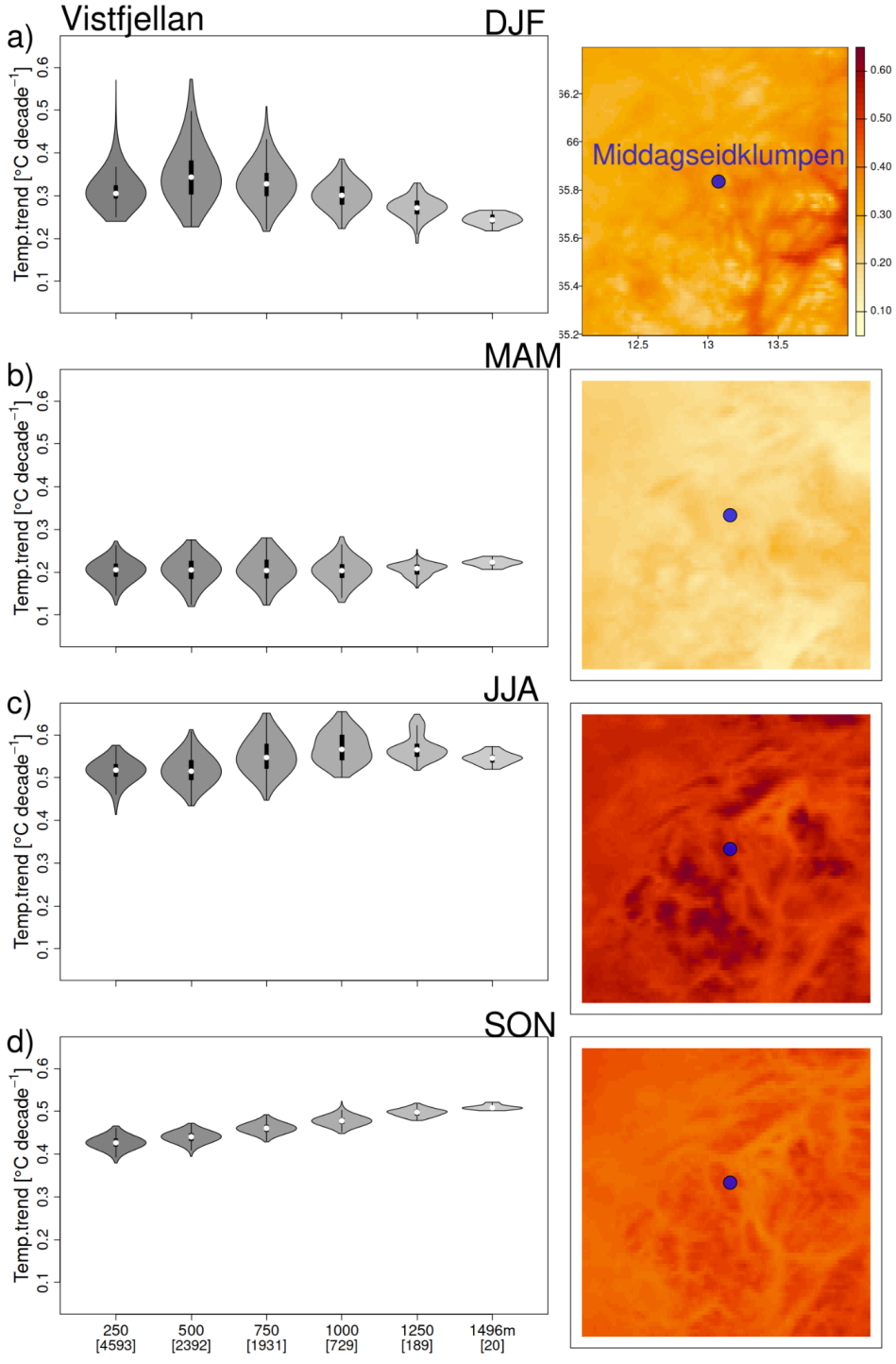


Figure C5. Vistfjellan (Middagseidklumpen, ~65.8°N)

https://doi.org/10.5194/egusphere-2026-5858
Preprint. Discussion started: 4 November 2026
© Author(s) 2026. CC BY 4.0 License.

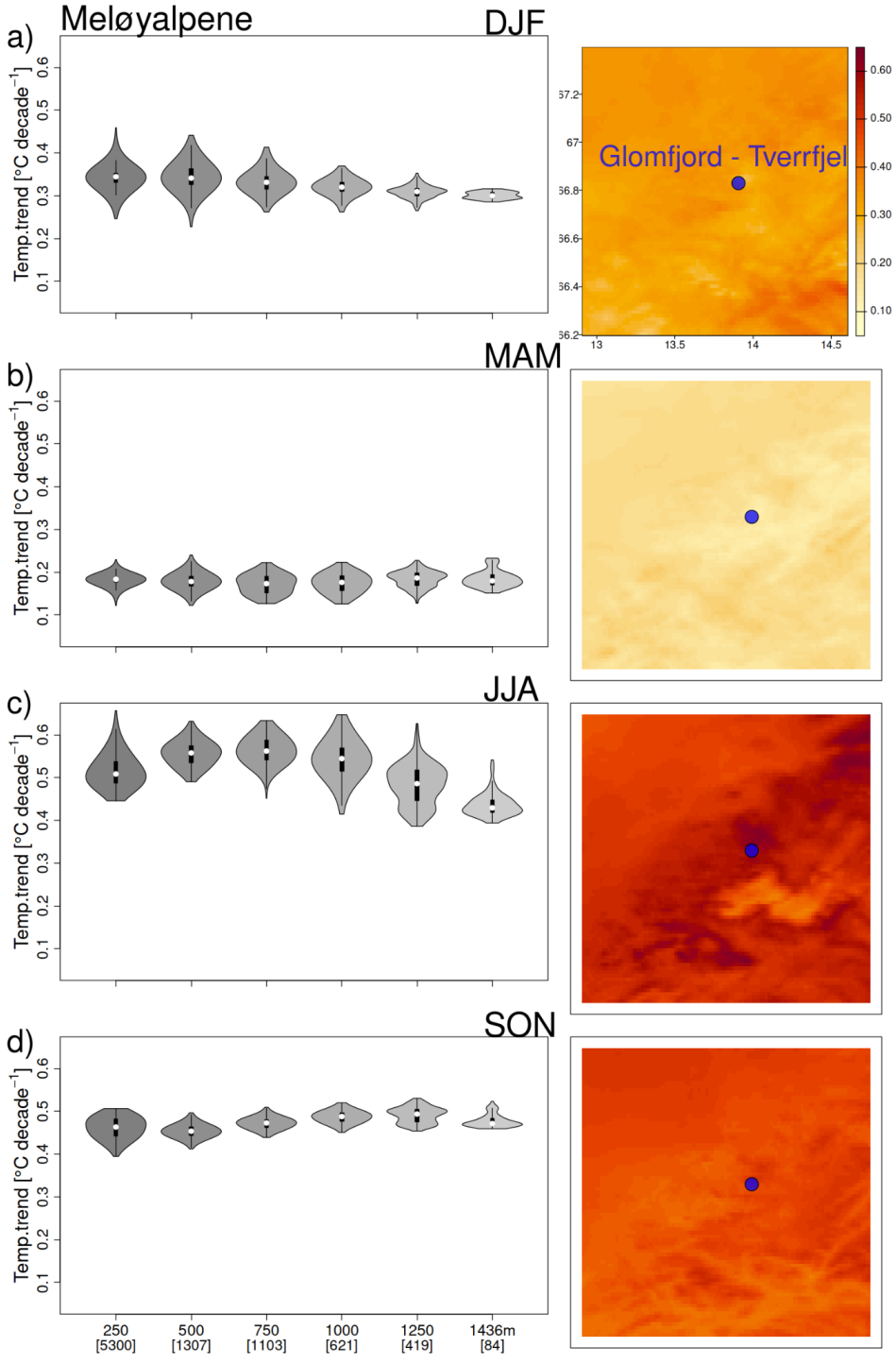


Figure C6. Meløyalpene (Glomfjord - Tverrfjellet, ~66.8°N).

https://doi.org/10.5194/egusphere-2026-5858
Preprint. Discussion started: 4 November 2026
© Author(s) 2026. CC BY 4.0 License.

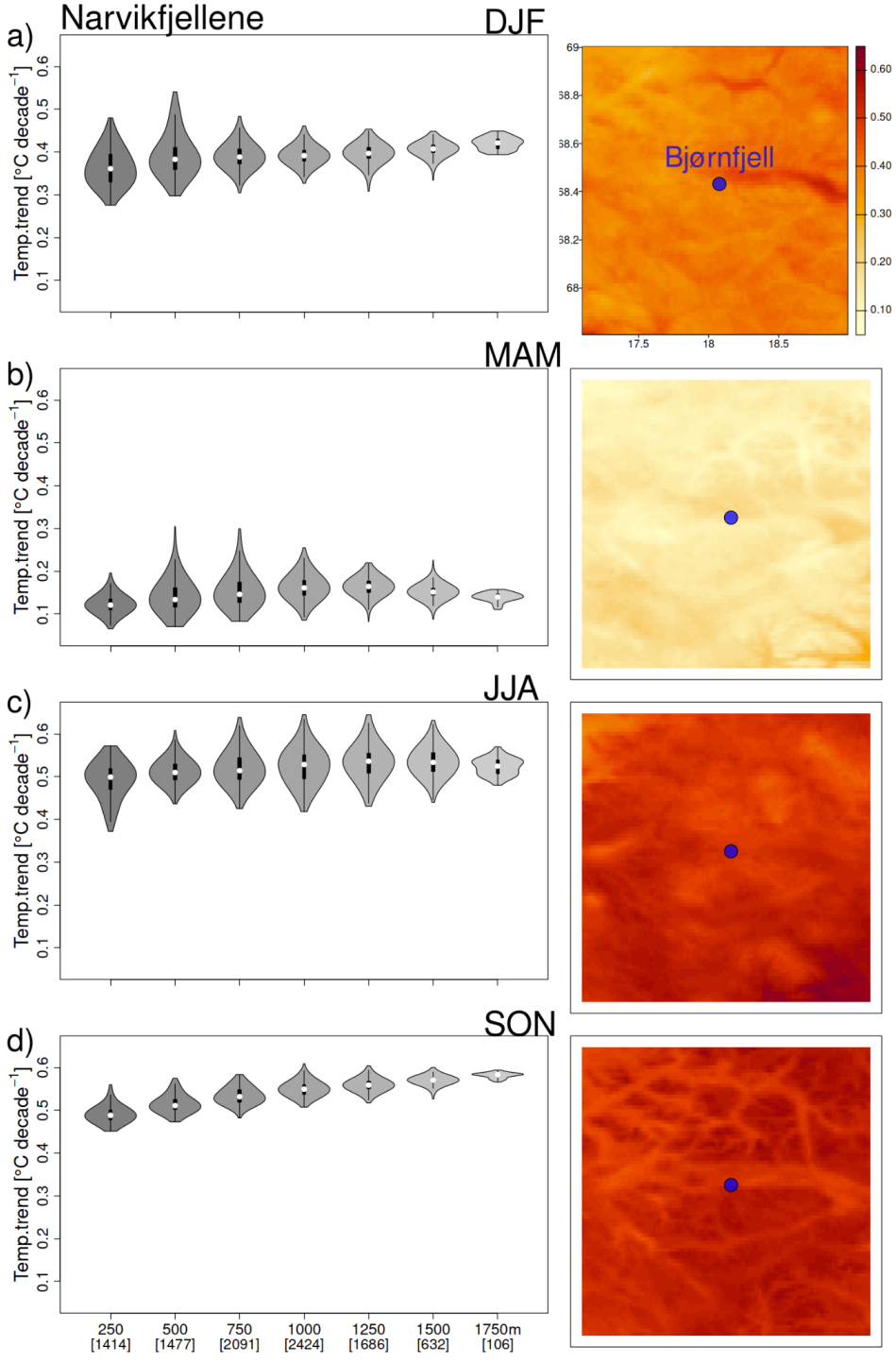


Figure C7. Narvikfjellene (Bjørnfjell, ~68.4°N)

https://doi.org/10.5194/egusphere-2026-5858
Preprint. Discussion started: 4 November 2026
© Author(s) 2026. CC BY 4.0 License.

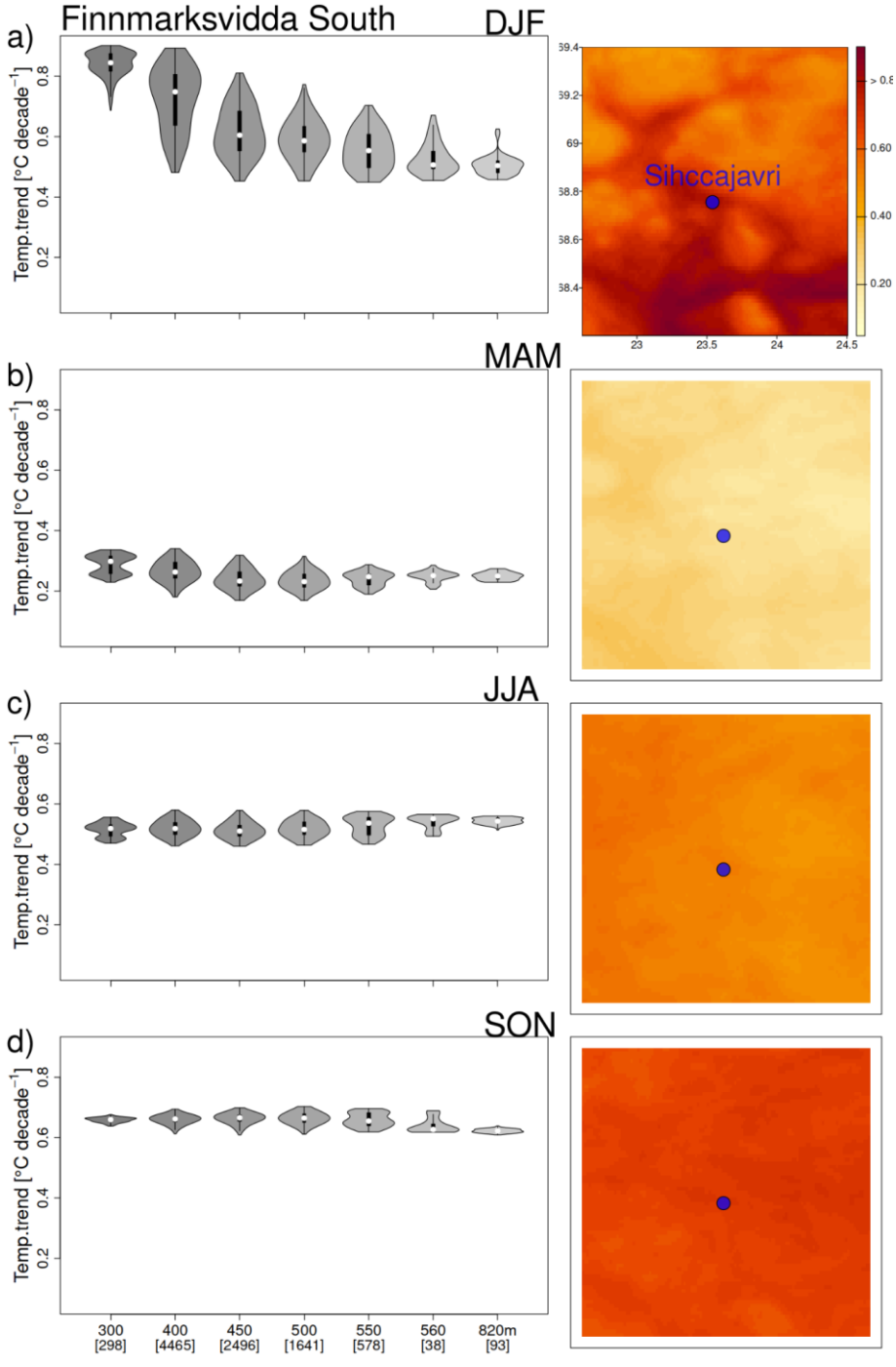


Figure C8. Finnmarksvidda south (Sihccajavri, ~68.8°N). Note that the data are grouped into 100 m elevation bands and utilize an expanded y-axis scale (0.0–0.9 °C per decade) for the temperature trends, compared to the 250 m bands and 0.0–0.7 °C per decade scale applied in the other regions

https://doi.org/10.5194/egusphere-2026-5858
Preprint. Discussion started: 4 November 2026
© Author(s) 2026. CC BY 4.0 License.

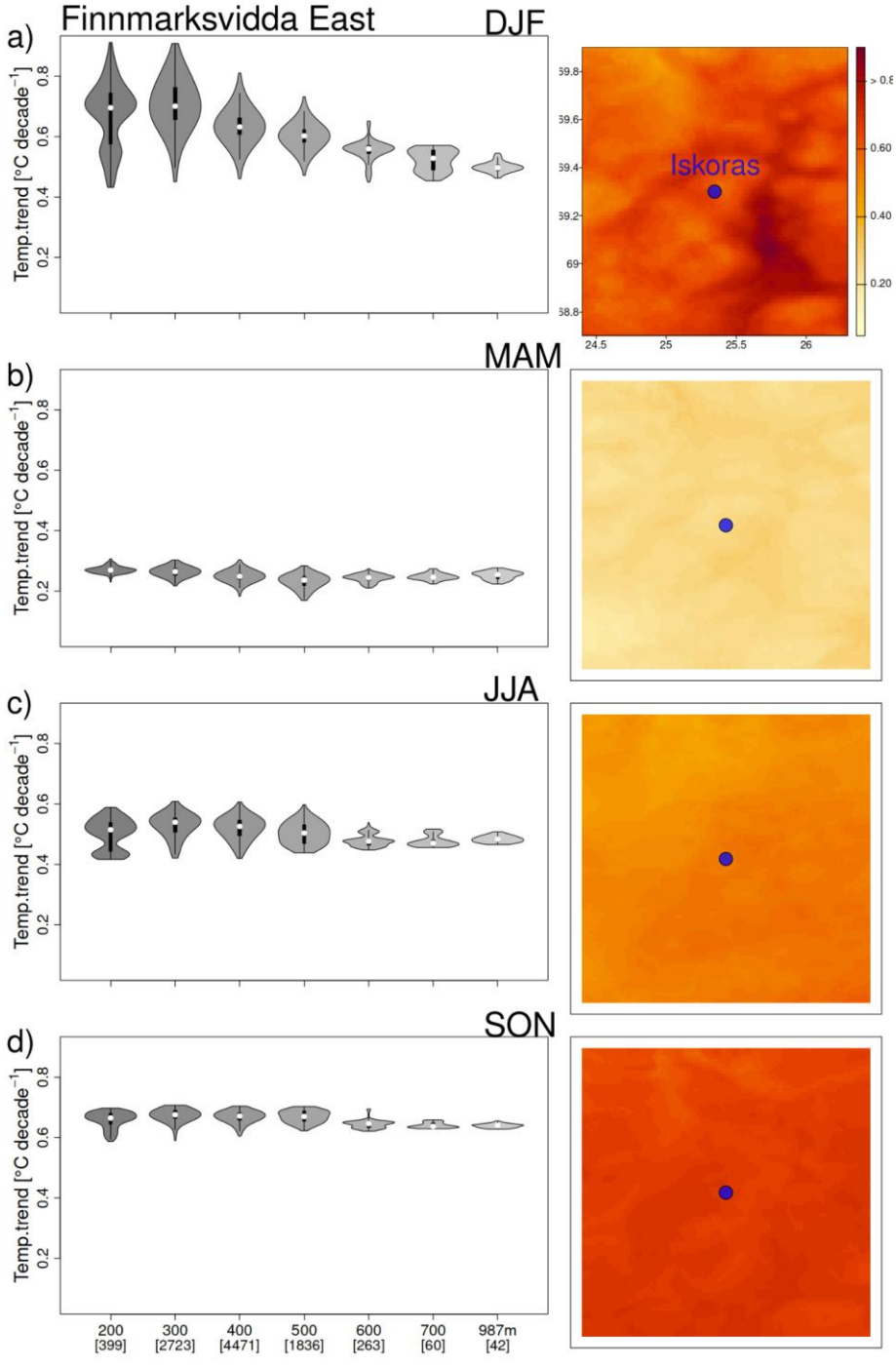


Figure C9. Finnmarksvidda east (Iskoras, ~69.3°N). Note that the data are grouped into 100 m elevation bands and utilize an expanded y-axis scale (0.0–0.9 °C per decade) for the temperature trends, compared to the 250 m bands and 0.0–0.7 °C per decade scale applied in the other regions.

https://doi.org/10.5194/egusphere-2026-5858
Preprint. Discussion started: 4 November 2026
© Author(s) 2026. CC BY 4.0 License.

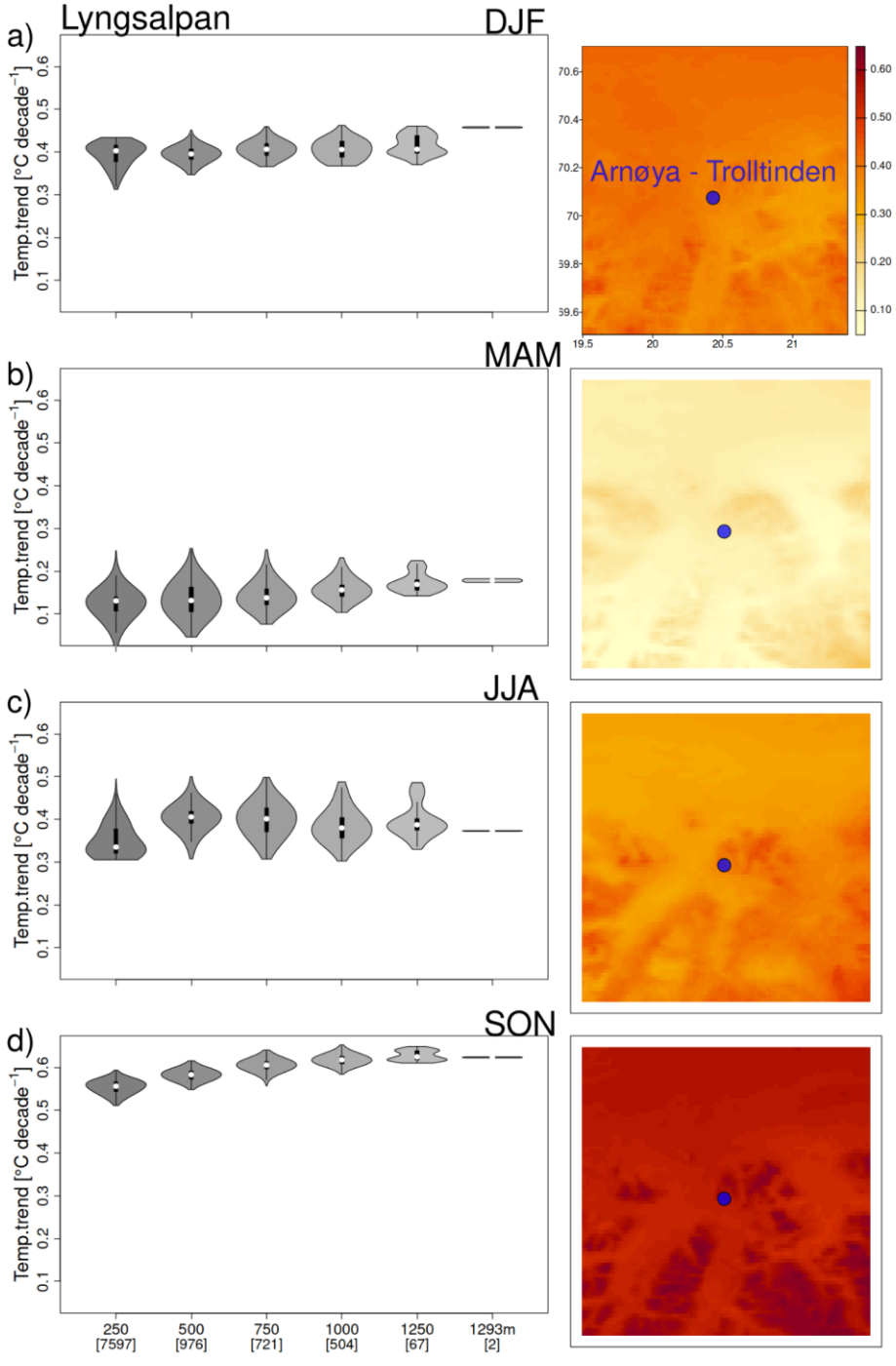


Figure C10. Lyngsalpan (Arnøya - Trolltinden, ~70.1°N).

https://doi.org/10.5194/egusphere-2026-5858
Preprint. Discussion started: 4 November 2026
© Author(s) 2026. CC BY 4.0 License.

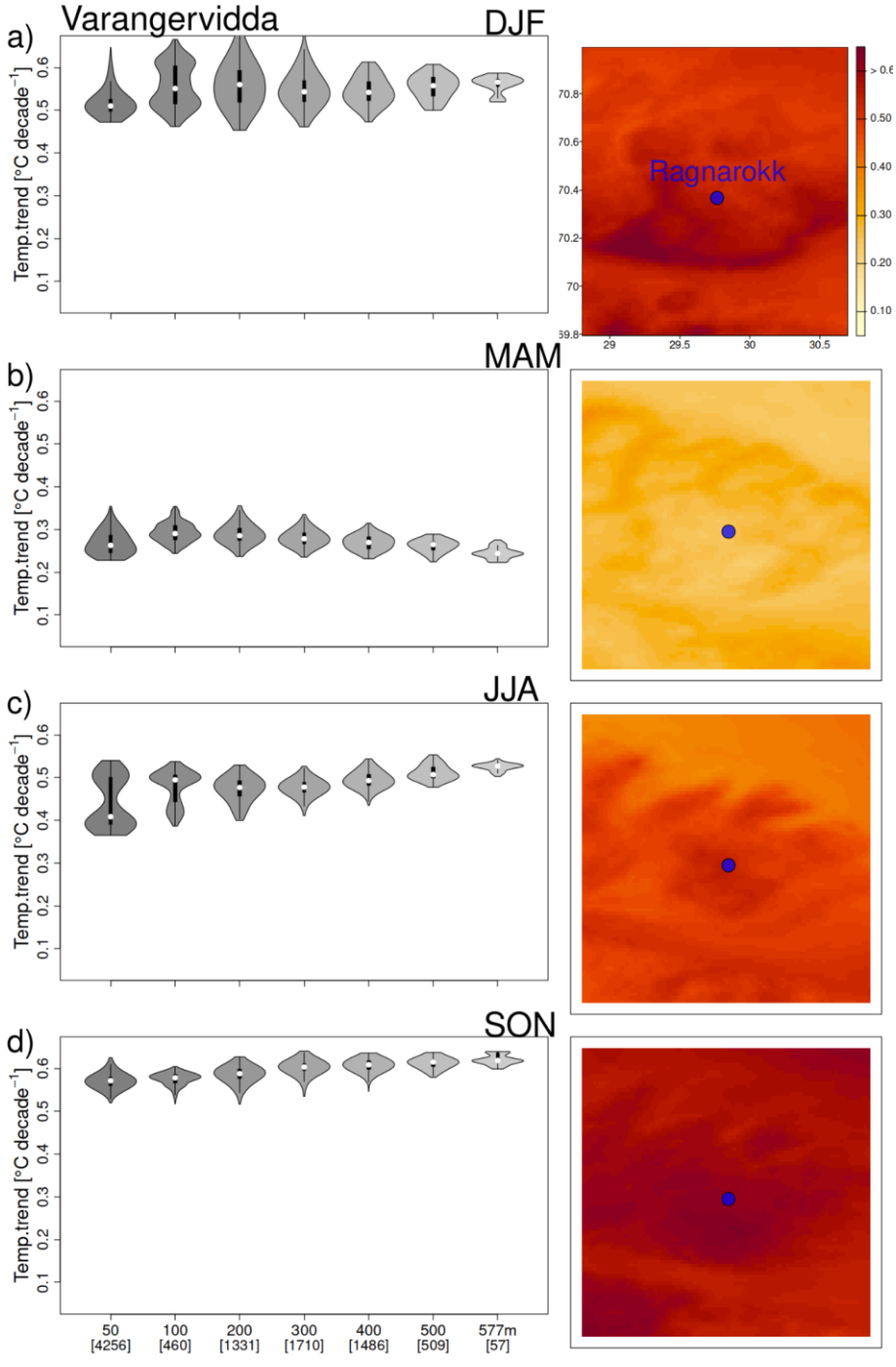


Figure C11. Varangervidda (Ragnarokk, ~70.4°N). Note that the data are grouped into 100 m elevation bands compared to the 250 m bands applied in the other regions.

https://doi.org/10.5194/egusphere-2026-5858
Preprint. Discussion started: 4 November 2026
© Author(s) 2026. CC BY 4.0 License.

930

Appendix D

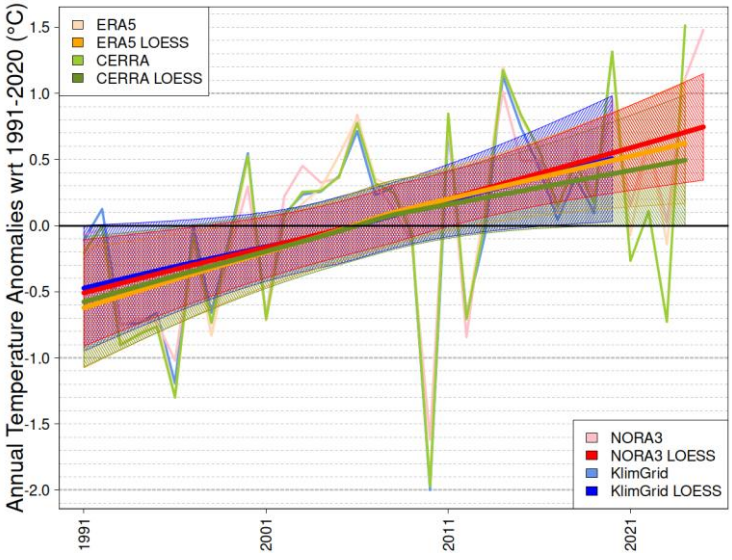


Figure D1. Same as in Figure 7d, but for the 1991-2024 period. KlimGrid (blue), NORA3 (red), ERA5 (orange) and CERRA (green) with
935 LOESS fits and confidence band shown.

940

https://doi.org/10.5194/egusphere-2026-5858
Preprint. Discussion started: 4 November 2026
© Author(s) 2026. CC BY 4.0 License.

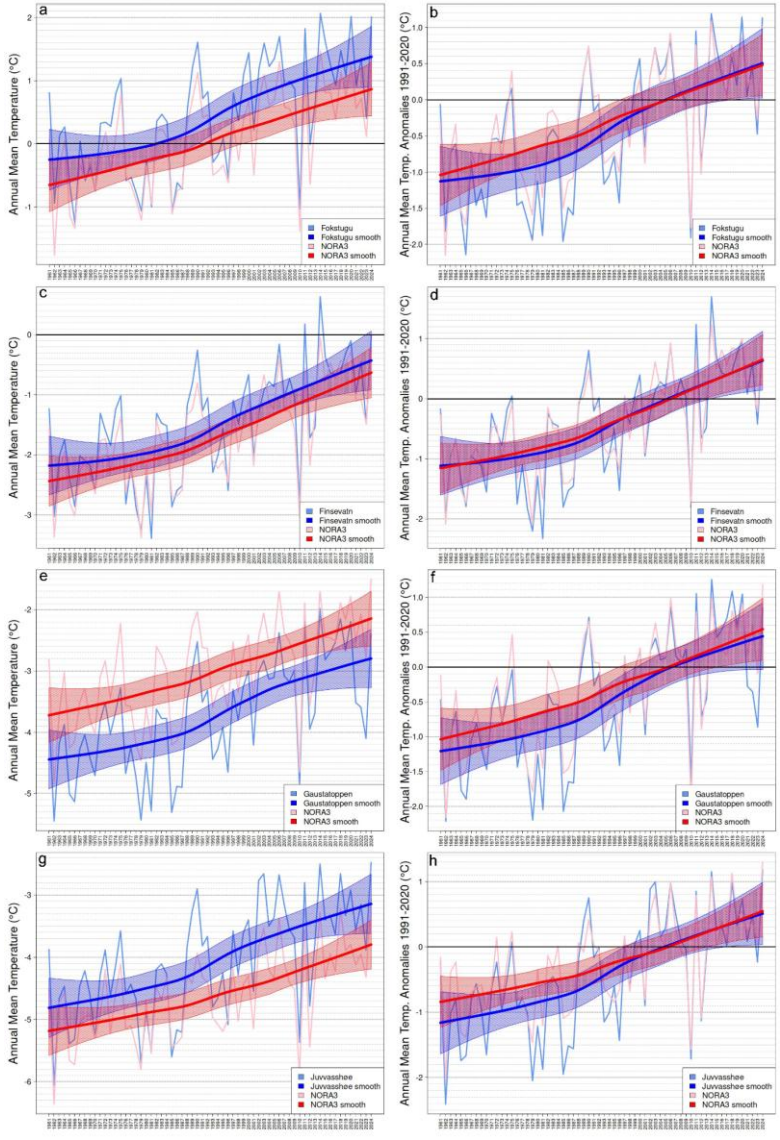


Figure D2. Comparison of multi-decadal annual mean air temperatures and 1991–2020 anomalies between homogenised mountain reference series and NORA3 reanalysis (1961–2024). Panels display absolute mean annual air temperature (MAAT, °C; left column) and corresponding annual temperature anomalies relative to the 1991–2020 baseline (°C; right column) for the four target high-elevation composite series ordered by elevation: (a,b) Fokstugu (station: 973 m a.s.l., NORA3 grid: 1002 m a.s.l.), (c,d) Finsevatn (station: 1210 m a.s.l., NORA3 grid: 1205 m a.s.l.), (e,f) Gaustatoppen (station: 1804 m a.s.l., NORA3 grid: 1532 m a.s.l.), and (g,h) Juvvasshøe (station: 1894 m a.s.l., NORA3 grid: 1846 m a.s.l.).Thin blue lines and thin pink lines show raw annual values for the homogenised in-situ station series and the corresponding NORA3 grid cell, respectively. Thick dark blue and thick red curves represent multi-decadal trends derived from local regression (LOESS) smoothing, with shaded hatched regions indicating the associated 95% confidence intervals. Horizontal solid black lines in anomaly panels (b, d, f, h) represent the 1991–2020 reference baseline (0.0 °C).

https://doi.org/10.5194/egusphere-2026-5858
Preprint. Discussion started: 4 November 2026
© Author(s) 2026. CC BY 4.0 License.

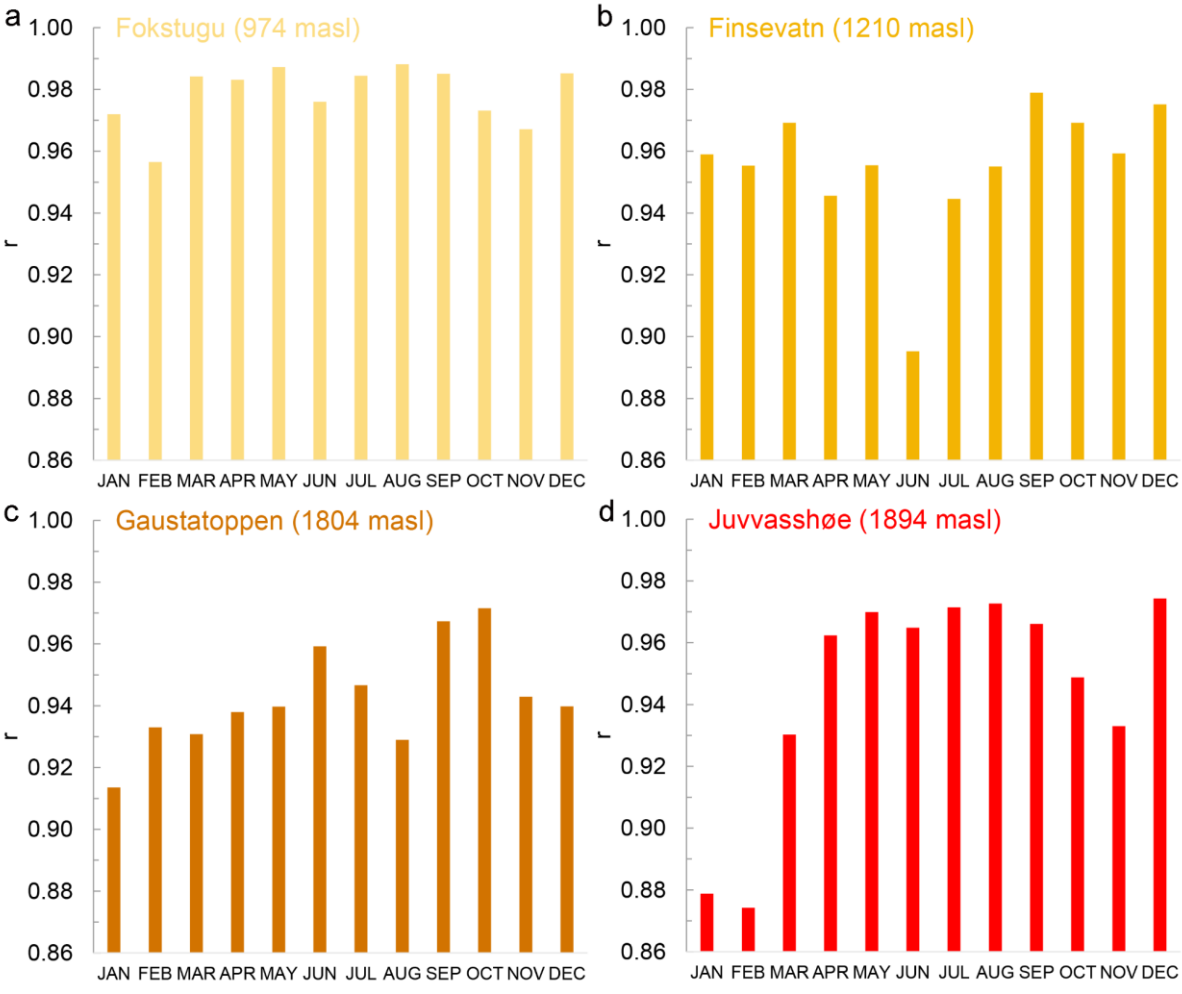


Figure D3. Monthly Pearson correlation coefficients (r) between homogenised mountain station temperature series and NORA3 reanalysis (1981–2025). Panels show month-by-month correlation coefficients (r) derived from monthly mean near-surface air temperatures between in-situ homogenised observations and co-located NORA3 grid cells for: (a) Fokstugu (station: 973 m a.s.l., NORA3 grid: 1002 m a.s.l.), (b) Finsevatn (station: 1210 m a.s.l., NORA3 grid: 1205 m a.s.l.), (c) Gaustatoppen (station: 1804 m a.s.l., NORA3 grid: 1532 m a.s.l.), and (d) Juvvasshøe (station: 1894 m a.s.l., NORA3 grid: 1846 m a.s.l.). Bars represent individual calendar months (JAN-DEC). High correlation values across all sites ($r > 0.87$, predominantly $r > 0.94$–0.98) demonstrate strong temporal covariance and multi-decadal consistency between NORA3 and mountain observations across all seasons, despite local sub-grid elevation offsets.

https://doi.org/10.5194/egusphere-2026-5858
Preprint. Discussion started: 4 November 2026
© Author(s) 2026. CC BY 4.0 License.

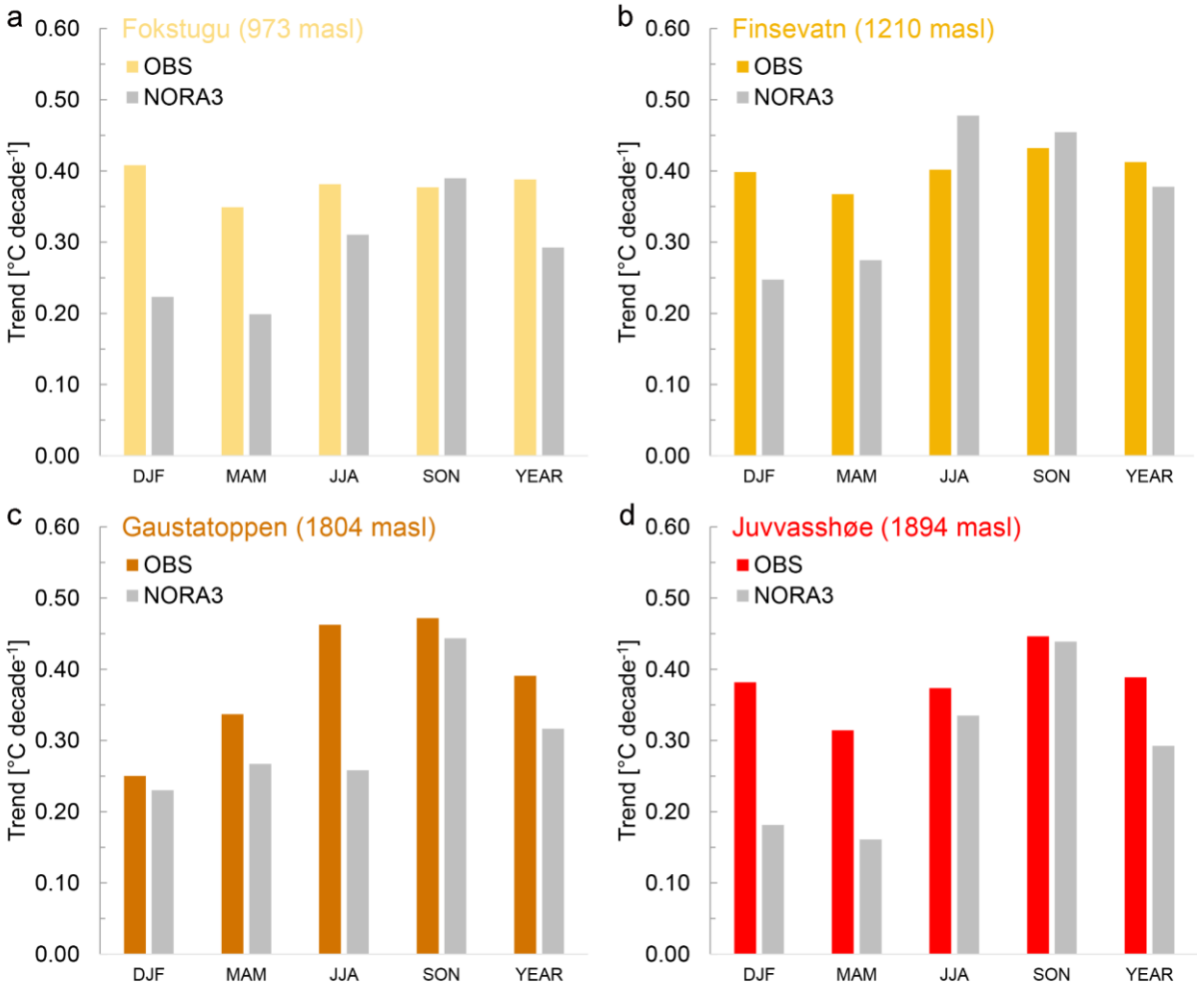


Figure D4. Comparison of seasonal and annual linear near-surface air temperature trends (1981–2025) between homogenised mountain reference series and NORA3 reanalysis. Panels display linear warming trends (°C per decade) for the period 1981–2025 across the four primary target sites ordered by elevation: (a) Fokstugu (station: 973 m a.s.l., NORA3 grid: 1002 m a.s.l.), (b) Finsevatn (station: 1210 m a.s.l., NORA3 grid: 1205 m a.s.l.), (c) Gaustatoppen (station: 1804 m a.s.l., NORA3 grid: 1532 m a.s.l.), and (d) Juvvasshøe (station: 1894 m a.s.l., NORA3 grid: 1846 m a.s.l.). Colored bars represent homogenised in-situ observational series (OBS), while grey bars denote co-located 3-km NORA3 reanalysis grid-cell trends. Bars are grouped by winter (DJF), spring (MAM), summer (JJA), autumn (SON), and annual mean (YEAR). Elevation differences reflect sub-grid digital elevation model smoothing inherent to the 3-km reanalysis resolution, particularly at steep, isolated summits (e.g., Gaustatoppen).

https://doi.org/10.5194/egusphere-2026-5858
Preprint. Discussion started: 4 November 2026
© Author(s) 2026. CC BY 4.0 License.

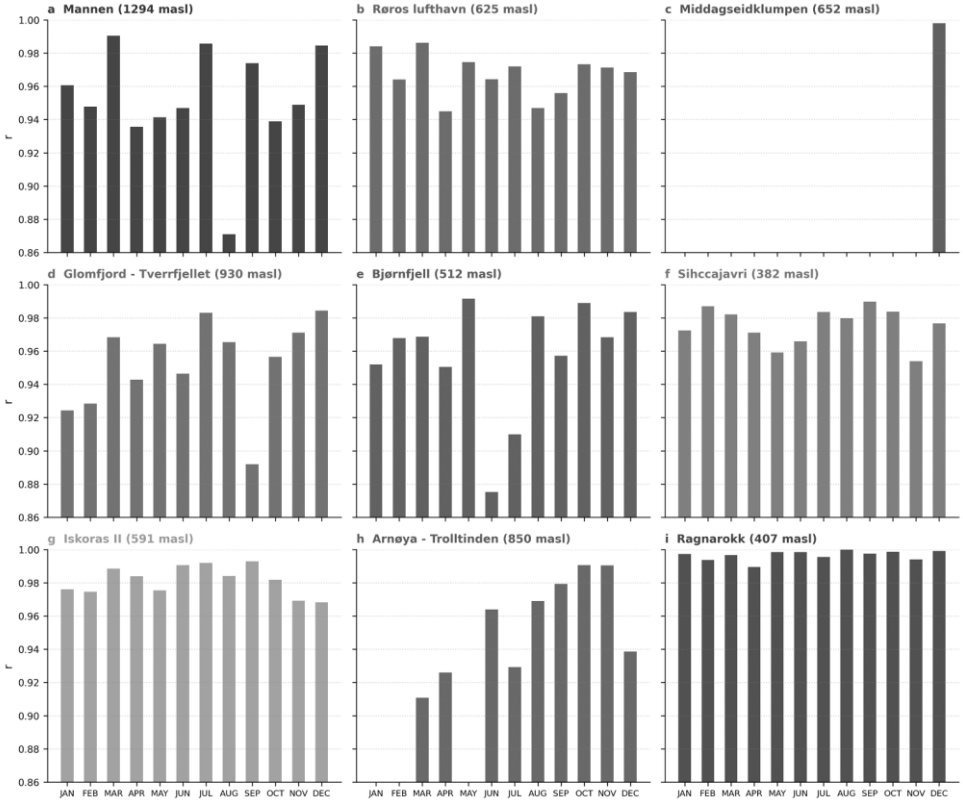


Figure D5. Monthly Pearson correlation coefficients (r) between observations and NORA3 reanalysis across the ten supplementary regional mountain domains. Panels display month-by-month correlation coefficients (r) calculated from monthly mean near-surface air temperatures between in-situ observations and co-located 3-km NORA3 grid cells for: (a) Mannen (Romsdal; 2010–2025; station: 1294 m a.s.l., NORA3 grid: 1266 m a.s.l.), (b) Røros lufthavn (Rørosvidda; 2002–2025; station: 625 m a.s.l., NORA3 grid: 643 m a.s.l.), (c) Middagseidklumpen (Vistfjellan; 2024–2025; station: 652 m a.s.l., NORA3 grid: 582 m a.s.l.), (d) Glomfjord - Tverrfjellet (Meløyalpene; 2014–2025; station: 930 m a.s.l., NORA3 grid: 779 m a.s.l.), (e) Bjørnfjell (Narvikfjellene; 2016–2025; station: 512 m a.s.l., NORA3 grid: 603 m a.s.l.), (f) Sihccajavri (Finnmarksvidda south; 1981–2025; station: 382 m a.s.l., NORA3 grid: 383 m a.s.l.), (g) Iskoras II (Finnmarksvidda east; 2014–2025; station: 591 m a.s.l., NORA3 grid: 542 m a.s.l.), (h) Arnøya - Trolltinden (Lyngsalpan; 2014–2025; station: 850 m a.s.l., NORA3 grid: 574 m a.s.l.), and (i) Ragnarokk (Varangervidda; 2022–2025; station: 407 m a.s.l., NORA3 grid: 403 m a.s.l.). Bars denote individual calendar months (JAN-DEC). Correlation coefficients are calculated over the total overlapping observational period available at each site, reflecting variable record lengths across the monitoring network - ranging from multi-decadal series (e.g., Sihccajavri, 45 years) to recently established AWS sites (e.g., Ragnarokk, 4 years; Middagseidklumpen, 2 years). Note that at Arnøya - Trolltinden (panel h), correlation values for three months fall at or below the y-axis baseline ($r = 0.86$ in Jan, $r = 0.78$ in Feb, and $r = 0.83$ in May) due to extreme coastal-alpine topographic gradient. In general there is a high correlation across all multi-year records ($r > 0.87$, predominantly $r > 0.94$–0.99) that confirm strong temporal covariance between NORA3 and regional mountain observations throughout mainland Norway.

https://doi.org/10.5194/egusphere-2026-5858
Preprint. Discussion started: 4 November 2026
© Author(s) 2026. CC BY 4.0 License.

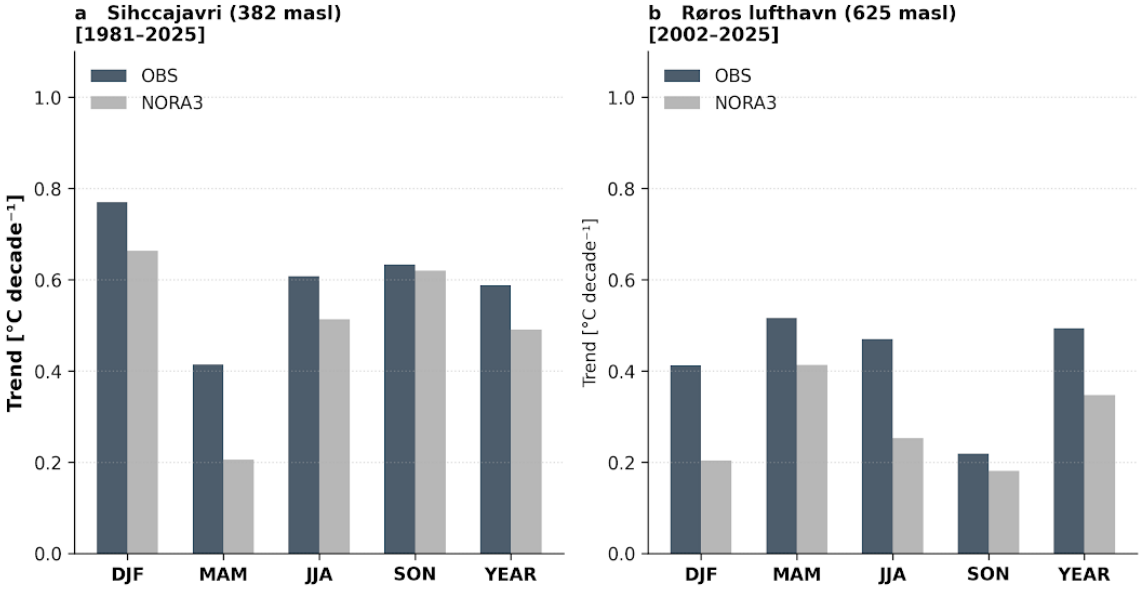


Figure D6. Comparison of seasonal and annual linear near-surface air temperature trends (°C per decade) between long-term regional station observations and NORA3 reanalysis. Panels display seasonal (DJF, MAM, JJA, SON) and annual (YEAR) linear warming trends for the two longest supplementary regional mountain records: (a) Sihccajavri (Finnmarksvidda south; 1981–2025; station: 382 m a.s.l., NORA3 grid: 383 m a.s.l.), and (b) Røros lufthavn (Rørosvidda; 2002–2025; station: 625 m a.s.l., NORA3 grid: 643 m a.s.l.). Dark slate bars represent observational series (OBS), while grey bars denote co-located 3-km NORA3 reanalysis grid-cell trends. Trends are calculated over the full overlapping record length available at each site. Because Sihccajavri covers the standard 1981–2025 baseline (45 years), its trend magnitudes are directly comparable to the primary target reference series (Fig. S13). In contrast, the shorter record at Røros lufthavn (2002–2025; 24 years) prevents direct absolute trend comparisons with the 1981–2025 period, but provides a highly valuable high-elevation benchmark for evaluating the relative agreement and consistency between observations and NORA3 reanalysis. The shorter mountain station series (e.g., Mannen, 16 years; Arnøya-Trolltinden, 12 years etc) were omitted from linear trend benchmarking due to increased sensitivity to decadal-scale variability over short sample windows.

https://doi.org/10.5194/egusphere-2026-5858
Preprint. Discussion started: 4 November 2026
© Author(s) 2026. CC BY 4.0 License.

Appendix E

Table E1. Climatology, linear trend rates, and sensitivities of atmospheric water vapour mixing ratio (w) across a lowland-to-high-mountain elevation gradient in Southern Norway (1981–2025). Stations span low-elevation fjord valleys (Tafjord, 15 m a.s.l.; Lærdal composite [SN54130 Tønjum, SN54120 Moldo, and SN54110 Lærdal IV], 24 m a.s.l.) to intermediate and high-alpine observatories (Fokstugu, 973 m a.s.l.; Sognefjellhytta, 1413 m a.s.l.; Juvvasshøe, 1894 m a.s.l.); note that Juvvasshøe covers 2012–2025, N = 13). For Sognefjellhytta, the effective sample size reflects a historical operational data gap from June 1989 through August 1997, alongside the omission of years 1988 and 2010 in summer (JJA) due to incomplete records and documented sensor drift (yielding N = 32 for summer and N = 36 for autumn). Variables include mean seasonal air temperature (T_{mean}, °C), mean water vapour pressure (e_{mean}, hPa), mean water vapour mixing ratio (w_{mean}, g kg^{-1}), ordinary least-squares decadal trend rates ($Trend_w$, g kg^{-1} per decade), relative decadal trend rates ($Rel.Trend_w = [Trend_w / w_{mean}] \times 100$, % per decade), non-parametric Mann–Kendall significance (p_{MK}), decadal air temperature trend ($Trend_T$, °C per decade), empirical sensitivity ($S = [\Delta w/\Delta T / w_{mean}] \times 100$, % K^{-1}), and Pearson correlation coefficient between seasonal temperature and mixing ratio (r).

Station	Station ID	Elevation (m a.s.l.)	Season	Period	N (years)	T_{mean} (°C)	e_{mean} (hPa)	w_{mean} (g kg^{-1})	$Trend_w$ (g kg^{-1} per decade)	Rel. $Trend_w$ (% per decade)	p_{MK}	$Trend_T$ (°C per decade)	Sensitivity (S) (%K^{-1})	r
Tafjord	SN60500	15	JJA	81–2025	44	14.04	12.17	7.59	0.123	1.62	0.0088	0.34	4.27	0.65
Lærdal (comp)	SN54110/20/30	24	JJA	81–2025	45	14.61	12.13	7.57	0.165	2.17	0.0032	0.39	4.10	0.63
Fokstugu	SN16610	973	JJA	81–2025	45	9.60	8.69	6.06	0.185	3.05	0.0019	0.35	5.12	0.65
Sognefjellhytta	SN55290	1413	JJA	81–2025	32	6.05	7.64	5.61	0.251	4.48	0.0001	0.52	5.66	0.85
Juvvasshøe	SN15270	1894	JJA	12–2025	13	4.12	6.56	5.11	0.459	8.97	0.0173	1.23	4.35	0.70
Tafjord	SN60500	15	SON	81–2025	45	8.04	7.80	4.85	0.112	2.30	0.0126	0.28	3.80	0.74
Lærdal (comp)	SN54110/20/30	24	SON	81–2025	45	6.37	7.85	4.88	0.181	3.72	0.0005	0.23	5.73	0.81
Fokstugu	SN16610	973	SON	81–2025	45	0.92	5.53	3.86	0.165	4.28	0.0005	0.39	5.47	0.77
Sognefjellhytta	SN55290	1413	SON	81–2025	36	-1.46	5.03	3.71	0.159	4.28	0.0024	0.48	7.04	0.91
Juvvasshøe	SN15270	1894	SON	12–2025	13	-2.43	4.41	3.45	0.478	13.86	0.0087	1.01	5.12	0.75

https://doi.org/10.5194/egusphere-2026-5858
Preprint. Discussion started: 4 November 2026
© Author(s) 2026. CC BY 4.0 License.

Code and data availability

The datasets generated and analysed during the current study are available from the following sources:

Observational air temperature data: All air temperature observations from Norwegian weather stations are publicly available and can be downloaded from the Norwegian Meteorological Institute (MET Norway) historical climate data archives via https://seklima.met.no/ and the Frost API at https://frost.met.no.

NORA3 reanalysis: The NORA3 reanalysis (3 km) is available at https://thredds.met.no/thredds/catalog/projects/nora3.html. The NORA3 temperature fields downscaled to 1 km are available as the MET Nordic long-term consistent dataset at https://thredds.met.no/thredds/catalog/metppltcarchivev1/catalog.html, documented at https://github.com/metno/NWPdocs/wiki/MET-Nordic-dataset.

ERA5 and CERRA reanalyses: The 2-m air temperature fields derived from the ERA5 (DOI: 10.24381/cds.adbb2d47) and CERRA reanalyses (DOI: 10.24381/cds.622a565a) are available through the Copernicus Climate Data Store (CDS) at https://cds.climate.copernicus.eu

Code availability: Information regarding the data processing and analysis codes can be obtained from the corresponding author upon request.

Author contributions

KI conceptualised the study, led the research and drafted the original manuscript. ØN, HMG, and JL curated the observational data; ØN led the digitisation of historical records, HMG led the homogenisation of the long-term reference series, and JL processed and analysed the national dataset, and significantly contributed to harmonising and refining the overall text. AMC and CL performed the NORA3 data processing and formal analysis, with CL leading the evaluation against observational grids and reanalyses. TNN developed the NORA3 1-km downscaling code and LB made the initial analyses of NORA3. REB conducted national and regional-scale statistical analyses and evaluated the statistical methodology for the observational datasets. AD, IHB, EB, HBE, BE, RSØ, and KØ contributed to the interpretation of results and discussion of physical EDW drivers - including snow-albedo feedbacks and inversions (IHB), humidity (EB), and cryosphere linkages (BE, RSØ). All authors contributed to reviewing and editing the final manuscript.

https://doi.org/10.5194/egusphere-2026-5858
Preprint. Discussion started: 4 November 2026
© Author(s) 2026. CC BY 4.0 License.

Competing interests

The authors declare that they have no conflict of interest.

Disclaimer

Copernicus Publications remains neutral with regard to jurisdictional claims made in the text, published maps, institutional affiliations, or any other geographical representation in this paper. While Copernicus Publications makes every effort to include appropriate place names, the final responsibility lies with the authors. Views expressed in the text are those of the authors and do not necessarily reflect the views of the publisher."

Acknowledgements

This study was supported by the project "Klimarisiko i Jotunheimen" (2023–2026), funded by the Regional Research Funds of Norway (Regionalt forskingsfond Innlandet), and the "Fjellviten" project (2024–2027), funded by the Savings Bank Foundation DNB (Sparebankstiftelsen DNB) and led by the Norwegian Mountain Centre (Norsk Fjellsenter). We also acknowledge internal funding and support from the Norwegian Meteorological Institute. Furthermore, this work serves as a scientific contribution to "Klimapark 2469", a nature park and outdoor discovery centre in the alpine region of Jotunheimen. Finally, we extend our special thanks to Olav P. Amundgård for his invaluable efforts in digitising the historical high-elevation observation series that form a central foundation for this study. The authors acknowledge the use of Sikt AI-chat (provided by Sikt - Norwegian Agency for Shared Services in Education and Research) and Google Gemini for English language editing and text condensation during the preparation of this manuscript. All final editorial decisions and the overall responsibility for the content remain with the authors.

References

Andreassen, L. M., Isaksen, K., Monrad-Krohn, L. J., Abderhalden, J. M., Girod, L., De Marco, J., Etzelmüller, B., Oldani, S., and Ødegård, R. S.: Rapid mass loss and climate-driven dynamics of the Juvfonne ice patch, Norway (2010–2025), EGUsphere [preprint], https://doi.org/10.5194/egusphere-2026-3152, 2026.

Benjamini, Y., and Hochberg, Y.: Controlling the false discovery rate: a practical and powerful approach to multiple testing, J. R. Stat. Soc. Ser. B, 57, 289–300, https://doi.org/10.1111/j.2517-6161.1995.tb02031.x, 1995.

Birkeland, K.: The Norwegian Aurora Polaris Expedition 1902-1903. Volume I: On the Cause of Magnetic Storms and The Origin of Terrestrial Magnetism (Second Section), H. Aschehoug & Co., 1913.

Bjerknes, J.: On the structure of moving cyclones, Mon. Weather Rev., 47, 95–99, 1919.

https://doi.org/10.5194/egusphere-2026-5858
Preprint. Discussion started: 4 November 2026
© Author(s) 2026. CC BY 4.0 License.

Bjerknes, J., and Solberg, H.: Life cycle of cyclones and the polar front theory of atmospheric circulation, Geofys. Publ., 3, 1–18, 1922.

Bjerknes, V.: Das Problem der Wettervorhersage, betrachtet vom Standpunkte der Mechanik und der Physik, Meteorol. Z., 21, 1–7, 1904.

Bjerknes, V., Bjerknes, J., Solberg, H., and Bergeron, T.: Physikalische Hydrodynamik mit Anwendung auf die dynamische Meteorologie, Julius Springer, Berlin, 797 pp., 1933.

Brekke, A.: Arven etter Haldde-observatoriet, Naturen, 146, 40–47, https://doi.org/10.18261/naturen.146.1.5, 2022.

Bryn, A. and Potthoff, K.: Elevational treeline and forest line dynamics in Norwegian mountain areas – a review, Landsc. Ecol., 33, 1225–1245, https://doi.org/10.1007/s10980-018-0670-8, 2018.

Byrne, M. P., Boos, W. R., and Hu, S.: Elevation-dependent warming: observations, models, and energetic mechanisms, Weather Clim. Dynam., 5, 763–777, https://doi.org/10.5194/wcd-5-763-2024, 2024.

Carrer, M., Dibona, R., Prendin, A. L., and Brunetti, M.: Recent waning snowpack in the Alps is unprecedented in the last six centuries, Nat. Clim. Change, 13, 155–160, https://doi.org/10.1038/s41558-022-01575-3, 2023.

Cavalleri, F., Viterbo, F., Brunetti, M., Bonanno, R., Manara, V., Lussana, C., Lacavalla, M., and Maugeri, M.: Inter-comparison and validation of high-resolution surface air temperature reanalysis fields over Italy, Int. J. Climatol., 44, 2681–2700, https://doi.org/10.1002/joc.8475, 2024.

Ceppi, P., Scherrer, S. C., Fischer, A. M., and Appenzeller, C.: Revisiting Swiss temperature trends 1959–2008, Int. J. Climatol., 32, 203–213, https://doi.org/10.1002/joc.2260, 2012.

Danielson, J. J. and Gesch, D. B.: Global Multi-resolution Terrain Elevation Data 2010 (GMTED2010), U.S. Geological Survey Open-File Report 2011-1073, U.S. Geological Survey, Reston, VA, https://pubs.usgs.gov/of/2011/1073/, 2011.

Davy, R. and Esau, I.: Differences in the efficacy of climate forcings explained by variations in atmospheric boundary layer depth, Nat. Commun., 7, 11690, https://doi.org/10.1038/ncomms11690, 2016

Devik, O.: Blant fiskere, forskere og andre folk, H. Aschehoug & Co., 1971.

Dyrrdal, A. V., Bakke, S. J., Hanssen-Bauer, I., Mayer, S., Nilsen, I. B., Nilsen, J. E. Ø., Paasche, Ø., Saloranta, T., and Arthun, M. (Eds.): Klima i Norge - kunnskapsgrunnlag for klimatilpasning oppdatert i 2025 (NCCS-rapport nr. 1/2025), Norsk klimaservicesenter, https://doi.org/10.60839/4rgq-nn84, 2025.

Egli, S., Thies, B., Drönner, J., Cermak, J., and Bendix, J.: A 10 year fog and low stratus climatology for Europe based on Meteosat Second Generation data, Q. J. R. Meteorol. Soc., 143, 530–541, https://doi.org/10.1002/qj.2941, 2017.

Etzelmüller, B., Guglielmin, M., Hauck, C., Hilbich, C., Hoelzle, M., Isaksen, K., Noetzli, J., Oliva, M., and Ramos, M.: Twenty years of European mountain permafrost dynamics - the PACE legacy, Environ. Res. Lett., 15, 104070, https://doi.org/10.1088/1748-9326/abae9d, 2020.

Etzelmüller, B., Isaksen, K., Czekirda, J., Westermann, S., Hilbich, C., and Hauck, C.: Rapid warming and degradation of mountain permafrost in Norway and Iceland, The Cryosphere, 17, 5477–5497, https://doi.org/10.5194/tc-17-5477-2023, 2023.

https://doi.org/10.5194/egusphere-2026-5858
Preprint. Discussion started: 4 November 2026
© Author(s) 2026. CC BY 4.0 License.

Gobiet, A., Kotlarski, S., Beniston, M., Heinrich, G., Rajczak, J., and Stoffel, M.: 21st century climate change in the European Alps - A review, Sci. Total Environ., 493, 1138–1151, https://doi.org/10.1016/j.scitotenv.2013.07.050, 2014.

Grêt-Regamey, A., Brunner, S. H., and Kienast, F.: Mountain ecosystem services: who cares?, Mt. Res. Dev., 32, S1–S11, https://doi.org/10.1659/MRD-JOURNAL-D-10-00115.S1, 2012.

Haakenstad, H., Breivik, Ø., Furevik, B. R., Reistad, M., Bohlinger, P., and Aarnes, O. J.: NORA3: A nonhydrostatic high-resolution hindcast of the North Sea, the Norwegian Sea, and the Barents Sea, J. Appl. Meteorol. Climatol., 60, 1443–1464, https://doi.org/10.1175/JAMC-D-21-0029.1, 2021.

Haakenstad, H., and Breivik, Ø.: NORA3. Part II: Precipitation and temperature statistics in complex terrain modeled with a nonhydrostatic model, J. Appl. Meteorol. Climatol., 61, 1549–1572, https://doi.org/10.1175/JAMC-D-22-0005.1, 2022.

Hanssen-Bauer, I., and Isaksen, K.: Snow cover and air temperature 1961–2025: Analyses based on observations from 23 Norwegian stations (MET Report No. 07/2026 Climate), Norwegian Meteorological Institute, 2026.

Hanssen-Bauer, I., Tveito, O. E., Tajet, H. T. T., and Skaland, R. G.: Temperatur- og nedbør-regioner i Norge: Sammenligning av forskjellige regioninndelinger (MET report No. 11/2022), Norwegian Meteorological Institute, 2022.

Harris, C., Haeberli, W., Vonder Mühll, D., and King, L.: Permafrost monitoring in the high mountains of Europe: the PACE project in its global context, Permafrost Periglac. Process., 12, 3–11, https://doi.org/10.1002/ppp.377, 2001.

Held, I. M. and Soden, B. J.: Robust responses of the hydrological cycle to global warming, J. Climate, 19, 5686–5699, https://doi.org/10.1175/JCLI3990.1, 2006.

Hjortnæs, K.: Høyfjellstasjonene på Gaustatoppen og Fanaråken, en saga blott, Været, 22–23, 1979.

Hock, R., Rasul, G., Adler, C., Cáceres, B., Gruber, S., Hirabayashi, Y., Jackson, M., Kääb, A., Kang, S., Kutuzov, S., Milner, A., Molau, U., Morin, S., Orlove, B., and Steltzer, H.: High Mountain Areas, in: IPCC Special Report on the Ocean and Cryosphere in a Changing Climate, edited by: Pörtner, H.-O. et al., Cambridge University Press, Cambridge, UK and New York, NY, USA, 131–202, https://doi.org/10.1017/9781009157964.004, 2019.

Immerzeel, W. W., Lutz, A. F., Andrade, M., et al.: Importance and vulnerability of the world's water towers, Nature, 577, 364–369, https://doi.org/10.1038/s41586-019-1822-y, 2020.

Kotlarski, S., Gobiet, A., Morin, S., et al.: 21st Century alpine climate change, Clim. Dyn., 60, 65–86, https://doi.org/10.1007/s00382-022-06303-3, 2023.

Kuhn, M., and Olefs, M.: Elevation-Dependent Climate Change in the European Alps, in: Oxford Research Encyclopedia of Climate Science, Oxford Academic, New York, NY, https://doi.org/10.1093/acrefore/9780190228620.013.762, 2020.

Kuya, E. K., Gjelten, H. M., and Tveito, O. E.: Homogenization of Norway's mean monthly temperature series (MET Report No. 03/2020), Norwegian Meteorological Institute, 2020.

Körner, C.: Mountain biodiversity, its causes and function, AMBIO, 33, 11–17, https://doi.org/10.1007/0044-7447-33.sp13.11, 2004.

Lutz, J., Hanssen-Bauer, I., Tveito, O. E., and Dobler, A.: Precipitation variability in Norway 1961–2020 (MET Report No. 01/2024 Climate), Norwegian Meteorological Institute, 2024.

https://doi.org/10.5194/egusphere-2026-5858
Preprint. Discussion started: 4 November 2026
© Author(s) 2026. CC BY 4.0 License.

Mann, H. B.: Nonparametric tests against trend, Econometrica, 13, 245–259, https://doi.org/10.2307/1907187, 1945.

Masson, V., Le Moigne, P., Martin, E., Faroux, S., Alias, A., Alkama, R., Belamari, S., Barbu, A., Boone, A., Bouyssel, F., Brousseau, P., Brun, E., Calvet, J.-C., Carrer, D., Decharme, B., Delire, C., Donier, S., Essaouini, K., Gibelin, A.-L., Giordani, H., Habets, F., Jidane, M., Kerdraon, G., Kourzeneva, E., Lafaysse, M., Lafont, S., Lebeaupin Brossier, C., Lemonsu, A., Mahfouf, J.-F., Marguinaud, P., Mokhtari, M., Morin, S., Pigeon, G., Salgado, R., Seity, Y., Taillefer, F., Tanguy, G., Tulet, P., Vincendon, B., Vionnet, V., and Voldoire, A.: The SURFEXv7.2 land and ocean surface platform for coupled or offline simulation of earth surface variables and fluxes, Geosci. Model Dev., 6, 929–960, https://doi.org/10.5194/gmd-6-929-2013, 2013.

McLeod, A. I.: Kendall rank correlation and Mann-Kendall trend test, R package Kendall, 602, 1–10, https://CRAN.R-project.org/package=Kendall, 2005.

Mestre, O., Domonkos, P., Picard, F., Auer, I., Robin, S., Lebarbier, E., Böhm, R., Aguilar, E., Guijarro, J., Vertachnik, G., Klancar, M., Dubuisson, B., and Stepanek, P.: HOMER: A homogenization software - methods and applications, IDŐJÁRÁS, 117, 47–67, https://www.met.hu/en/ismeret-tar/kiadvanyok/idojaras/index.php?id=82, 2013.

Minder, J. R., Letcher, T. W., and Liu, C.: The character and causes of elevation-dependent warming in high-resolution simulations of Rocky Mountain climate change, J. Clim., 31, 2093–2113, https://doi.org/10.1175/JCLI-D-17-0321.1, 2018.

Mountain Research Initiative EDW Working Group: Elevation-dependent warming in mountain regions of the world, Nat. Clim. Change, 5, 424–430, https://doi.org/10.1038/nclimate2563, 2015.

Nilsen, I. B., Isaksen, K., Nordeide, S., Hanssen-Bauer, I., and Bakke, S. J.: Observerte langtidstrender i snøforhold i Norge: Bakgrunnsrapport til rapporten Klima i Norge (NVE Rapport nr. 9/2025), Norges vassdrags- og energidirektorat, https://urn.nb.no/URN:NBN:no-nb_pliktmonografi_000045635, 2025.

Ohmura, A.: Enhanced temperature variability in high-altitude climate change, Theor. Appl. Climatol., 110, 499–508, https://doi.org/10.1007/s00704-012-0687-x, 2012.

Palazzi, E., Mortarini, L., Terzago, S., and Von Hardenberg, J.: Elevation-dependent warming in global climate model simulations at high spatial resolution, Clim. Dyn., 52, 2685–2702, https://doi.org/10.1007/s00382-018-4287-z, 2019.

Pepin, N. C., and Lundquist, J. D.: Temperature trends at high elevations: Patterns across the globe, Geophys. Res. Lett., 35, L14701, https://doi.org/10.1029/2008GL034026, 2008.

Pepin, N. C., Arnone, E., Gobiet, A., Haslinger, K., Kotlarski, S., Notarnicola, C., Palazzi, E., et al.: Climate changes and their elevational patterns in the mountains of the world, Rev. Geophys., 60, e2020RG000730, https://doi.org/10.1029/2020RG000730, 2022.

Pepin, N., Apple, M., Knowles, J., Terzago, S., Arnone, E., Hänchen, L., et al.: Elevation-dependent climate change in mountain environments, Nat. Rev. Earth Environ., 6, 772–788, https://doi.org/10.1038/s43017-025-00740-4, 2025.

Rahbek, C., Borregaard, M. K., Colwell, R. K., Dalsgaard, B. O., Holt, B. G., Morueta-Holme, N., et al.: Humboldt's enigma: What causes global patterns of mountain biodiversity?, Science, 365, 1108–1113, https://doi.org/10.1126/science.aax0149, 2019.

https://doi.org/10.5194/egusphere-2026-5858
Preprint. Discussion started: 4 November 2026
© Author(s) 2026. CC BY 4.0 License.

Rangwala, I., and Miller, J. R.: Climate change in mountains: a review of elevation-dependent warming and its possible causes, Clim. Change, 114, 527–547, https://doi.org/10.1007/s10584-012-0419-3, 2012.

Rangwala, I., Sinsky, E., and Miller, J. R.: Amplified warming projections for high altitude regions of the northern hemisphere mid-latitudes from CMIP5 models, Environ. Res. Lett., 8, 024040, https://doi.org/10.1088/1748-9326/8/2/024040, 2013.

Rottler, E., Kormann, C., Francke, T., and Bronstert, A.: Elevation-dependent warming in the Swiss Alps 1981–2017: Features, forcings and feedbacks, Int. J. Climatol., 39, 2556–2568, https://doi.org/10.1002/joc.5970, 2019.

Ruosteenoja, K. and Räisänen, J.: Evolution of observed and modelled temperatures in Finland in 1901–2018 and potential dynamical reasons for the differences, Int. J. Climatol., 41, 3374–3390, https://doi.org/10.1002/joc.7024, 2021.

Scherrer, S. C., and Appenzeller, C.: Fog and low stratus over the Swiss Plateau - a climatological study, Int. J. Climatol., 34, 678–686, https://doi.org/10.1002/joc.3714, 2014.

Scherrer, S. C., Isotta, F. A., and Kotlarski, S.: Elevation-dependent warming in Switzerland: Observed signals and dataset limitations, J. Eur. Meteorol. Soc., 4, 100026, https://doi.org/10.1016/j.jemets.2025.100026, 2026.

Sen, P. K.: Estimates of the Regression Coefficient Based on Kendall's Tau, J. Am. Stat. Assoc., 63, 1379–1389, https://doi.org/10.1080/01621459.1968.10480934, 1968.

Sollid, J. L., Holmlund, P., Isaksen, K., and Harris, C.: Deep permafrost boreholes in western Svalbard, northern Sweden and southern Norway, Nor. Geogr. Tidsskr., 54, 186–191, https://doi.org/10.1080/002919500448567, 2000.

Spinnangr, F.: Meteorologisk observatorium paa Fanaraaken i Jotunheimen, Naturen, 50, 342–348, 1926.

Spinnangr, F. and Eide, O.: On the climate of the lofty mountain region of southern Norway, Meteorologiske Annaler, 2(13), 403–464, 1948.

Tajet, H. T. T., Hanssen-Bauer, I., Nilsen, I. B., Tveito, O. E., and Gangstø, R.: Temperaturindekser 1961-1990 og 1991-2020 (MET report No. 2/2024), Norwegian Meteorological Institute, 2024.

Tudoroiu, M., Eccel, E., Gioli, B., Gianelle, D., Schume, H., Genesio, L., and Miglietta, F.: Negative elevation-dependent warming trend in the Eastern Alps, Environ. Res. Lett., 11, 044021, https://doi.org/10.1088/1748-9326/11/4/044021, 2016.

Tveito, O. E.: Norwegian standard climate normals 1991–2020: The methodological approach (MET Report No. 05/2021 Climate), Norwegian Meteorological Institute, 2021.

Tveito, O. E.: The effect of homogenization when constructing long-term gridded monthly precipitation and temperature data, Int. J. Climatol., 43, 7618–7632, https://doi.org/10.1002/joc.8283, 2023.

Wang, Q., Fan, X., and Wang, M.: Recent warming amplification over high elevation regions across the globe, Clim. Dyn., 43, 87–101, https://doi.org/10.1007/s00382-013-1889-3, 2014.

Wilks, D. S.: On "field significance" and the false discovery rate, J. Appl. Meteorol. Climatol., 45, 1181–1189, https://doi.org/10.1175/JAM2404.1, 2006.

Wilks, D. S.: "The Stippling Shows Statistically Significant Grid Points": How Research Results are Routinely Overstated and Overinterpreted, and What to Do about It, Bull. Am. Meteorol. Soc., 97, 2263–2273, https://doi.org/10.1175/BAMS-D-15-00267.1, 2016.

https://doi.org/10.5194/egusphere-2026-5858
Preprint. Discussion started: 4 November 2026
© Author(s) 2026. CC BY 4.0 License.



1210 Wilks, D. S.: Statistical Methods in the Atmospheric Sciences, Elsevier Science, https://doi.org/10.1016/C2017-0-03921-6, 2019.